Master's thesis

NTNU
Norwegian University of Science and Technology
Faculty of Natural Sciences
Department of Materials Science and Engineering

Sigurd Opdal Eidem

Synthesis of Hexagonal Yttrium and Ytterbium Manganites

Master's thesis in Nanotechnology
Supervisor: Prof. Mari-Ann Einarsrud
Co-supervisor: Dr. Kenneth Marshall

July 2020

NTNU
Norwegian University of
Science and Technology

Sigurd Opdal Eidem

Synthesis of Hexagonal Yttrium and Ytterbium Manganites

Master's thesis in Nanotechnology
Supervisor: Prof. Mari-Ann Einarsrud
Co-supervisor: Dr. Kenneth Marshall
July 2020

Norwegian University of Science and Technology
Faculty of Natural Sciences
Department of Materials Science and Engineering

NTNU
Norwegian University of
Science and Technology

To my family. Your unconditional love and support all the way from my childhood to the submission of this thesis mean more to me than you can imagine.

PREFACE

This Master's Thesis has been submitted as part of the requirements for the degree of Master of Science in Nanotechnology at the Norwegian University of Science and Technology (NTNU). All the experimental work presented in this thesis was carried out by the author between January and June 2020 at the Department of Materials Science and Engineering, NTNU. Prof. Mari-Ann Einarsrud and Dr. Kenneth Marshall have served as supervisor and co-supervisor, respectively. The work presented is a further investigation of the material system and synthesis approach explored in the author's specialization project between August 2019 and December 2019, and the Background and Introduction chapters of this thesis are based on the corresponding chapters in the author's project thesis (submitted in December 2019).

The outbreak of the COVID-19 pandemic has undeniably affected the experimental work presented in this thesis. Not only were all laboratories shut down for students for one and a half months, between 12.03.2020 and 27.04.2020; restrictions on instrument training and on the number of people allowed to work simultaneously in the laboratories were also imposed after the reopening of the laboratories. Although it might have been possible to carry out more experimental work as well as to employ additional characterization techniques if not for the pandemic and the restrictions that followed, it is the author's sincere hope that this thesis will provide insight into the exciting field it is devoted to.

ACKNOWLEDGMENTS

Trondheim, 19.07.2020

Sigurd Opdal Eidem

ABSTRACT

This study is devoted to investigating hydrothermal synthesis of hexagonal rare-earth manganites, h-LnMnO$_3$ (Ln denoting the rare-earth element), which are a class of lead-free ferroelectric materials. Yttrium and ytterbium are used as the rare-earth elements, and reaction conditions such as temperature, hydroxide concentration, and reaction time are varied. Syntheses from both oxide precursors and soluble salt precursors are performed.

Both h-YMnO$_3$ and h-YbMnO$_3$ are successfully synthesized, the former at 240 °C and the latter in a wide range of temperatures, including as low as 110 °C. A low-temperature, environmentally friendly route for synthesis of h-LnMnO$_3$ particles is thus presented. The particles have platelet morphology with a typical diameter below 1 µm when ytterbium is used as the rare-earth element. When yttrium is used, hollow platelets with typical diameter around 10-50 µm form when the reaction time is 48-72 h, whereas dense platelets are seen after shorter reaction times. Differences caused by choice of rare-earth element and other reaction parameters are observed and discussed, and a mechanism for manganite formation during hydrothermal synthesis is proposed. In the proposed mechanism, h-LnMnO$_3$ forms via the intermediate phases Ln(OH)$_3$ and LnOOH, and the h-YMnO$_3$ eventually turns hollow by mechanism of inside-out Ostwald ripening.

SAMMENDRAG

I denne studien utforskes hydrotermisk syntese av heksagonale manganitter av sjeldne jordartsmetaller, h-LnMnO$_3$ (der Ln er det sjeldne jordartsmetallet), som er en klasse blyfrie ferroelektriske materialer. De sjeldne jordartsmetallene som brukes er yttrium og ytterbium, og reaksjonsbetingelser som temperatur, hydroksidkonsentrasjon og reaksjonstid varieres. Synteser gjøres både fra oksidforløpere og fra løselige saltforløpere.

Vellykket syntese av både h-YMnO$_3$ og h-YbMnO$_3$ gjennomføres, førstnevnte ved 240 °C og sistnevnte i et bredt spektrum av temperaturer, helt ned til 110 °C. Dermed presenteres en miljøvennlig synteserute til h-LnMnO$_3$-partikler som kan gjennomføres ved lave temperaturer. Partiklene har platemorfologi med typisk diameter under 1 µm når ytterbium anvendes som sjeldent jordartsmetall. Når yttrium benyttes dannes hule plater med typisk diameter omkring 10-50 µm når reaksjonstiden er 48-72 t, mens platene ikke er hule etter kortere reaksjonstid. Forskjeller som resulterer fra valg av sjeldent jordartsmetall og andre reaksjonsparametre observeres og diskuteres, og en mekanisme for manganittdannelse under hydrotermisk syntese foreslås. I den foreslåtte mekanismen går dannelsen av h-LnMnO$_3$ via mellomproduktene Ln(OH)$_3$ og LnOOH, og h-YMnO$_3$-partiklene blir etter hvert hule ved ostwaldmodning fra innsiden og ut.

CONTENTS

ACRONYMS

EDXS   Energy Dispersive X-ray Spectroscopy

FeRAM Ferroelectric Random Access Memory

KNN $K_xNa_{1-x}NbO_3$

LDH   Layered Double Hydroxides

LSPR   Localized Surface Plasmon Resonance

PTFE   Polytetrafluoroethylene

PZT   Lead Zirconate Titanate, $PbZr_xTi_{1-x}O_3$

SEM   Scanning Electron Microscopy

XRD   X-ray Diffraction

BACKGROUND

1.1 MOTIVATION

Piezoelectric materials find various applications including microphones and loudspeakers, ultrasound devices, transducers, sensors and actuators, and in energy harvesting [1–8]. Ferroelectric materials are a subset of piezoelectric materials characterized by a spontaneous, switchable polarization, and often display high piezoelectric coefficients [9]. Since the discovery of ferroelectricity by Valasek in 1920 [10], ferroelectric materials have gained increasing attention as more applications have become apparent. In addition to those mentioned above, capacitors, ferroelectric random access memory (FeRAM), and various forms of catalysis are potential applications of ferroelectric materials [11–18].

Lead zirconate titanate, $PbZr_xTi_{1-x}O_3$ (PZT), is the state-of-the-art commercial ferroelectric material today [19]. As PZT contains lead, which is toxic to humans and the environment, efforts are being made worldwide to find safer and more environmentally friendly alternatives, especially after an EU directive was issued in 2003, stating that lead is not to be used in electronics if a good substitute exists [20]. While several lead-free materials have been investigated, for instance $BaTiO_3$, $BiFeO_3$, and $K_xNa_{1-x}NbO_3$ (KNN), many of them display a lower piezoelectric coefficient than PZT and/or are challenging to process [21–24]. Hexagonal rare-earth manganites (h-$LnMnO_3$, where Ln denotes the rare-earth element) are a class of ferroelectric materials and a lead-free alternative to PZT [25, 26]. They display very high Curie temperatures (up to 1000 °C), making them a good choice for high-temperature applications [27–29]. In addition, they have received attention for being multiferroic with both ferroelectric and antiferromagnetic properties [30, 31], and might thus find applications for instance in antiferromagnetic memory devices [32]. While sol-gel and solid-state approaches to synthesize hexagonal manganites are well established, these methods typically require high synthesis temperature and/or several reaction steps [33]. However, several authors have reported low-temperature hydrothermal synthesis of hexagonal rare-earth manganites, using different precursors and reaction conditions [34–37]. The prospect of synthesizing lead-free ferroelectric materials like h-$LnMnO_3$ at low temperature and with water as solvent is very promising in terms of safety and environmental footprint, but a fundamental understanding of how these materials form and grow under hydrothermal conditions is lacking. As different applications

call for different product sizes and morphologies, such an understanding would be highly desired. For example, nanoparticles could be of interest for applications that benefit from large surface area, such as catalysis, as well as for down-scaling electronic devices. Particle morphologies may also influence the performance of ferroelectric materials. For instance, hollow nanocrystals of $CaTiO_3$ have been reported to exhibit good photocatalytic properties [38], and one-dimentional nanostructures of ferroelectric materials may be of interest in applications ranging from energy harvesting to FeRAM [39, 40]. Hence, further effort is required before hydrothermal synthesis of hexagonal rare-earth manganites with satisfying product control can be achieved. A better understanding of how these materials form under hydrothermal conditions would significantly improve our ability to tailor reaction products, and possibly allow us to move away from the trial and error approach that is common in development of lead-free ferroelectric materials today.

1.2   AIM OF THE WORK

This study aims to improve the understanding of the hydrothermal synthesis of hexagonal rare-earth mangantites. Several reaction parameters including temperature, hydroxide concentration, reaction time, and precursor type will be varied and their effect on the product composition and microstructure studied. The exploration of the temperature-pH parameter space in which h-LnMnO$_3$ can be formed is tied into this – knowledge of where the boundaries for h-LnMnO$_3$ formation lie will help determining the range over which the parameters can be varied and thus our ability to tailor the products. Such information also is of interest if an upscaling becomes relevant in the future, as the temperature and hydroxide concentration should not be higher than necessary from an economical and environmental perspective.

Two rare-earth elements with different radius, yttrium and ytterbium, will be investigated. The goal is to find out how hydrothermal synthesis of h-LnMnO$_3$ is affected by the choice of rare-earth element and other reaction parameters, and to explain possible differences between syntheses with yttrium and ytterbium. Particles of h-LnMnO$_3$ are aimed for, ideally with size and/or morphology depending on conditions during syntheses, which would allow for product tailoring. The products' dependence on rare-earth element and reaction conditions will be discussed, as will mechanisms of the h-LnMnO$_3$ formation.

INTRODUCTION

2.1 FERROELECTRIC MATERIALS AND THEIR APPLICATIONS

Unless otherwise stated, the content of the following section is based on Whatmore's [41] and Wang's [42] work.

Ferroelectric materials are a subset of dielectric, piezoelectric, and pyroelectric materials [43], as illustrated in Figure 2.1a. In addition to lacking inversion symmetry (which is a prerequisite for crystal structures to be piezoelectric) and possessing a unique symmetry axis (which characterizes the pyroelectric crystal structures), ferroelectric crystals exhibit a net polarization that can be switched upon the application of an external electric field. However, ferroelectric materials normally only adopt a crystal structure that allows for such a polarization at certain temperatures. Typically, such materials are paraelectric with a centrosymmetrical crystal structure at high temperatures, and undergo a symmetry-breaking transition to a ferroelectric structure at a critical temperature known as the *Curie temperature*, T_C. Such a transition is illustrated for the perovskte structure PZT in Figure 2.1b and 2.1c.

Because ferroelectric materials below their T_C have the ability to have their polarization switched by an external field, a characteristic curve known as a *hysteresis loop* results when such materials are exposed to an alternating electric field. An example is seen in Figure 2.1d. The exact shape of the hysteresis loop varies from material to material, but the qualitative behavior and general shape of the curve is common for all ferroelectric materials. In Figure 2.1d, two important characteristics of a ferroelectric material is marked: the *coercive field E_C*, which is the minimum field strength required to switch the polarization, and the *remanent polarization P_r*, which is the polarization that remains in the material when the external field is turned off.

The properties of ferroelectric materials lead to a wide range of potential applications. For instance, they typically have very high relative permittivities, yielding high capacitance when used as medium between the plates of a capacitor.

Furthermore, the hysteresis behavior of ferroelectric materials enable them to be used in FeRAM, where different polarizations are used to discriminate between 1 and 0 (as opposed to the presence or absence of current in conventional transistor based RAM) [11–13]. As FeRAM does not depend on electrical current, it has the advantage of being unrestricted by electron tunneling, potentially enabling a down-scaling

(a)

(b)

(c)

(d)
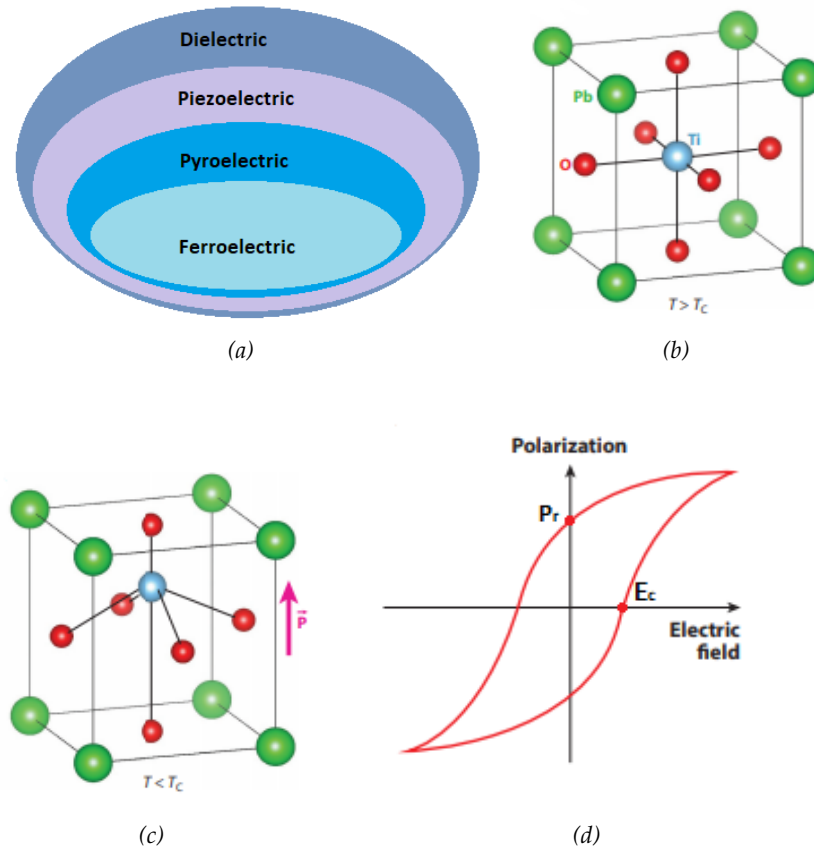
Figure 2.1: Illustration of important principles regarding ferroelectric materials.

(a) Schematic showing how ferroelectric materials are a subset of pyroelectric materials, which again are a subset of piezoelectric and dielectric materials.

(b) Schematic showing the high temperature paraelectric crystal structure of the common ferroelectric perovskite PZT. Above T_C, it displays inversion symmetry and is thus not piezoelectric or ferroelectric.

(c) The crystal structure of PZT below T_C. The cubic symmetry is broken, and the displacement of the central Ti^{4+} ion causes a net polarization across the unit cell. The displacement is greatly exaggerated in the figure for illustration.

(d) A hysteresis loop showing the induced polarization P in a typical ferroelectric material plotted against the externally applied electric field E. The coercive field E_C and the remanent polarization P_r are indicated.

Subfigures *(b)*, *(c)*, and *(d)* are adapted with permission from [42].

beyond what is predicted to be possible for conventional RAM and increasing the likelihood for Moore's law [44] to continue. For the same reason, it will also consume less power and generate less heat than current based RAM. Furthermore, FeRAM is non-volatile, and thus does not require continuous power supply to be sustained. Hence, FeRAM would even survive a power loss without loss of data.

More recently, ferroelectric materials have proven themselves very interesting in the field of catalysis. Piezoelectric particles exhibit catalytic properties on their own when subject to ultrasonic waves because the resulting strain improves transport of free charge carriers to the particles' surface [14, 15]. Because strain of piezoelectric particles is accompanied by polarization, ultrasound induces a slope in the conduction and valence bands, rendering the transport of charges to active facets more efficient. These charges can then reduce or oxidize species in the solution. In combination with illumination, however, the combined piezoelectric and photocatalytic properties of many ferroelectrics can be utilized because the number of electron/hole pairs is greatly increased by the incoming photons. The principle is illustrated in Figure 2.2a. Ferroelectric materials such as $BiFeO_3$, $BaTiO_3$, $KNbO_3$, and PZT have been successfully used in photocatalysis [16], and it has even been demonstrated that coating the ferroelectric particles with silver nanoparticles can enhance the effect further [17]. This enhancement was ascribed to the localized surface plasmon resonance (LSPR) effect the silver nanoparticles provide.
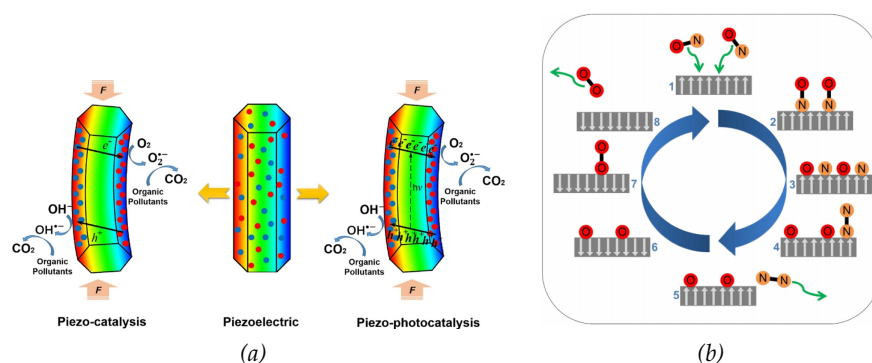
Figure 2.2: Conceptual schematics that show examples of how ferroelectric materials can be used for catalysis applications.
(a) Schematic on how the piezoelectric properties of a ferroelectric photocatalyst can be used to separate an electron/hole pair and transport the charges to active surfaces. Adapted with permission from [14].
(b) Use of ferroelectric materials for switchable catalysts. Switching the polarization alters the catalyst's affinities for reactants and products, allowing for adsorbtion and desorbtion in a cyclic manner. Reproduced with permission from [18].

Use of ferroelectric materials in novel, switchable catalysts has also been proposed [18]. The polarization of a ferroelectric material can

readily be controlled, and does in turn dictate the surface chemistry. Thus, Kakekhani et al. suggested that a heterogeneous catalyst with switchable reactant and product affinities can be constructed from these materials, as illustrated in Figure 2.2b [18]. Such a catalyst could exhibit great efficacy in converting reactants without the problems of catalyst poisoning and low product desorption rates that are often observed in catalysts that interact strongly with the reactants. Hence, by using ferroelectric materials it might one day be possible to avoid compromising between strong reactant interactions and weak product interactions, a compromise that is currently considered necessary according to the Sabatier principle [45].

2.2   HEXAGONAL RARE-EARTH MANGANITES

Unless otherwise stated, the content of this section is based on the work of Gibbs [27] and van Aken [30].

Hexagonal rare-earth manganites, h-LnMnO$_3$, are lead-free multiferroic materials with high Curie temperatures [25, 28] (for instance, $T_C = 1258 \pm 14$K has been reported for h-YMnO$_3$ [27]). An orthorhombic polymorph of LnMnO$_3$, o-LnMnO$_3$, also exists, but the hexagonal form is favored for Ln = Sc, Y, In, and the late lanthanides Ho-Lu. Hexagonal LnMnO$_3$ has a layered structure consisting of corner-sharing MnO$_5$ bipyramids and 8-coordinated Ln^{3+} ions between the MnO$_5$ layers, as shown for h-YMnO$_3$ in Figure 2.3. The room temperature structure belongs to the $P6_3cm$ space group, and is characterized by buckling of the MnO$_5$ bipyramid layers, leading to displacement of the Ln^{3+} ions and a net polarization from which the ferroelectricity arises. At high temperature, however, the structure is paraelectric and adopts the centrosymmetric $P6_3/mmc$ space group.

At 300 K, the lattice parameters of h-YMnO$_3$ are reported to be $a =$ 6.1483 and $c =$ 11.4432 [46], whereas the parameters of h-YbMnO$_3$ are reported to be $a = 6.0629$ Å and $c = 11.353$ Å [47, 48]. However, it should be noted that there are some deviations in the reported values - for instance, Lorentz reports the parameters of h-YbMnO$_3$ to be a = 6.062 Å and $c = 11.36$ Å [49], which is slightly different from the values reported by Liu et al. [47] and Fabrèges et al. [48].

In the Ln-Mn-O system, LnMn$_2$O$_5$ is the thermodynamically most stable phase at room temperature, and h-LnMnO$_3$ is only favored at high temperature (789 °C or above for Y [50] and about 850 °C or above for Yb [51]). High reaction temperatures are thus necessary if a solid state reaction approach is used. However, as will be discussed in Section 2.4.3, hydrothermal synthesis can yield h-LnMnO$_3$ at much lower temperatures.
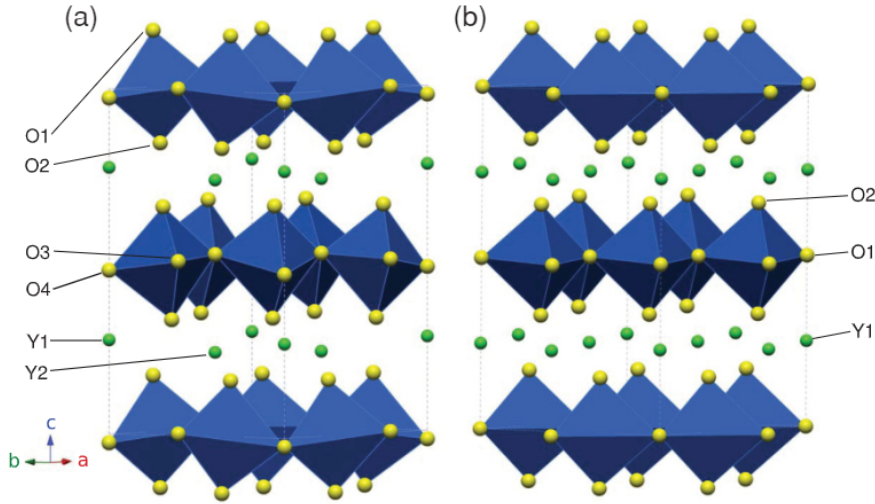
Figure 2.3: Schematic of the *h*-LnMnO$_3$ structure, here shown for *h*-YMnO$_3$. Reproduced with permission from [27].
(a) The ferroelectric room-temperature *P6$_3$cm* structure.
(b) The centrosymmetric high-temperature *P6$_3$/mmc* structure.

2.3 PRINCIPLES OF NUCLEATION AND GROWTH

Unless otherwise stated, the content of this section is based on de Yoreo and Vekilov's [52] and Cao and Wang's [53] work.

2.3.1 *Nucleation of crystals*

In classical nucleation theory, the change in Gibbs free energy upon nucleation is used to evaluate whether the process is spontaneous. The free energy can be split into a bulk term and a surface term. In the case of homogeneous nucleation of a spherical nucleus with radius r, the total change in free energy upon nucleation is given by

$$\Delta G_{nucl} = \frac{4}{3}\pi r^3 \Delta G_v + 4\pi r^2 \gamma, \tag{2.1}$$

where γ is the interfacial free energy per surface area on the formed nucleus and accounts for missing or disrupted intermolecular bonds for the surface molecules compared to bulk molecules. The interfacial free energy is positive for all solids (if it were negative, surfaces would be more energetically favorable than the bulk solid, meaning that the bulk would decompose to maximize surface area, and the solid would eventually completely vanish). ΔG_v is the change in Gibbs free energy per volume that nucleates. For a pure precipitation reaction, for instance, it is given by the difference in the free energy of a given volume in a nucleus and the free energy of the same volume of

solution, divided by that volume. In general, the change in free energy from a reaction is given by

$$\Delta G = \Delta G^0 + RT \ln Q, \tag{2.2}$$

where ΔG^0 is the standard state free energy change, T is the temperature, R the universal gas constant, and Q the reaction quotient [54]. Since Q in a nucleation reaction decreases when the reactant concentration increases, ΔG_v will eventually become negative once the reactant concentrations become large enough. According to 2.1, this means negative ΔG_{nucl} for sufficiently large nuclei, so that nucleation will lower the total free energy of the system if large enough nuclei can form.

However, nucleation can be prohibitively slow even when it is in principle spontaneous. Since the interfacial free energy is always positive, the second term of Equation 2.1 is positive and will dominate for small r. Thus, the free energy change will have a maximum, ΔG^*_{nucl}, which acts as an energy barrier that must be overcome, and a forming nucleus must reach a critical radius r^* before it is expected to keep growing rather than dissolving. These critical values are found by differentiating 2.1 with respect to r:

$$r^* = -\frac{2\gamma}{\Delta G_v}, \tag{2.3}$$

$$\Delta G^*_{nucl} = \Delta G_{nucl}(r^*) = \frac{16\pi}{3} \cdot \frac{\gamma^3}{\Delta G_v{}^2}. \tag{2.4}$$

When ΔG^*_{nucl} is inserted as the activation energy in a simple Arrhenius expression, an expression for the nucleation rate J_{nucl} is obtained:

$$J_{nucl} = A \exp\left(-\frac{\Delta G^*_{nucl}}{RT}\right) = A \exp\left(-\frac{1}{RT} \cdot \frac{16\pi}{3} \cdot \frac{\gamma^3}{\Delta G_v{}^2}\right), \tag{2.5}$$

where A is a system specific constant. If the assumption of spherical nuclei is relaxed, the geometrical factor $\frac{16\pi}{3}$ can be replaced by a different one, but the same principles still apply. Furthermore, if the nucleation is heterogeneous, γ is replaced by $\frac{2\gamma_{lc}+\gamma_{sc}-\gamma_{ls}}{2}$, where γ_{lc} is the interfacial free energy at the liquid/crystal interface, γ_{sc} at the substrate/crystal interface, and γ_{ls} at the liquid/substrate interface. Since this substitution typically results in a lower value than in the homogeneous case, heterogeneous nucleation is expected to be faster than homogeneous according to Equation 2.5, in agreement with heterogeneous nucleation being observed more frequently than homogeneous [55].

Modern experiments have indicated that the nucleation process can proceed through intermediate stages before a thermodynamically stable nucleus is formed [56]. Thus, nonclassical models based on

primary nanoparticles forming, aligning, and aggregating into larger particles [57] should also be briefly mentioned. It has been proposed that primary nanoparticles may form by aggregation of *pre-nucleation clusters*, amorphous or nano-crystalline assemblies of atoms [58]. Contrary to classical nucleation theory, it has also been proposed that colloidal rather than thermodynamical stability sometimes determines the smallest stable particle size [59].

2.3.2 *Growth of crystals*

When a nucleus has exceeded the critical formation radius, it will keep growing to minimize the free energy of the system. Small growth species (*monomers*) adsorb on the growing surface, migrate to sites of high energy such as steps, kinks, and defects, and are incorporated there. When the driving force[1] for growth is weak, i.e. when the free energy of the growing phase is only slightly lower than that of the reactants, new growth layers depend on defects to form. Once a layer has formed, it will propagate in a step-wise manner across the surface. This is because sites in and adjacent to the step have higher energy than sites outside the growing layer, such that it is more energetically favorable for the monomers to be incorporated there.

At stronger driving force, however, *2D nucleation* becomes more prominent. It is a process where a monomer is incorporated on top of an existing layer without the help of an existing kink, step, or defect, and leads to rougher surfaces than the step-by-step growth that takes place at lower driving force because several layers can form and grow at the same time.

When the driving force is even stronger, the growth rate is restricted by the mass transport of the monomers to the surfaces rather than incorporation. Typically, the result is rapid growth in regions that are easily accessible to the monomers, such as corners and edges of the growing crystal. Dendrite formation often results.

The growth will continue as long as the reaction conditions in the system such as temperature and reactant concentrations can sustain it. Unless more reactants are continuously added to the system, the reactant concentrations will decrease as the growth proceeds, gradually weakening the driving force until in practice no growth occurs. However, the crystals will often be subject to changes in size even after the primary growth has stopped. *Ostwald ripening* is a mechanism by which this can occur. The mechanism involves large particles growing at the expense of smaller ones, which will eventually dis-

---

1 In pure precipitation reactions, supersaturation is often used as a measure of the driving force for nucleation and growth, but the term driving force is used here to preserve generality for solid phase-transitions and reactions between solid(s) and solute(s).

solve completely. Lower total surface area and thus lower total energy results.

It should further be mentioned that other chemical species than the reactants may affect the growth. Examples include surfactants adsorbing to the crystal/solution interface to lower the interfacial energy and impurities inhibiting growth through mechanisms such as step pinning, kink blocking, and impurity incorporation.

Non-classical growth models also exist. For instance, oriented attachment of primary nanoparticles and of temporarily stabilized mesocrystals have been mentioned as possible alternative growth routes to classical growth [58].

2.3.3   *Mechanisms for hollow crystallite formation*

Hollow crystallites, i.e. crystallites that are *not* topologically equivalent to spheres, sometimes form instead of dense ones, and this can occur by various mechanisms. Techniques based on sacrificial templates aside, Weng et al. [60] state three mechanisms in a 2018 review paper; the Kirkendall effect, oriented attachment, and inside-out Ostwald ripening.

The Kirkendall effect arises from a net vacancy flux due to different diffusion rates between two interdiffusing species [61]. If a phase, say A, is deposited on originally dense nanoparticles of another phase B, and the diffusibility of B in A is greater than that of A in B, a net flux of matter from the core and outwards and thus a hollow core can result [62, 63]. The effect is sometimes seen in combination with *galvanic replacement*, another mechanism by which hollow nanostructures can form [61, 64]. When metal particles are exposed to dissolved precursors of a more noble metal, the noble precursors are reduced and deposit on the less noble metal particles, which are oxidized and evacuate the structure, for instance through pinholes, with hollow structures as the result [64]. The effect may be especially pronounced if the noble precursors have a higher valency than the ions the less noble metal is oxidized into, as more metal atoms from the core then dissolve for each atom that is deposited.

Oriented attachment of primary (and dense) nanoparticles into hollow structures is an entirely different mechanism by which such crystallites can form. For instance, Wannapop et al. hydrothermally synthesized hierachical donut-like structures composed of nanosheets aggregating in a layered fashion [65].

It has also been reported that dense structures can turn hollow after the primary growth by means of inside-out Ostwald ripening. This has for instance been seen for various oxide materials such as SnO_2 [66], anatase TiO_2 [67], and Cu_2O [68]. The formation of hollow structures through Ostwald ripening is perhaps a counterintuitive result, as the driving force behind Ostwald ripening is lowering the

surface energy and hollow particles are expected to have a larger total surface area than dense particles of the same size. However, it has been proposed that primary crystallites constituting the particle are smaller or more loosely packed near the core [66, 69], and thus dissolve more easily than the primary particles constituting the exterior. Another hypothesis is that the degree of crystallinity may tend to decrease towards the core, and that it costs less energy to dissolve the more amorphous core than the crystalline exterior [66]. The process of inside-out Ostwald ripening is illustrated in Figure 2.4a.

Yet another mechanism for formation of hollow particles has been proposed by Budhysutanto et al. [70], and is schematically illustrated in Figure 2.4b. Using a hydrothermal method with microwave heating, they synthesized donut-like crystals of Al-Mg layered double hydroxides LDH. They proposed a growth mechanism where dissolved $Al(OH)_3$ reacts on the surface of insoluble MgO spheres to form Mg-Al LDH. Since the supersaturation of Mg^{2+} is highest near the surface of the MgO particles, the LDH will grow laterally around the MgO particles, which gradually dissolves, rather than growing radially, and a donut-like structure results once the MgO has completely dissolved.

(a)   *(b)*
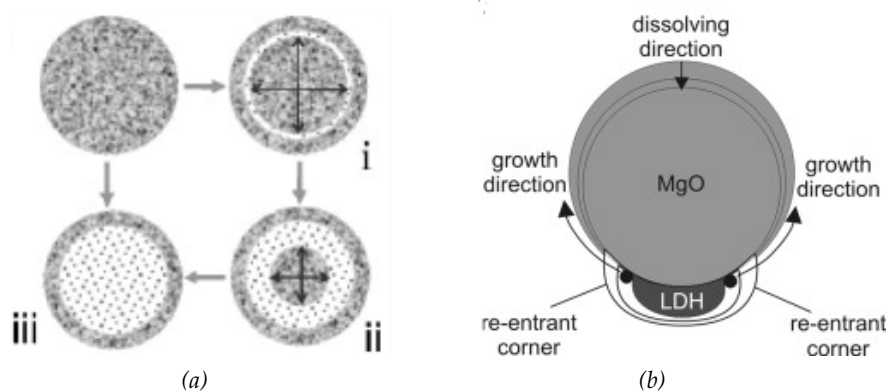
Figure 2.4: Two different mechanisms for how hollow particles can form.
(a) Inside-out Ostwald ripening. Starting from a dense particle, the interior is gradually dissolved. It can start dissolving near the particle's surface and proceed inwards (i-iii), or start near the particle's core and proceed to (iii) directly. Adapted with permission from [66].
(b) Formation of a hollow LDH particle around a MgO core that later dissolves. Due to higher supersaturation of Mg^{2+} in the proximity of the MgO particle, the LDH grows laterally around it. The MgO particle in turns dissolves as the Mg^{2+} surrounding it is consumed, leaving a hollow LDH particle. Adapted with permission from [70].

2.4   HYDROTHERMAL SYNTHESIS

2.4.1   *Principles of hydrothermal synthesis*

Hydrothermal synthesis is a special case of the solvothermal synthesis, characterized by water being the solvent. The method is simple and scalable, and involves mixing precursors and water (and possibly other additives such as mineralizer or surfactant) in a sealed pressure vessel known as an *autoclave*, see Figure 2.5a. Typically, the autoclave consists of a steel casing designed to withstand high pressures with an inert Teflon liner inside to avoid contact between the steel casing and the reactants. Reaction conditions at elevated temperature and pressure can thus be achieved simply by heating the autoclave in an oven. Under such conditions, many of the properties of water change, including density, viscosity, ionic product, and dielectric constant [71]. These changes can be favorable in several ways - for instance, reduced viscosity allows for more efficient mass transport, and the significant decrease in dielectric constant enhances the solubility of non-polar species. Furthermore, salts that are insoluble in water at room temperature may be soluble at higher temperatures.

While the critical point of water is at about 374 °C, Teflon lined autoclaves typically cannot withstand higher temperatures than about 270 °C [72]. Thus, supercritical conditions are rarely seen for hydrothermal syntheses compared to solvothermal syntheses using a solvent with a lower critical point than water. Nevertheless, the filling factor of the autoclave and the temperature of the oven it is placed in can easily be adjusted, allowing for good control of the reaction environment, as illustrated in Figure 2.5b.
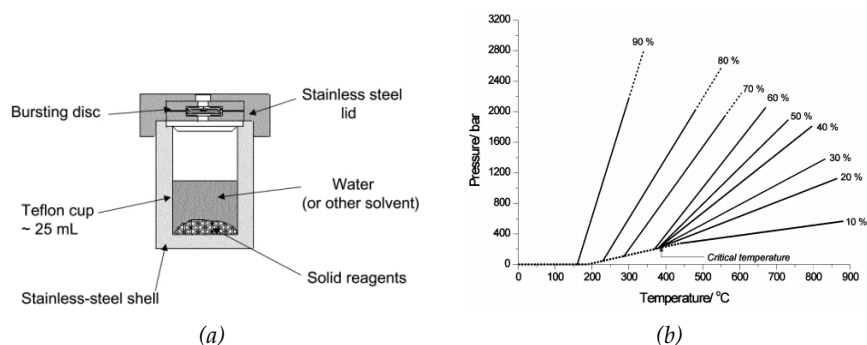
Figure 2.5: (a) Schematic showing an autoclave with a typical content consisting of solid precursors and solvent. Dissolved precursors can also be used. *(b)* Pressure as a function of temperature for several different autoclave fill factors. These pressures are for pure water.
Both subfigures reproduced with permission from [72].

Temperature and pressure are not the only parameters that can be controlled and used to tailor the products. Some of the parameters

reported to affect the products of hydrothermal synthesis are briefly discussed in Section 2.4.2.

2.4.2 *Parameters affecting hydrothermal reactions*

In a review of hydrothermal reactions and growth of complex oxide systems, mainly perovskites, Gersten [73] has summarized several trends regarding how different parameters influence reaction products.

Temperature is reported to influence the crystallite size in a somewhat inconsistent manner depending on other reaction conditions [74], which is perhaps not so surprising considering that the driving forces for nucleation and growth have a complex temperature dependence. For instance, the nucleation rate in Equation 2.5 exhibits an explicit temperature dependence that applies for all material systems and accounts for greater fluctuations at high temperature and thus higher probability of forming a sufficiently large nucleus, but it also has a more complicated and material-specific temperature dependence because ΔG_v and γ depend on temperature. The morphology, however, seems to display a somewhat more consistent temperature dependence in the material system Gersten [73] reviews, the tendency being rounder crystallites at lower temperatures [75].

Precursor concentration is reported to influence the crystallite size. Typically, a decrease in crystallite size results from an increase in precursor concentration [76]. An explanation could be high concentration leading to high supersaturation and thus faster nucleation, yielding many small crystallites rather than few large ones.

According to Gersten [73], increased pH is consistently reported to result in increased particle size. However, smaller particles resulting from higher pH has also been reported [74], as has inconsistency in how the pH affects the particle size [77]. The pH is also found to significantly affect product morphology [74, 78], but once again a trend independent of other reaction conditions seems difficult to find.

Intuitively, it is found that longer reaction time leads to larger crystallites [77]. Ostwald ripening and increased time for primary growth are both possible explanations.

Precursor size and morphology is also found to affect the size and morphology of the product in several studies; the tendency is similar sizes and morphologies for product and precursor [79–81]. Such an effect is expected when the hydrothermal reaction is an *in situ transformation*, i.e. when a reaction takes place on a solid precursor's surface and the product diffuses inwards, eventually transforming the entire precursor into a new phase. For a pure *dissolution-precipitation* mechanism, where the precursors release ions and are completely dissolved while products precipitate from the solution, the size and shape of the precursors will not necessarily affect the size and shape of the products. However, a correlation cannot be excluded in this case

either. For instance, larger precursors will lead to slower release of ions, which can in turn lead to slower nucleation and larger products. If the hydrothermal reaction in question is not a pure dissolution-precipitation reaction, using anisometric precursors is one of the most important methods to induce anisotropic growth of products [71]. Such control is particularly important when the target product does not have an anisotropic crystal structure that will direct the growth in the desired direction.

2.4.3 *Hydrothermal synthesis of rare-earth manganites*

Several authors have demonstrated that particles of hexagonal rare-earth manganites can be successfully synthesized by means of low-temperature hydrothermal synthesis. For instance, Stampler et al. hydrothermally synthesized plate-like and needle-like crystallites of h-LnMnO$_3$ by mixing solid Ln$_2$O$_3$ and Mn$_2$O$_3$ with water or hydroxide solution, and investigated how the products depended on Ln element, pH, reaction temperature, and reaction time [34]. They suggested that the formation of hexagonal manganites is due to a reaction between rare-earth oxyhydroxide, LnOOH, and a soluble hydroxomanganite complex, Mn(OH)$_4^-$. At a certain temperature that is determined for several different Ln elements by Klevtsov and Sheina [82] , Ln(OH)$_3$ (which is formed in a reaction between rare-earth oxide and water) undergoes a transition to the more reactive LnOOH upon release of water. The temperatures at which this transition occurs for different lanthanides are shown in Figure 2.6.

The transition temperature is strongly correlated with the ionic radius of the Ln element; the higher the radius, the higher the transition temperature. A possible explanation is small cations exhibiting stronger Lewis acidity and pulling the anions' electrons more strongly than large cations do, thus destabilizing the Ln(OH)$_3$ phase and favoring release of water. The coordination numbers of the LnOOH phase and the Ln(OH)$_3$ phase, 7 and 9, respectively [83], may also contribute to this trend. Because the repulsion between the negative hydroxide ions in the Ln(OH)$_3$ phase is stronger when the Ln ion is small, it is to be expected that the transition to the lower-coordinated LnOOH phase occurs more readily for small rare-earth elements.

Stampler et al. also found that neutral pH does not result in formation of h-LnMnO$_3$, and only yields a mixture of Ln(OH)$_3$ and LnOOH, which probably can be attributed to Mn$_2$O$_3$ failing to dissolve in water when the pH is too low for Mn(OH)$_4^-$ to form.

In an in situ study of hydrothermal synthesis of h-YMnO$_3$ from the same oxide precursors used by Stampler et al., Marshall et al. [33] investigated reaction rates and intermediate products at different temperatures and pH. They found that the dehydration from Y(OH)$_3$ to YOOH discussed by Stampler is faster not only at higher tempera-
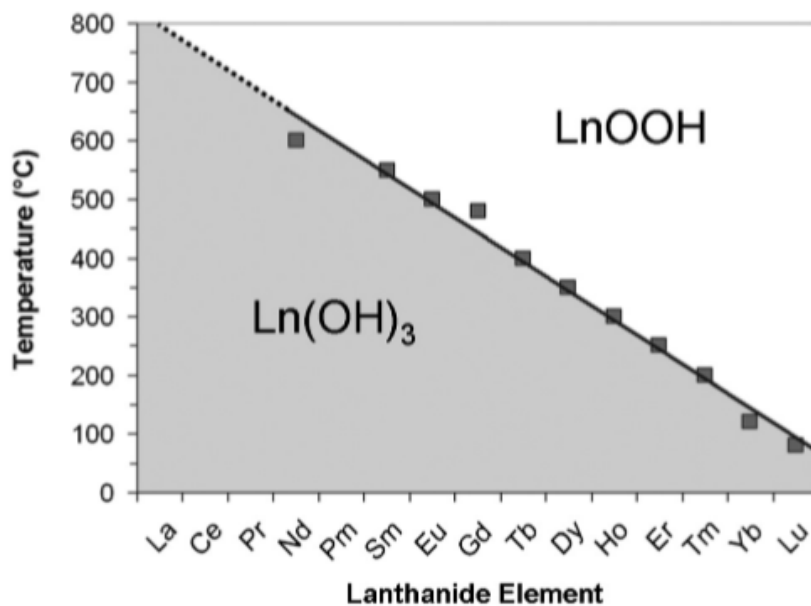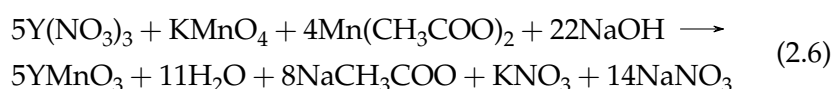
Figure 2.6: Dehydration temperature for several rare-earth hydroxides in 2.5 M NaOH solution, determined by Klevtsov and Sheina [82] and represented graphically by Stampler et al. [34]. Reproduced with permission from [34].

ture, but also at higher pH, indicating that hydroxide plays a role in favoring the dehydration in addition to dissolving Mn_2O_3.

Harunsani et al. reported hydrothermal synthesis of h-YMnO$_3$ platelets from Y(NO$_3$)$_3$, MnCl$_2$, KMnO$_4$, and KOH at 240 °C overnight [35]. This temperature is lower than the transition temperature from Y(OH)$_3$ to YOOH that was reported by Stampler et al. (300 °C), indicating that the h-YMnO$_3$ is formed by a different mechanism when synthesized from Harunsani's soluble salt precursors than from Stampler's oxide precursors, although the different results could also be owing to possible dissimilarities in other parameters such as pH, concentration, or pressure inside the autoclave.

Zheng et al. [36] have also reported successful hydrothermal synthesis of h-YMnO$_3$ from the same soluble salt precursors as Harunsani et al., although no measure taken to increase the pH is mentioned. They reported formation of h-YMnO$_3$ nanoparticles when an autoclave with 70 % fill factor was heated at 230 °C for 2 days.

Also using salt precursors (although Mn(CH$_3$COO)$_2$ was used instead of MnCl$_2$) and a pH of 9.2, Kumar et al. have reported synthesis of h-YMnO$_3$ nanorods during hydrothermal treatment at 200 °C for 2 days [37]. An autoclave fill factor of 80 % was used. They proposed a one-step mechanism directly from dissolved ions:

$$5Y(NO_3)_3 + KMnO_4 + 4Mn(CH_3COO)_2 + 22NaOH \longrightarrow$$
$$5YMnO_3 + 11H_2O + 8NaCH_3COO + KNO_3 + 14NaNO_3$$

(2.6)

The hydrothermal synthesis of ytterbium manganites was also investigated in the author's specialization project, where h-YbMnO$_3$ was successfully formed at temperatures down to 190 °C [84]. Emphasis was put on chloride and nitrate precursors, but oxide precursors were also used. The goal was to identify the impact of different reaction parameters on the final product. High temperature and high hydroxide concentration were found to favor manganite formation, as well as to result in smaller particles. Oxide precursors were also observed to result in larger particles than salt precursors.

As this review shows, low-temperature hydrothermal synthesis of rare-earth manganites is indeed possible, and will be investigated further in the following.

EXPERIMENTAL

3.1 CHEMICALS

The purity and manufacturer of all chemicals used in syntheses are given in Table 3.1.

KOH and the oxides were used as received. Solutions were prepared from the nitrate and chloride salts, and the concentration of the solutions are given in Table 3.2. The concentration of the $KMnO_4$ solutions were simply obtained by measuring the quantities of salt and deionized water used to prepare the solutions. As the other salts are hydrates and thus have a greater uncertainty in their molar masses, the concentration of the $Y(NO_3)_3$, $MnCl_2$, and $Yb(NO_3)_3$ solutions were obtained by thermogravimetric standardization. A small amount of solution was transferred to crucibles with kaolinite wool, dried, and calcined at an appropriate temperature to convert all cations into a single metal oxide (600 °C, 1000 °C, and 1150 °C for Mn_2O_3, Yb_2O_3, and Y_2O_3, respectively).

Table 3.1: The purity and manufacturer of the chemicals used in the syntheses.

Chemical	Manufacturer	Purity [%]
Yb_2O_3	Sigma Aldrich	99.9
Mn_2O_3	Sigma Aldrich	99
Y_2O_3	Alfa Aesar	99.9
KOH	Sigma Aldrich	90
$MnCl_2 \cdot 4\,H_2O$	Sigma Aldrich	99
$KMnO_4$	Sigma Aldrich	99
$Yb(NO_3)_3 \cdot xH_2O$	Alfa Aesar	99.9
$Yb(NO_3)_3 \cdot 5\,H_2O$	Sigma Aldrich	99.9
$Y(NO_3)_3 \cdot 6\,H_2O$	Sigma Aldrich	99.8

Table 3.2: The concentration of the solutions used in the syntheses. The change in manufacturer for $Yb(NO_3)_3$ was only done due to availability, and is not expected to impact the products as the salts are completely dissolved in the precursor solutions. SA = Sigma Aldrich, AA = Alfa Aesar.

Solution	$MnCl_2$	$KMnO_4$	$KMnO_4$	$Y(NO_3)_3$	$Yb(NO_3)_3$	$Yb(NO_3)_3$
Concentration [M]	0.48	0.12	0.28	0.38	0.40	1.3
Manufacturer	SA	SA	SA	SA	AA	SA

3.2   HYDROTHERMAL SYNTHESIS

Two different experimental procedures were used for mixing the precursors, depending on precursor type. They are represented schematically in Figure 3.1.

In the syntheses from oxide precursors, equimolar amounts of Mn_2O_3 and Ln_2O_3 were ground together using mortar and pestle, then added to a 23 mL polytetrafluoroethylene (PTFE) liner. Deionized water was then added to the liner, and the mixture was stirred for about 10 min. Then, KOH was added, and the mixture was stirred for another 30 min before the liner was placed in a stainless steel casing and transferred to a preheated oven.

For the salt precursors, solutions of $Ln(NO_3)_3$ and $KMnO_4$ were first added to a 23 mL PTFE liner and stirred for about 10 min. KOH was
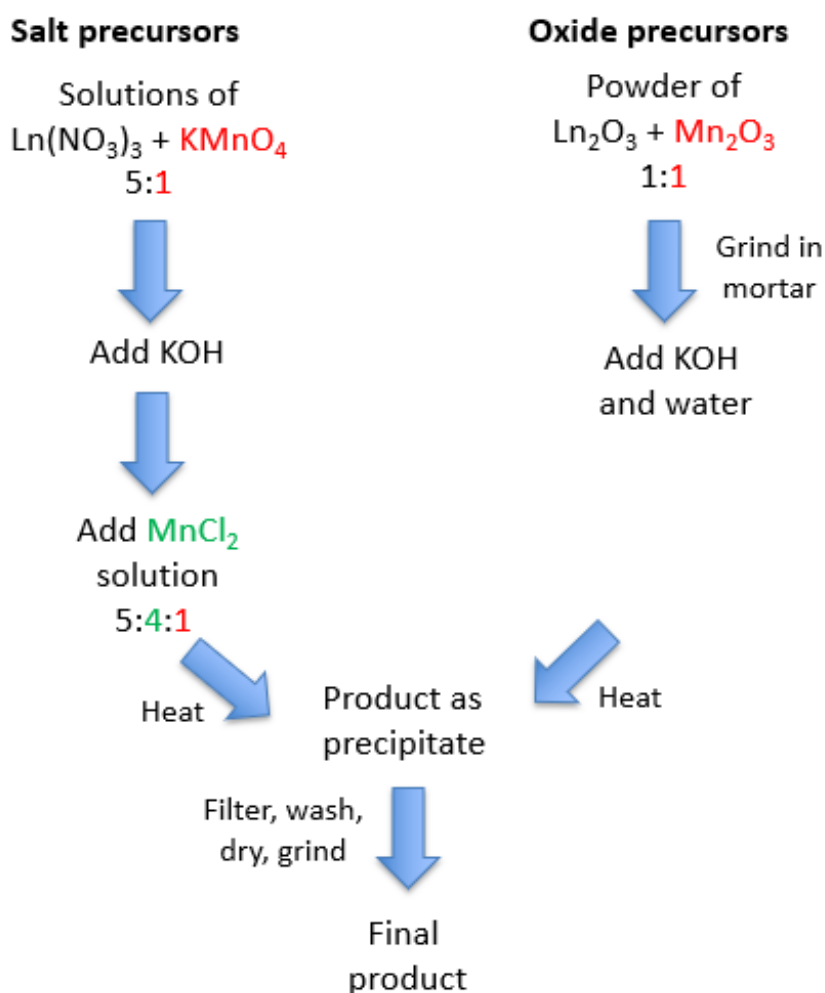
Figure 3.1: Illustration of the experimental procedures for synthesis from oxide and salt precursors. In addition to the steps illustrated, the mixtures were stirred after each chemical was added. The ratios indicated are stochiometric ratios.

then added and the mixture stirred for another 30 min. Finally, $MnCl_2$ solution was added, the mixture stirred for 30 min, and the liner placed in a stainless steel casing (Parr 4749 General Purpose Vessel [85]) and transferred to a preheated oven. The stochiometric ratio of $Ln(NO_3)_3$, $MnCl_2$, and $KMnO_4$ was 5:4:1 in each synthesis, ensuring equal total amounts of Ln and Mn and also an initial average oxidation state of +3 for Mn, which is the oxidation state of Mn in h-$LnMnO_3$. While the amount of KOH relative to the other precursors was varied, OH^- was always in excess according to Equation 2.6 proposed by Kumar et al. [37].

Type of rare-earth element, precursor type, concentration[1] of OH^- and of the rare-earth element (and thereby also of manganese due to fixed stochiometric ratio), as well as the reaction temperature and time for each reaction, are given in Table 3.3. The synthesis IDs consist of the rare-earth element and the hydroxide concentration used, as well as an enumeration to distinguish between different syntheses with similar rare-earth element and hydroxide concentration. Syntheses from salt precursors were conducted with 0.4 M $Ln(NO_3)_3$ and 0.12 M $KMnO_4$. The only exceptions are the syntheses with 0.31 M Ln^{3+}, which were prepared with 1.3 M $Yb(NO_3)_3$ and 0.28 M $KMnO_4$ (see Table 3.2), as well the Yb5-21 synthesis, which is otherwise identical to the Yb3-21 and the repeat Yb4-21 syntheses and was carried out to reveal possible differences arising from change in solution batches. In all syntheses except Y-11, the autoclave fill factor was about 50 % (precursor solutions with a total volume of 9.7-10.5 mL as well as 0.5-11.5 g KOH depending on synthesis were added to a 23 mL liner). The Y-11 synthesis was carried out at higher temperature than PTFE lined autoclaves typically can withstand [72], and a high temperature autoclave (Parr 4760 General Purpose Vessel [86], 100 mL, heated by a Parr 4838 Reactor Controller [87] instead of in an oven) was thus used. The autoclave was made of Monel 400, which is an alloy of copper and nickel [88]. As a safety measure, the fill factor was lowered to about 30 % for this synthesis because the autoclave had never been used with nitrate precursors before. This was done to ensure that the pressure would not exceed what the autoclave could withstand even in the event of NO_x formation due to nitrate decomposition.

For all syntheses, the autoclave was allowed to cool to room temperature after the hydrothermal heat treatment before the product was collected by suction filtration and washed several times with deionized water. The products were then dried at 110 °C for 3-4 h before being ground to a fine powder using mortar and pestle and stored for future

---

1 The concentrations were calculated by dividing the total amount of hydroxide or rare-earth element by the total volume of *liquid* added to the liner. However, the addition of solid hydroxide (and of Ln_2O_3 and Mn_2O_3 for the syntheses from oxides) leads to a slight volume increase. Thus, the true concentrations will be somewhat lower than those given in Table 3.3, especially in syntheses with a high amount of KOH.

characterization. Ovens of the Termaks TS9000 series were used both for hydrothermal heat treatment and for drying.

Table 3.3: ID and description of the syntheses performed. Concentrations of OH^- and Ln^{3+} are calculated from the amount of precursors added and the combined volume of the precursors solutions. For all reactions with salt precursors, the initial stochiometric ratio in the autoclave was Ln^{3+}: Mn^{2+}: Mn^{7+} = 5:4:1. For oxide precursors the ratio was Ln^{3+}: Mn^{3+} = 1:1.

ID	Ln element	Precursor type	$[Ln^{3+}]$ [M]	$[OH^-]$ [M]	$T_{reaction}$ [°C]	Time [h]
Yb-0.9	Yb	Salt	0.17	0.93	130	24
Yb1-11	Yb	Salt	0.17	10.6	110	24
Yb2-11	Yb	Salt	0.17	10.6	130	24
Yb3-11	Yb	Salt	0.17	10.6	130	72
Yb4-11	Yb	Salt	0.17	10.6	150	24
Yb5-11	Yb	Oxide	0.17	10.6	150	24
Yb6-11	Yb	Salt	0.31	10.6	240	24
Yb1-21	Yb	Salt	0.17	21.2	110	24
Yb2-21	Yb	Salt	0.17	21.2	130	24
Yb3-21	Yb	Salt	0.17	21.2	150	24
Yb4-21*	Yb	Salt	0.17	21.2	150	24
Yb5-21*	Yb	Salt	0.17	21.2	150	24
Yb6-21	Yb	Oxide	0.17	21.2	150	24
Yb7-21	Yb	Salt	0.17	21.2	240	24
Yb8-21	Yb	Salt	0.17	21.2	240	72
Yb9-21	Yb	Salt	0.31	21.2	240	24
Y-11	Y	Salt	0.17	10.6	300	24
Y-16	Y	Salt	0.17	15.9	240	24
Y1-21	Y	Salt	0.17	21.2	240	6
Y2-21	Y	Salt	0.17	21.2	240	24
Y3-21	Y	Salt	0.17	21.2	240	48
Y4-21	Y	Salt	0.17	21.2	240	72
Y5-21	Y	Oxide	0.17	21.2	240	72

*Repeats of Yb3-21

3.3 CHARACTERIZATION

3.3.1 *X-ray diffraction*

All samples were characterized by X-ray Diffraction (XRD) in a Bruker
D8 A25 DaVinci X-ray diffractometer with Cu K-α radiation. A 2θ
range from 10 to 80 degrees and a fixed divergence slit of 0.2 degrees
was used for all samples.

To obtain information about phase purity, lattice parameters, and
other phases present, Rietveld refinements were carried out on the
manganite products using the Bruker TOPAS software [89]. A fifth
order Chebychev polynomial was used initially for the background.
Then, after finding all phases, the order of the Chebychev polynomial
was increased until the background was properly fit (typically, a
polynomial of order 8-10 was necessary). The order was increased
after finding the phases to reduce the risk of small peaks being fit as
part of the background. Lattice parameters and Lorentzian volume
weighted mean crystallite size (L Vol IB, obtained from measured
integral breadth) were refined for each phase. In addition, preferred
orientation was refined for phases expected to have highly anisometric
particle morphology. For the hexagonal rare-earth manganite phases,
displacements from the high-temperature unit cell positions of the
atoms were refined as well to account for h-LnMnO$_3$ being below T_C
at room temperature. Furthermore, the Stephens hexagonal model
was used to be able to refine possible anisotropic peak broadening
from anisometric particles [90].

3.3.2 *Scanning electron microscopy*

Scanning electron microscopy (SEM) was performed on the products
confirmed by XRD to contain an appreciable amount (30 wt% or more)
of h-LnMnO$_3$. The products were characterized in a field emission
scanning electron microscope (Zeiss Ultra 55 limited edition or Zeiss
Supra 55 VP). A small amount of product powder was dispersed in
ethanol in an ultrasonic bath for 2 min, and an aperture size of either
10 or 20 µm and a 10 kV acceleration voltage were used. The images
were generated from secondary electron detection.

Whereas the SEM images were only used to qualitatively assess the
morphology and approximate size of the particles for most products,
quantitative measurements of particle diameter (and hole diameter
where applicable) were carried out on several particles in the Y1-21,
Y2-21, Y3-21, and Y4-21 products. For hexagonal particles, the particle
diameter was measured along the long diagonal, corner to corner (see
Figure A.1 in Appendix A). For particles with interior clearly in the
process of dissolving, the diameter of the dissolving area was used as
the hole diameter (see Figure A.2).

3.3.3 *Energy-dispersive X-ray spectroscopy*

In order to determine whether each particle consisted of one or several phases, energy dispersive X-ray spectroscopy (EDXS) was carried out on the Y1-21 sample. The powder was dispersed in ethanol in the same manner as described in Section 3.3.2 and in addition coated with carbon. Al-Mg sample holders were used. The Zeiss Ultra 55 limited edition microscope was run in high current mode with an aperture size of 60 μm and 15 kV acceleration voltage. Spot analysis was performed on multiple locations on several particles. The resulting spectra were analyzed using Bruker ESPRIT 1.9 software, yielding atom percentages of Y, Mn, and O at each spot (contributions from Al and Mg from the sample holder and C from the coating were disregarded and the percentages re-normalized).

RESULTS

4.1 PRODUCT COMPOSITION

Both h-YMnO$_3$ and h-YbMnO$_3$ were successfully formed using several different sets of reaction parameters. Key results from the XRD analysis and Rietveld refinements of the products are presented in the following, organized by the reaction parameters' effect. Main phases are given as well as their weight percentage obtained from Rietveld refinements. Full product compositions with minor phases included can be found in Appendix B. All X-ray diffractograms are given in Appendix C.

The three parallels with reaction conditions as in the Yb3-21 synthesis will be examined in Section 4.1.7. In the following, the average h-YbMnO$_3$ phase purity of 76% will be used as the value for those reaction conditions (150 °C, 21.2 M KOH, 0.17 M Yb^{3+}, 24 h, salt precursors).

4.1.1 *The effect of temperature*

Phase purity of h-YbMnO$_3$ is plotted as a function of temperature for two different hydroxide concentrations in Figure 4.1. Within each series, all reaction parameters except temperature are kept constant. An increase in h-LnMnO$_3$ phase purity resulting from increased temperature is seen for both hydroxide concentrations. For the products synthesized with 21.2 M KOH, the phase purity strongly increases from 110 °C to 130 °C, then slowly increases to 240 °C. With 10.6 M KOH, the increase appears to be stronger than with 21.2 M KOH at low temperatures. The phase purity seems to become similar for both hydroxide concentrations around 150 °C, although experiments to determine whether the purities remain similar for both hydroxide concentrations at higher temperatures than 150 °C have not been conducted in this study.

The major phases of each of the products included in Figure 4.1 are given in Table 4.1 (the full compositions are given in Appendix B). As the temperature is increased, a clear decline in the YbOOH content is observed in addition to the increase in h-YbMnO$_3$ content. The Mn$_3$O$_4$ phase, in which manganese has an average oxidation state of +2.67, also seems to become less prominent as temperature increases. Further, the Mn^{4+} containing phases YbMn$_2$O$_5$ and Yb$_2$Mn$_2$O$_7$ are observed in appreciable amounts only at 240 °C.
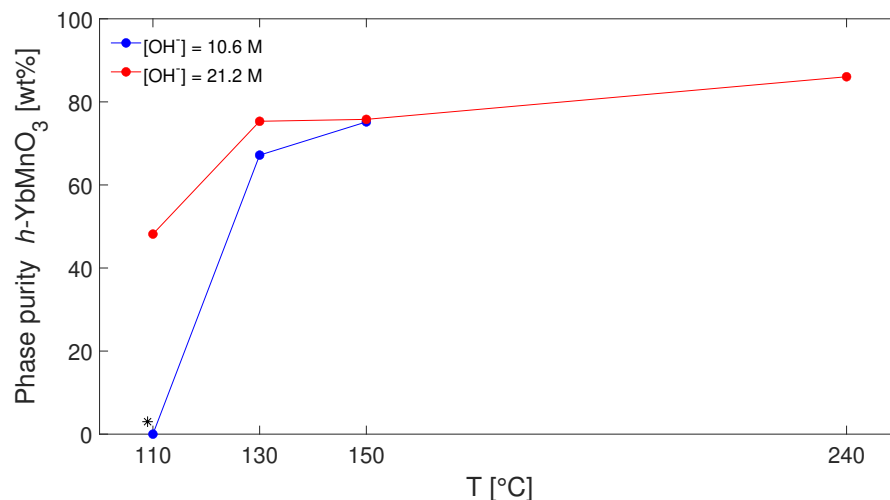
Figure 4.1: Phase purities of h-YbMnO$_3$ as a function of reaction temperature for two different hydroxide concentrations. Syntheses with hydroxide concentration of 10.6 M (Yb1-11, Yb2-11 and Yb4-11) are in blue, syntheses with 21.6 M KOH (Yb1-21, Yb2-21, the average of Yb3-21 to Yb5-21, and Yb7-21) in red. Apart from temperature and hydroxide concentration, all reaction parameters are identical for all syntheses included in this figure.
*Some h-YbMnO$_3$ may be present or in the process of forming, see below.

Table 4.1: Product composition (in wt%) as a function of temperature. Hydroxide concentration can be read out of the synthesis ID, and reaction temperature is given in the table. Apart from those two parameters, all syntheses were performed under identical conditions. Full compositions are given in tables B.1 and B.7.

ID	T [°C]	Main phases	Rwp
Yb2-11	130	h-YbMnO$_3$ (67%), YbOOH (20%), Mn$_3$O$_4$ (11%)	9.4
Yb4-11	150	h-YbMnO$_3$ (75%), YbOOH (18%), Mn$_3$O$_4$ (5%)	8.0
Yb1-21	110	h-YbMnO$_3$ (48%), YbOOH (36%), Mn$_3$O$_4$ (10%)	8.9
Yb2-21	130	h-YbMnO$_3$ (75%), YbOOH (18%), Mn$_3$O$_4$ (5%)	7.5
Avg*	150	h-YbMnO$_3$ (76%), YbOOH (18%), Mn$_3$O$_4$ (3%)	7.5-10.7
Yb7-21	240	h-YbMnO$_3$ (86%), Yb$_2$Mn$_2$O$_7$ (7%), YbMn$_2$O$_5$ (4%)	11.7

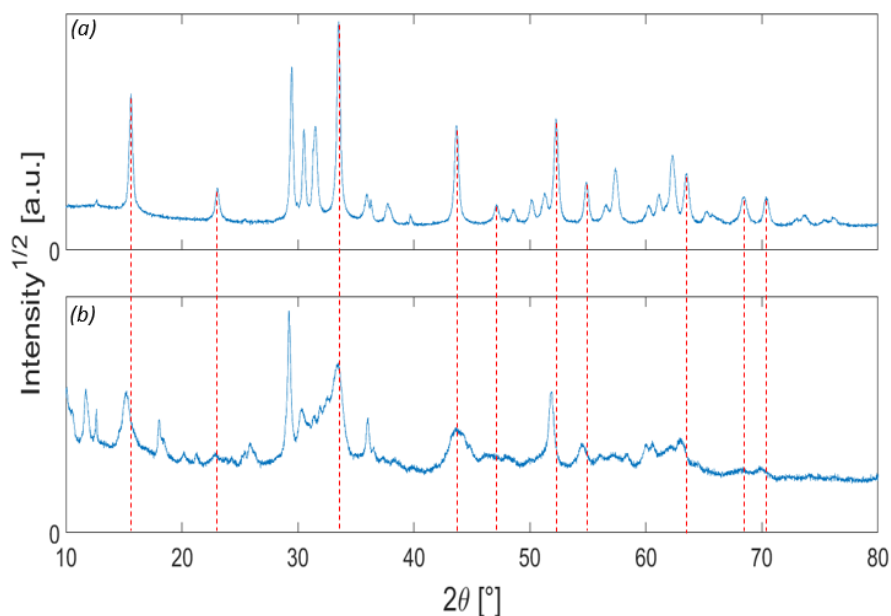*Average percentages of the Yb3-21, Yb4-21, and Yb5-21 syntheses.

Figure 4.2: X-ray diffractograms of a product with relatively high amount of *h*-YbMnO$_3$ (*(a)*, Yb7-21, 86%) and the Yb1-11 product (*b*). Some peaks belonging to *h*-YbMnO$_3$ in *(a)* are highlighted in red and projected onto *(b)* to illustrate the possibility that *h*-YbMnO$_3$ is in the process of forming also in *(b)*. The full Rietveld refinement of the Yb7-21 product can be found in Appendix C, as can the isolated plot of the diffractogram of Yb1-11.

The phase purities are determined from Rietveld refinements, the only exception being the synthesis at 110 °C and with 10.6 M KOH (Yb1-11). As can be seen in the diffractogram in Figure 4.2 *(b)* (also, the diffractogram is plotted alone in Figure C.2), the product appears to consist of a mix of amorphous and crystalline material, which in combination with some unidentified peaks at low angles did not allow for a reliable Rietveld refinement to be carried out. Whether or not *h*-YbMnO$_3$ is present in the product is thus not completely clear. Some peaks belonging to *h*-YbMnO$_3$ in the Yb7-21 product seem to have broader, less intense, and slightly shifted counterparts in the Yb1-11 product, and are indicated in red in Figure 4.2. Thus, there is a possibility that *h*-YbMnO$_3$ is in the process of forming from more amorphous material in the Yb1-11 product. However, some of the peaks belonging to *h*-YbMnO$_3$ in Yb7-21 do not appear to have counterparts in the Yb1-11 product, speaking against presence of *h*-YbMnO$_3$ in the latter. Further, the product from Yb1-11 is dark brown, whereas all products confirmed by XRD to contain a substantial amount of *h*-YbMnO$_3$ are black, indicating that the phase purity of *h*-YbMnO$_3$ from the Yb1-11 synthesis is very low if at all above zero. For simplicity, the value used for the *h*-YbMnO$_3$ content in that synthesis product will be zero, although it cannot be ruled out that a small amount is present or would form from the amorphous material if the synthesis were allowed to run longer.

4.1.2   *The effect of hydroxide concentration*

In addition to the temperature dependence discussed in Section 4.1.1, it is evident from Figure 4.1 and Table 4.1 that syntheses with lower hydroxide concentration yield products with lower h-LnMnO$_3$ content, especially when the temperature is low. This trend is substantiated by a synthesis conducted at 130 °C with only 0.93 M KOH (Yb-0.9). Despite its product being synthesized under otherwise identical reaction conditions to the manganite-yielding Yb2-11 and Yb2-21 products, it does not seem to contain any manganite - its color is brown and its diffractogram (which is plotted in Figure C.1, Appendix C) is more similar to that of the Yb1-11 product (see Section 4.1.1) than to those of products rich in h-YbMnO$_3$.

High hydroxide concentration favoring h-LnMnO$_3$ formation is a trend that is also observed when yttrium is used as the rare-earth element. As can be seen from the phase compositions of the Y-16 and Y2-21 products in Table 4.2, the phase purity of h-YMnO$_3$ is significantly lower when the hydroxide concentration is 15.9 M than when it is 21.2 M. This is in line with what is seen for ytterbium in Table 4.1, where higher hydroxide concentration also results in higher content of h-LnMnO$_3$.

In addition to favoring the formation of h-YMnO$_3$, higher hydroxide concentration seems to result in lower amounts of the Y(OH)$_3$ and YMn$_2$O$_5$ phases, whereas the content of o-YMnO$_3$ is also higher when the hydroxide concentration is high.

The Y-11 synthesis also indicates that high hydroxide concentration favors h-LnMnO$_3$. XRD analysis shows that the Y-11 product does not contain any h-YMnO$_3$, even though the Y-11 product was synthesized at higher temperature than the manganite-yielding Y-16 and Y2-21 syntheses (300 °C), which based on the observations in Section 4.1.1 and in literature [33, 34] is expected to favor h-LnMnO$_3$ formation. Instead, the product seems to consist mainly of YMn$_2$O$_5$ as well as one or more unidentified phases. The X-ray diffractogram and the calculated intensities from the YMn$_2$O$_5$ phase are plotted in Figure C.17. As can be seen, several diffraction lines have not been accounted for, and a reliable phase composition can thus not be given. The unidentified phases may be a result of the Y-11 synthesis being

Table 4.2: Product composition (in wt%) as a function of hydroxide concentration. Apart from hydroxide concentrations, both syntheses were performed under identical conditions. Full compositions are given in Table B.2.

ID	Main phases	Rwp
Y-16	h-YMnO$_3$ (81%), YMn$_2$O$_5$ (13%), Y(OH)$_3$ (3%)	11.5
Y2-21	h-YMnO$_3$ (90%), o-YMnO$_3$ (4%), YMn$_2$O$_5$ (3%)	11.3

performed in a different autoclave than the other syntheses. Since the high-temperature autoclave consists of a Cu-Ni alloy and the solution inside the autoclave was observed to be deep blue after heating (which was not seen for any of the other syntheses), it can be assumed that the permanganate oxidized copper (and possibly also nickel) from the autoclave during heating. Thus, it is possible that the unidentified phases contain Cu^{2+} and/or Ni^{2+}. For the same reason, no further syntheses were carried out using the high-temperature autoclave.

Regions in temperature-pH-space where h-LnMnO$_3$ can be formed are suggested in Figures 4.3 and 4.4, with Yb and Y as the rare-earth element, respectively. All reaction conditions except temperature and hydroxide concentration are similar in all syntheses within each figure. It should be noted that the line between the regions where h-LnMnO$_3$ can and cannot be formed is arbitrarily drawn - the boundary between the regions may be a line with different slope or a curve instead of a line.
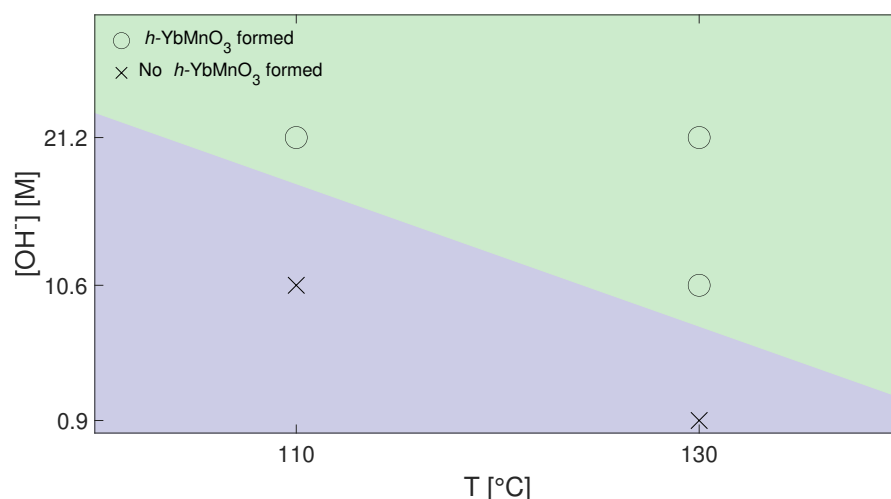
Figure 4.3: Graphical representation of temperatures and hydroxide concentrations that yielded h-YbMnO$_3$ (represented by "o"), as well as both temperature-[OH$^-$] combinations that did not (represented by "x"). The line between the regions where h-YbMnO$_3$ can and cannot be formed is arbitrarily drawn.
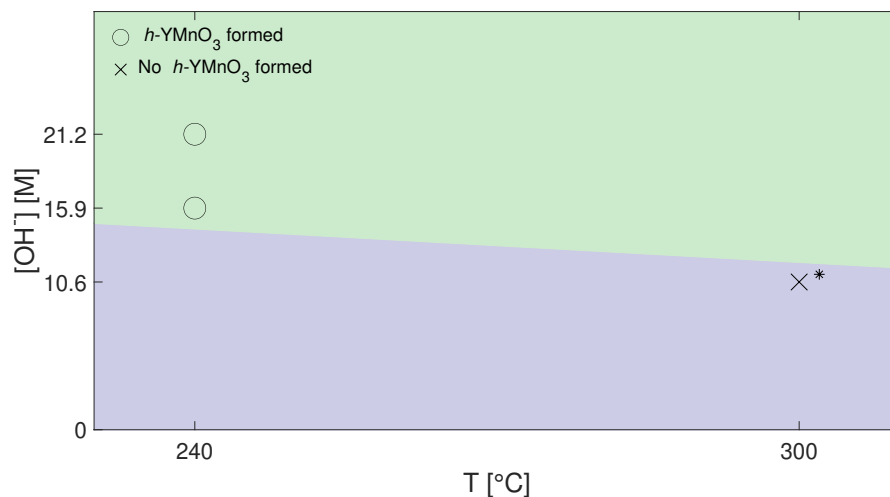
Figure 4.4: Graphical representation of temperatures and hydroxide concentrations that yielded *h*-YMnO$_3$ (represented by "o"), as well as the temperature-[OH$^-$] combinations that did not (represented by "x"). The line between the regions where *h*-YMnO$_3$ can and cannot be formed is arbitrarily drawn.
*Reaction at 300 °C performed in high temperature autoclave, see Section 3.2).

4.1.3   *The effect of reaction time*

With ytterbium as the rare-earth element, two sets of reaction conditions were used to determine the effect of reaction time. One of the sets was synthesized at 130 °C with 10.6 M KOH (Yb2-11 and Yb3-11), the other at 240 °C with 21.2 M KOH (Yb7-21 and Yb8-21). Within each set, one synthesis was allowed to run for 24 h and the other for 72 h. The phase compositions of those four synthesis products can be found in Table 4.3.

While the phase purity of *h*-YbMnO$_3$ is similar after 24 and 72 h at 240 °C and 21.2 M KOH, it increases over time at 130 °C and 10.6 M KOH. Additionally, the YbOOH content declines significantly over time at 130 °C, whereas that phase is not present in either product at 240 °C. At 130 °C, the amount of the Mn^{2+}-containing Mn$_3$O$_4$ phase

Table 4.3: Product composition (in wt%) as a function of reaction time, ytterbium. Hydroxide concentration can be read out of the synthesis ID, and reaction temperature and time are given in the table. Apart from those three parameters, all syntheses were performed under identical conditions. Full compositions are given in Table B.3.

ID	T [°C]	Time [h]	Main phases	Rwp
Yb2-11	130	24	*h*-YbMnO$_3$ (67%), YbOOH (20%), Mn$_3$O$_4$ (11%)	9.4
Yb3-11	130	72	*h*-YbMnO$_3$ (76%), YbOOH (13%), Mn$_3$O$_4$ (5%), YbMn$_2$O$_5$ (2%)	9.0
Yb7-21	240	24	*h*-YbMnO$_3$ (86%), Yb$_2$Mn$_2$O$_7$ (7%), YbMn$_2$O$_5$ (4%), Mn$_3$O$_4$ (3%)	11.7
Yb8-21	240	72	*h*-YbMnO$_3$ (84%), Yb$_2$Mn$_2$O$_7$ (12%), YbMn$_2$O$_5$ (2%), Mn$_3$O$_4$ (2%)	11.4

is also seen to decrease over time. For the syntheses at 240 °C, on the other hand, the largest difference between the 24 and 72 h products may be the increase in the total amount of the Mn^{4+}-containing phases $YbMn_2O_5$ and $Yb_2Mn_2O_7$ after longer reaction time.

With yttrium as the rare-earth element, the effect of reaction time was investigated through one set of reaction conditions with four different reaction times: 6 h (Y1-21), 24 h (Y2-21), 48 h (Y3-21), and 72 h (Y4-21). The phases that display an interesting development as the reaction time is varied are shown in Figure 4.5. In addition to the three phases shown, all four products contain 4% o-$YMnO_3$ as well as small amounts of Mn_3O_4 (the content of the latter declines from 3% to 1% as the reaction time is increased).

While the phase purity of h-$YMnO_3$ is similar after 6 and 72 h, it is higher in the products of the 24 h and 48 h syntheses. At the same time, the $Y(OH)_3$ content is much higher for the product from the 6 h synthesis than for all the other products. Additionally, the amount of the Mn^{4+}-containing YMn_2O_5 phase is seen to increase over time, particularly from 48 to 72 h, whereas the tendency appears to be that the amount of Mn^{2+}-containing Mn_3O_4 decreases over time (not included in Figure 4.5, see Table B.4). Both these observations are in line with the observations of the Mn^{4+} and Mn^{2+} phases in the ytterbium system in Table 4.3. In other words, the lower h-$YMnO_3$ content after 6 h compared to the 24 and 48 h syntheses appears to be primarily due to unreacted yttrium in the form of $Y(OH)_3$, whereas the content of YMn_2O_5 has increased at the expense of h-$YMnO_3$ after 72 h. The phase purities of h-$LnMnO_3$ from Table 4.3 and Figure 4.5 are plotted as a function of time in Figure 4.6.
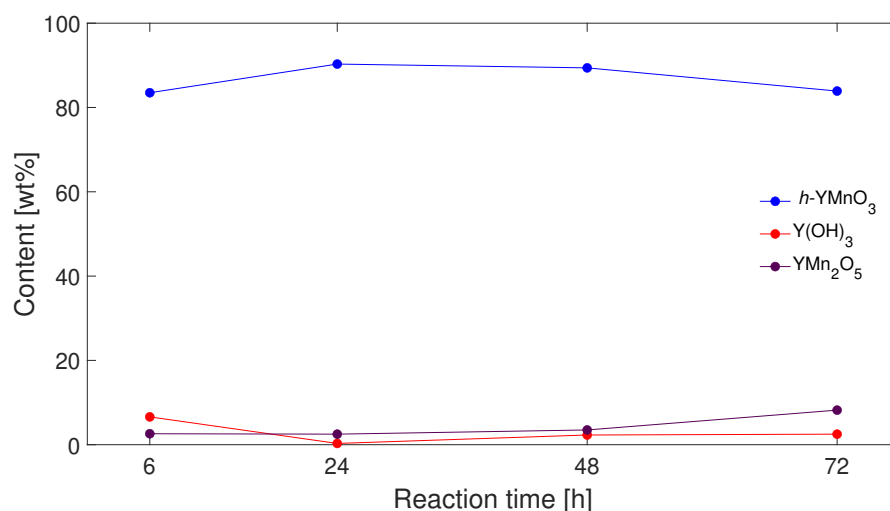

Figure 4.5: Product composition as a function of reaction time, yttrium. Apart from reaction time, all syntheses were performed under identical conditions. Only major phases with an interesting development as the reaction time is varied are shown, the full composition of the products is given in Table B.4.
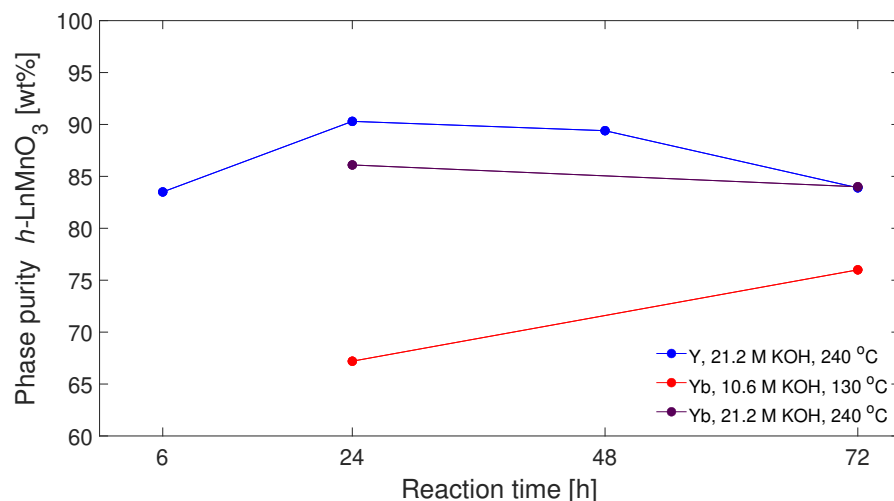
Figure 4.6: Phase purities of h-YbMnO$_3$ as a function of reaction time for three different sets of reaction conditions: Ln=Y, 240 °C, 21.2 M KOH (blue), Ln=Yb, 130 °C, 10.6 M KOH (red), Ln=Yb, 240 °C, 21.2 M KOH (purple). The purities were obtained from Rietveld refinements. Apart from the parameters listed, all reaction parameters are identical for all syntheses.

4.1.4 *The effect of cation concentration*

The difference in phase composition between the Yb7-21 and Yb9-21 products, which were synthesized under identical conditions except cation concentration, can be seen in Table 4.4. Additionally, Yb6-11, which is identical to Yb9-21 except for hydroxide concentration, is included to see if the effects of decreased hydroxide concentration observed in Section 4.1.2 persist when the cation concentration is higher. Only the concentration of Yb^{3+} is given in Table 4.4, as the Yb^{3+}: Mn^{2+}: Mn^{7+} ratio is constant (5:4:1).

The phase purity of h-YbMnO$_3$ is not observed to change much when the ytterbium concentration is increased from 0.17 to 0.31 M. However, the amount of YbOOH appears to be larger in the products synthesized at higher cation concentration, whereas the YbMn$_2$O$_5$ and

Table 4.4: Product composition (in wt%) as a function of cation concentration. Hydroxide concentration can be read out of the synthesis ID, and Yb^{3+} concentration is given in the table. Apart from those two parameters, all syntheses were performed under identical conditions. Full composition is given in Table B.5.

ID	[Yb^{3+}] [M]	Main phases	Rwp
Yb7-21	0.17	h-YbMnO$_3$ (86%), Yb$_2$Mn$_2$O$_7$ (7%), YbMn$_2$O$_5$ (4%)	11.7
Yb9-21	0.31	h-YbMnO$_3$ (86%), YbOOH (6%), Yb$_2$Mn$_2$O$_7$ (4%)	12.0
Yb6-11	0.31	h-YbMnO$_3$ (87%), YbOOH (9%), YbMn$_2$O$_5$ (2%)	10.3

$Yb_2Mn_2O_7$ phases are more prominent when lower cation concentration is used.

The trend of lower h-LnMnO$_3$ phase purity resulting from lower hydroxide concentration described in Section 4.1.2 is not seen at high cation concentration, at least not at temperatures as high as 240 °C. However, the Yb6-11 product has slightly more YbOOH than the Yb9-21 product, which was synthesized under identical conditions apart from hydroxide concentration.

4.1.5 *The effect of precursor type*

Syntheses from salt precursors are compared to otherwise similar syntheses from oxide precursors for three different sets of reaction conditions in Table 4.5. For the first two sets of reaction conditions (Yb, 150 °C, 24 h), oxide precursors are seen to result in much lower h-YbMnO$_3$ content, especially with lower hydroxide concentration. When oxide precursors are used, YbOOH is the most prominent phase in the product for both hydroxide concentrations, with substantial amounts of unreacted Mn$_2$O$_3$ also being present. In comparison, the product compositions from salt and oxide precursors are closer for the last set of reaction conditions (Y, 240 °C, 72 h).

For all three sets of reaction conditions, the Mn^{2+}-containing Mn$_3$O$_4$ phase is more abundant in the products from salt precursors than from oxide precursors, but small amounts of Mn^{2+}-containing Mn$_3$O$_4$ and/or phases containing Mn^{4+} are present even in the products from oxide precursors (see the full composition in Table B.6), where manganese has only been added in the +3 oxidation state (in the form of Mn$_2$O$_3$).

Table 4.5: The phase composition (in wt%) of products synthesized from different precursor types. Precursor type, reaction temperature, and reaction time are listed in the table, whereas Ln element and KOH concentration can be read out of the synthesis ID. All other parameters are identical for all syntheses listed. Full compositions are given in tables B.6 and B.7. See Section 3.2 for a description of the experimental procedure used with each precursor type.

ID	Precursor type	T [°C]	Time [h]	Main phases	Rwp
Yb4-11	Salt	150	24	h-YbMnO$_3$ (75%), YbOOH (18%), Mn$_3$O$_4$ (5%)	8.0
Yb5-11	Oxide	150	24	YbOOH (72%), Mn$_2$O$_3$ (25%), h-YbMnO$_3$ (1%)	13.3
Avg*	Salt	150	24	h-YbMnO$_3$ (76%), YbOOH (18%), Mn$_3$O$_4$ (3%)	7.5-10.7
Yb6-21	Oxide	150	24	YbOOH (49%), h-YbMnO$_3$ (32%), Mn$_2$O$_3$, (18%)	11.1
Y4-21	Salt	240	72	h-YMnO$_3$ (84%), YMn$_2$O$_5$ (8%)	9.4
Y5-21	Oxide	240	72	h-YMnO$_3$ (85%), YMn$_2$O$_5$ (12%)	8.2

*Average percentages of the Yb3-21, Yb4-21, and Yb5-21 syntheses.

4.1.6   *The effect of Ln element*

As can be seen by comparing figures 4.3 and 4.4, it is possible to synthe-
size *h*-YbMnO$_3$ at considerably lower temperature and hydroxide con-
centration than those required to obtain *h*-YMnO$_3$. For instance, the Y-
11 product synthesized at 300 °C does not contain *h*-LnMnO$_3$, whereas
the Yb2-11 product does despite being synthesized at only 130 °C,
other reaction conditions being similar. However, the *h*-LnMnO$_3$ phase
purity does not appear to be lower when Ln=Y than when Ln=Yb
given that the reaction conditions are such that *h*-YMnO$_3$ can form.
Instead, the *h*-LnMnO$_3$ phase purity in Figure 4.6 is observed to be
slightly higher with yttrium than with ytterbium.

Further, there appears to be a significant difference in the content
of the LnOOH and Ln(OH)$_3$ phases. As can be seen in the previous
sections, incompletely reacted yttrium (in the sense that it has not
formed a phase with manganese) seems to primarily be in the form
of Y(OH)$_3$, whereas incompletely reacted ytterbium mainly appears
as YbOOH. Examples are given in Figure 4.7, where diffractogram
subranges of typical products are shown (the full diffractograms are
given in Appendix C). Y(OH)$_3$ is clearly seen in *(a)*, whereas YbOOH
(but no Yb(OH)$_3$) is seen in *(b)*. It should be noted that although this
trend is consistent among the synthesis products where incompletely
reacted yttrium or ytterbium is present, some products neither contain
appreciable amounts of Ln(OH)$_3$ nor LnOOH.

Incompletely reacted Ln^{3+} is not only present as different phases
when yttrium and ytterbium are used, the peak broadening observed
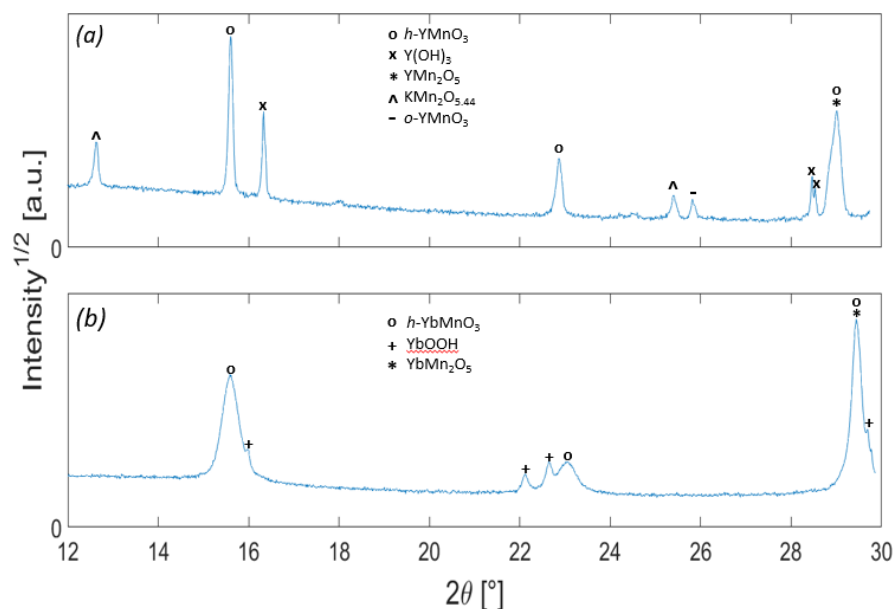
Figure 4.7: Subrange of the X-ray diffractogram from the Y1-21 product *(a)* and
the Yb9-21 product *(b)*, with major peaks indexed. The full diffractograms
are given in figures C.19 and C.16.

in those phases also differs. For YbOOH, the Lorentzian volume weighted mean crystallite size obtained from Rietveld refinement typically is below 100 nm, whereas no broadening (beyond what is caused by instrumental resolution) is observed for $Y(OH)_3$. Peak broadening is also observed for h-YbMnO$_3$ but not for h-YMnO$_3$, as can be seen by examining the peak shapes of h-LnMnO$_3$ in Figure 4.7. However, SEM will be used as the primary tool to assess the size of the h-LnMnO$_3$ particles, see Section 4.3.

A final difference between the diffractograms in Figure 4.7 is the presence of $KMn_2O_{5.44}$ in the Y1-21 product, but not in the Yb9-21 product. However, this is not a consistent trend across the other syntheses, and the amount of $KMn_2O_{5.44}$ is very low (<1 wt%) even in Y1-21 (the peaks of $KMn_2O_{5.44}$ being intense due to preferred orientation rather than high content).

4.1.7 *A remark about uncertainty*

In all refinements carried out except the refinement of the Y-11 synthesis, which was discussed in Section 4.1.2, all major peaks have been identified and refined. However, small shoulders, intensity mismatches, and/or minor unidentified peaks remain in some of the diffractograms and warrant attention in the future. Hence, the true phase compositions may differ slightly from those reported in the previous sections, especially in the refinements with high Rwp values.

Two repeats of one of the syntheses (Yb3-21) were carried out to get an idea of the reproducibility and uncertainty in the phase compositions. The two repeats were made from different batches of precursor solutions (see Section 3.2) to see if any differences from the batch change could be observed, but all three syntheses are otherwise identical. Full phase composition and Rwp values of the three syntheses as obtained from the Rietveld refinements are given in Table B.7.

While the phase composition does differ from synthesis to synthesis, the Yb5-21 synthesis made from a different batch of precursor solutions does not seem to differ more from the two other syntheses than Yb3-21 differs from Yb4-21. The phase purity of h-YbMnO$_3$ is 72, 75, and 80 wt% for Yb3-21, Yb4-21, and Yb5-21, respectively, yielding an average phase purity of 76 wt%. The sample standard deviation is 3.7 percentage points, serving as a measure of the uncertainty and reproducibility of the phase purities that have been reported.

4.2 LATTICE PARAMETERS

The lattice parameters of h-YbMnO$_3$ as obtained from Rietveld refinements are given in Table 4.6. Correspondingly, the lattice parameters of h-YMnO$_3$ are listed in Table 4.7. Literature values for h-LnMnO$_3$ synthesized by high-temperature methods are also included for comparison. For h-YbMnO$_3$, the values reported by Liu et al. [47], who prepared h-YbMnO$_3$ by a flux method at 1200 °C described by Choi et al. [91], are used. For h-YMnO$_3$, the values reported by Katsufuji et al. [46] are used. They prepared their samples by sintering stochiometric amounts of Y$_2$O$_3$ and MnO$_2$ at 1200, 1270, and 1350 °C as described by the same author in [92].

Table 4.6: Lattice parameters of h-YbMnO$_3$ in all products confirmed by XRD to contain that phase. The parameters were obtained from Rietveld refinements. As a reminder, the reaction conditions are also given, except the hydroxide concentration, which can be read from the synthesis ID. Literature value from Liu et al. [47]. The phase purity of h-YbMnO$_3$ is also given.

ID	Precursor type	[Yb^{3+}] [M]	$T_{reaction}$ [°C]	Time [hours]	h-YbMnO$_3$ content [wt%]	a [Å]	c [Å]
Literature						6.0629	11.353
Yb2-11	Salt	0.17	130	24	67	6.100	11.35
Yb3-11	Salt	0.17	130	72	76	6.086	11.35
Yb4-11	Salt	0.17	150	24	75	6.075	11.35
Yb5-11	Oxide	0.17	150	24	1	6.020	11.37
Yb6-11	Salt	0.31	240	24	87	6.065	11.36
Yb1-21	Salt	0.17	110	24	48	6.080	11.36
Yb2-21	Salt	0.17	130	24	75	6.069	11.35
Yb3-21	Salt	0.17	150	24	72	6.068	11.36
Yb4-21*	Salt	0.17	150	24	75	6.066	11.36
Yb5-21*	Salt	0.17	150	24	80	6.071	11.36
Yb6-21	Oxide	0.17	150	24	32	6.107	11.35
Yb7-21	Salt	0.17	240	24	86	6.066	11.36
Yb8-21	Salt	0.17	240	72	84	6.066	11.36
Yb9-21	Salt	0.31	240	24	86	6.065	11.36

*Repeats of Yb3-21

With ytterbium as the rare-earth element, only small variations in the c lattice parameter are observed (apart from the Yb5-11 product, where the h-YbMnO$_3$ content is only 1%). The values are also similar to the literature value. For the a parameter, on the other hand, slightly larger variations are observed. The most prominent trend may be that the a parameters from the hydrothermal syntheses in this study are considerably larger than the value reported by Liu et al. [47]. Also, the products synthesized hydrothermally in this study seem to display slightly larger a when synthesized at lower temperature, especially in the series with 10.6 M KOH. The products synthesized from oxide

Table 4.7: Lattice parameters of *h*-YMnO$_3$ in all products confirmed by XRD to contain that phase. The parameters were obtained from Rietveld refinements. As a reminder, the reaction conditions are also given, except the hydroxide concentration, which can be read from the synthesis ID. Literature value from Katsufuji et al. [46]. The phase purity of *h*-YMnO$_3$ is also given.

ID	Precursor type	[Y^{3+}] [M]	$T_{reaction}$ [°C]	Time [hours]	*h*-YMnO$_3$ content [wt%]	a [Å]	c [Å]
Literature						6.1483	11.443
Y-16	Salt	0.17	240	24	81	6.154	11.39
Y1-21	Salt	0.17	240	6	84	6.164	11.38
Y2-21	Salt	0.17	240	24	90	6.157	11.38
Y3-21	Salt	0.17	240	48	89	6.156	11.38
Y4-21	Salt	0.17	240	72	84	6.156	11.38
Y5-21	Oxide	0.17	240	72	85	6.142	11.40

precursors both display very different *a* from those synthesized from salt precursors, but the effect is inconsistent - oxide precursors seem to result in smaller *a* at 10.6 M KOH and larger *a* at 21.2 M KOH. It should also be noted that the phase purity of *h*-YbMnO$_3$ is very low for those two products (1 and 32 wt%), which may render the value obtained from Rietveld refinements less reliable.

With yttrium as the rare-earth element, larger *a* parameter for the hydrothermally synthesized *h*-YMnO$_3$ in this study compared to the value of *h*-YMnO$_3$ synthesized by solid-state synthesis [46, 92] is also observed. Further, the *c* parameter appears to be considerably smaller for the products in this study than the value reported by Katsufuji et al. [46]. Finally, the Y5-21 product from oxide precursors appears to have smaller *a* and larger *c* than the products from salt precursors.

4.3 MICROSTRUCTURE

SEM analysis shows that the *h*-LnMnO$_3$ formed in this work displays platelet morphology. However, the size and shape of the platelets vary significantly depending on reaction conditions, and will be discussed in the following. Since the microstructure of the *h*-YbMnO$_3$ particles is seen to differ considerably from that of the *h*-YMnO$_3$ particles, they will be discussed separately.

4.3.1 *The microstructure of hexagonal YbMnO$_3$*

Small, dense platelets are the predominant morphology of *h*-YbMnO$_3$ in all synthesis products. Examples can be seen in Figure 4.8, where SEM images of particles synthesized at different temperature and hydroxide concentration, but otherwise under identical conditions, are shown.

	10.6 M KOH	21.2 M KOH

110 °C   No data

(a)

130 °C

(b)

(c)

150 °C

(d)

(e)

240 °C   No data

(f)
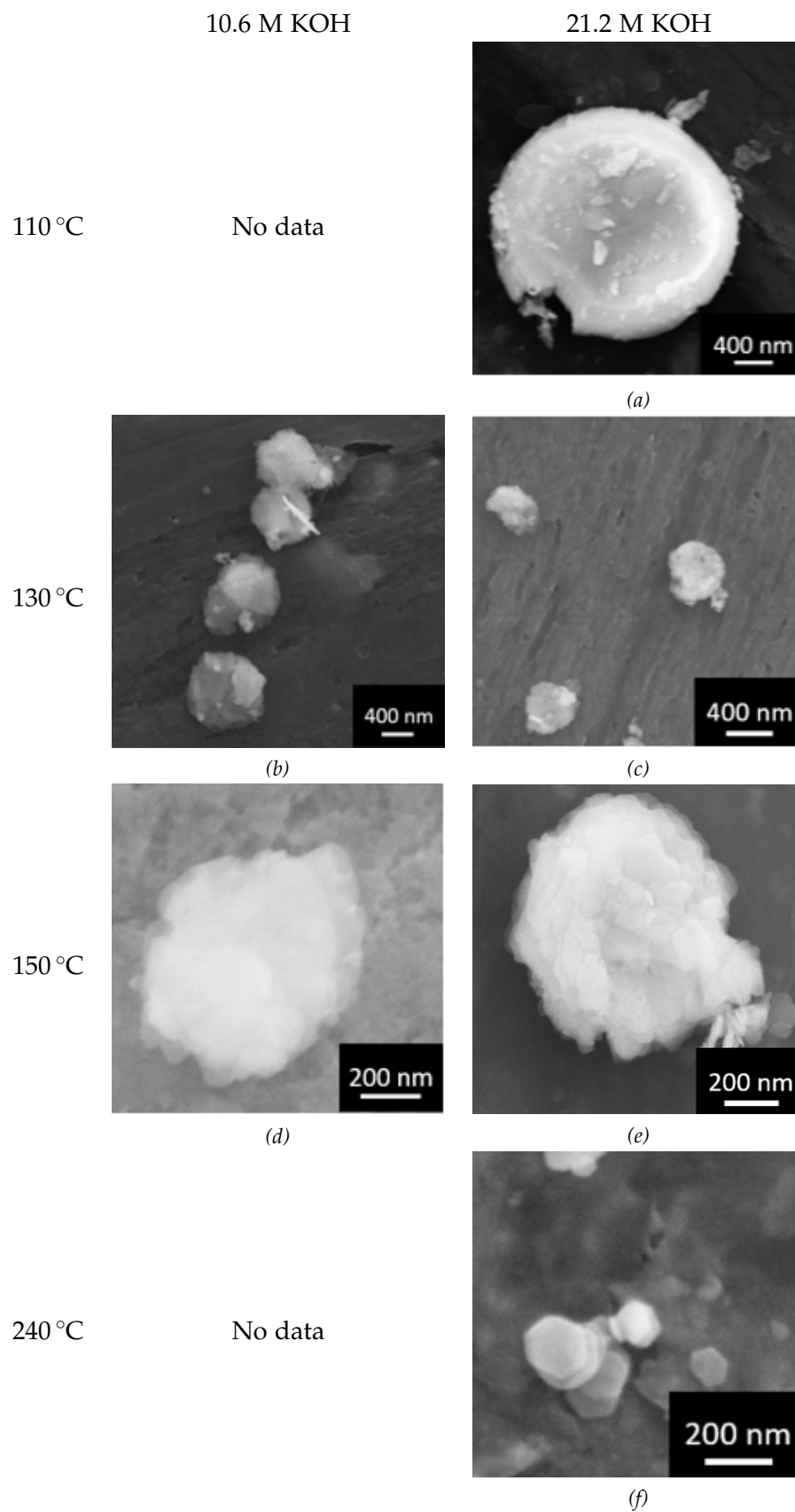
Figure 4.8: Comparison of representative *h*-YbMnO$_3$ particles from 24 h syntheses with different temperature and hydroxide concentration. Those two parameters are given in the figure, the reaction conditions are otherwise identical.
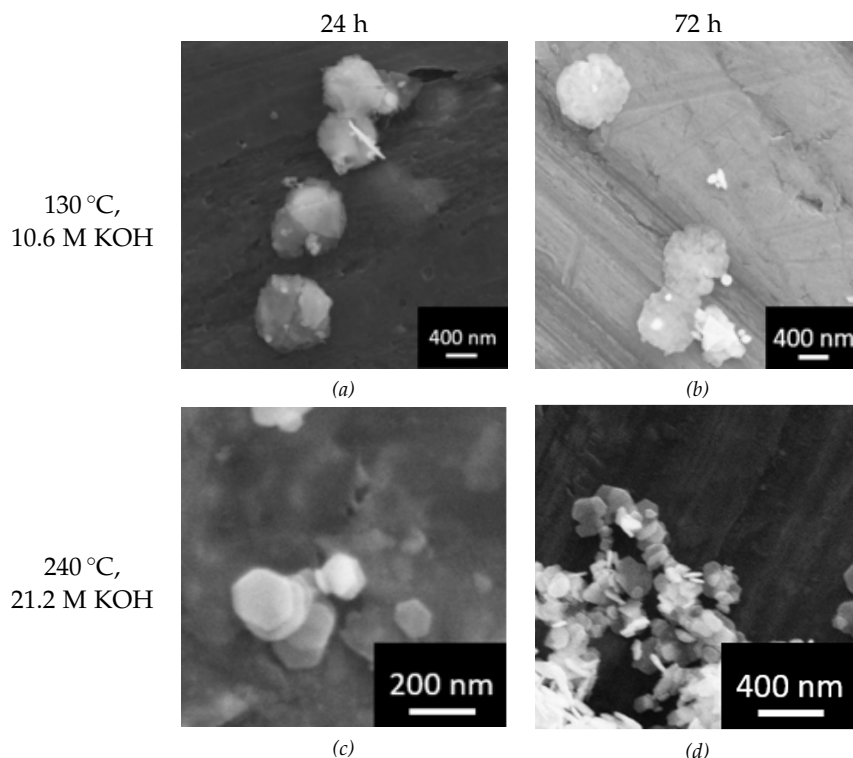
Figure 4.9: The effect of reaction time on h-YbMnO$_3$ microstructure for two different sets of reaction conditions. Reaction conditions which are not specified in the figure are identical for all four syntheses.

With the exception of the Yb1-21 product depicted in Figure 4.8a, the platelets have a diameter around 1 μm or below. Most particles also have a rough, almost flower-like morphology. Further, the trend appears to be that the particle size decreases as the temperature increases, although it is hard to be certain as the particles display a relatively broad size distribution. The two different hydroxide concentrations used do not appear to result in significantly different particle size.

Two sets of reaction conditions were used for both a 24 h synthesis and a 72 h synthesis. The microstructure of the products are shown in Figure 4.9. No significant difference is observed from different reaction times within each set of reaction conditions.

The products from the Yb6-11 and Yb9-21 syntheses, which were performed with higher cation concentration than the other syntheses, are shown in Figure 4.10. The Yb7-21 product is also shown for comparison, as it was synthesized under identical conditions as the Yb9-21 product apart from cation concentration. Whereas the products synthesized with 21.2 M KOH do not appear to differ much despite different cation concentrations, the product synthesized with 0.31 M Yb^{3+} and 10.6 M KOH (see Figure 4.10b) seems to consist of somewhat larger particles than the product with similar cation concentration, but higher hydroxide concentration (Figure 4.10c). Interestingly, this effect is not seen at lower cation concentration; the different hydroxide

	10.6 M KOH	21.2 M KOH
0.17 M Yb^{3+}	No data	
0.31 M Yb^{3+}		
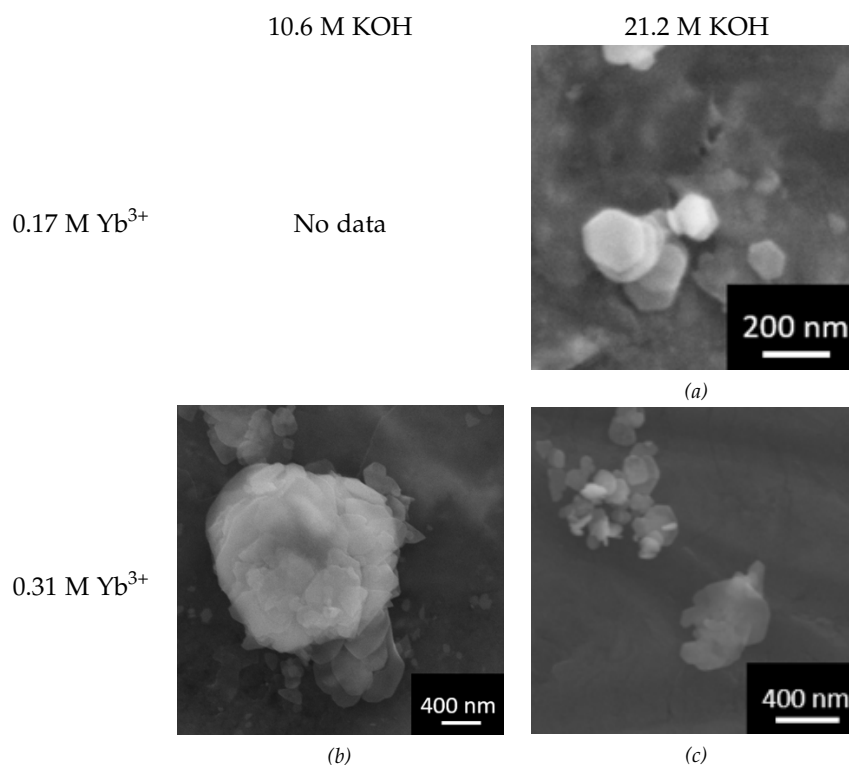
Figure 4.10: SEM images of h-YbMnO$_3$ from the products synthesized at higher cation concentration, as well as from the Yb7-21 product for comparison. Reaction conditions which are not specified in the figure are identical for all three syntheses. 240 °C, 24 h.

concentration does not seem to significantly affect the particle size in Figure 4.8.

While the parameters discussed so far are seen to have either no or only a slight effect on the product microstructure, considerable difference is observed when the precursor type is varied. Particles synthesized from different precursor types but otherwise under similar conditions are seen in Figure 4.11. The particles from oxide precursors (Figure 4.11a) are significantly larger than those from salt precursors (Figure 4.11b), and also seem to have a smoother surface.

Salt precursors   Oxide precursors

(a)   *(b)*
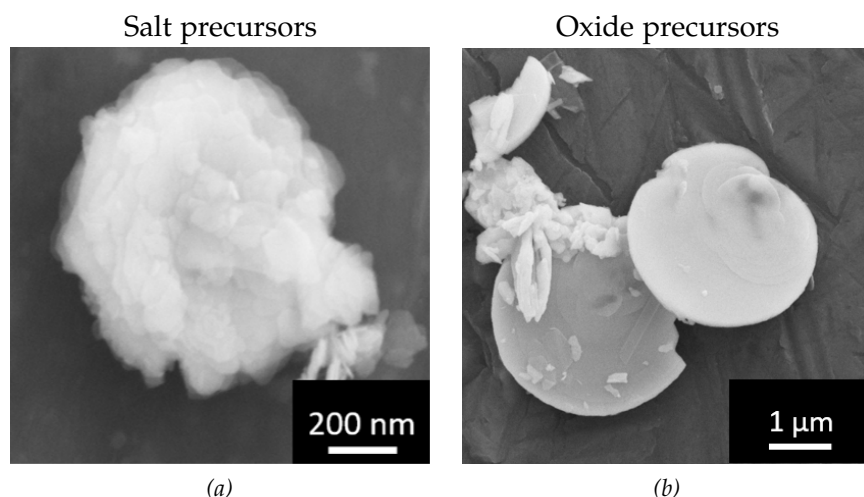
Figure 4.11: The effect of precursor type on h-YbMnO$_3$ microstructure. Reaction conditions are similar apart from the precursor type. 150 °C, 21.2 M KOH, 24 h.

4.3.2 *The microstructure of hexagonal YMnO$_3$*

Morphology of h-YMnO$_3$ as a function of reaction time for the Y1-21 - Y4-21 products is presented in Figure 4.12. Apart from the reaction time, the four syntheses were performed under identical conditions.

After 6 h of heating, only dense particles are observed (figures 4.12a and 4.12b). Most particles are also dense after 24 h (Figure 4.12c), but some particles have a hole or at least an interior that appears to have started dissolving. An example can be seen in Figure 4.12d. After 48 hours, however, several particles where the interior has started dissolving (Figure 4.12e) as well as completely hollow platelets with donut-like morphology (Figure 4.12f) are seen, although some dense platelets also remain. In the Y4-21 product (from 72 h heating), most particles have a completely formed hole and display the donut morphology exemplified in Figure 4.12h. Figure 4.12g shows an almost dense particle with only a very small hole, whereas the donut morphology seen in 4.12h is the predominant one.

Particles with a clear hexagon shape appear to be hollow less frequently (or have a smaller hole such as in Figure 4.12g) than the possibly polycrystalline particles without distinct hexagon shape (seen for instance in Figure 4.12e and 4.12h).

6 h

(a)

(b)

24 h

(c)

(d)

48 h

(e)

(f)

72 h

(g)

(h)
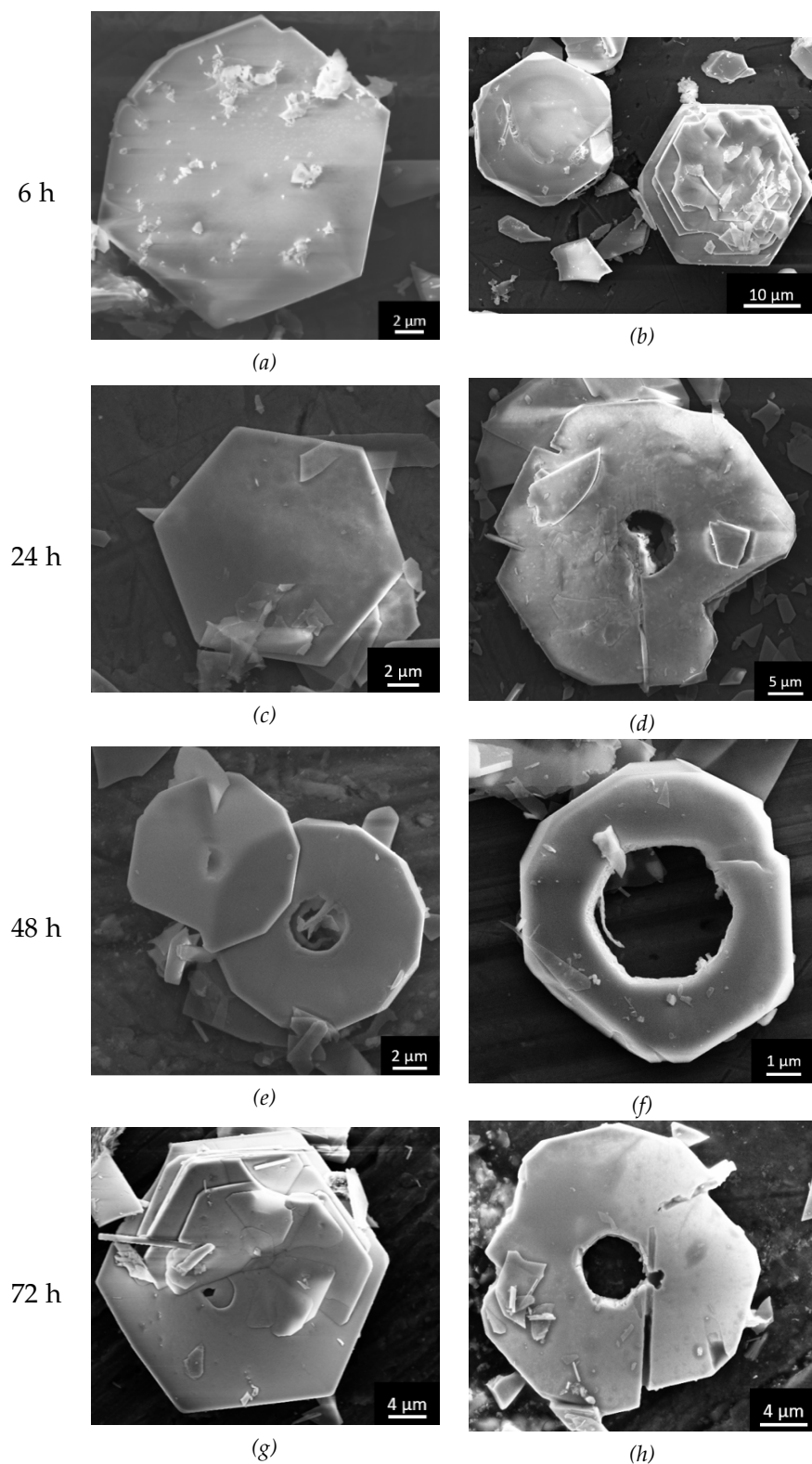
Figure 4.12: Comparison of representative particles from the Y1-21 - Y4-21 syntheses, all synthesized under identical reaction conditions (240 °C, 21.2 M KOH), but with varying reaction time. The reaction time is given in the figure.

The particle and hole diameter of 21-40 particles for each product have been measured in an attempt to understand the growth of the hollow structures. The measured particle sizes are presented in Figure 4.13, where each data point as well as the average size after each reaction time are plotted. No clear trend in the reaction time's impact on the particle diameter is observed. The average particle diameters after 6, 24, 48, and 72 hours are 19 µm, 34 µm, 17 µm, and 29 µm, respectively. It should be noted that the uncertainty in the measured sizes is considerable with a sample size that small and a broad size distribution.
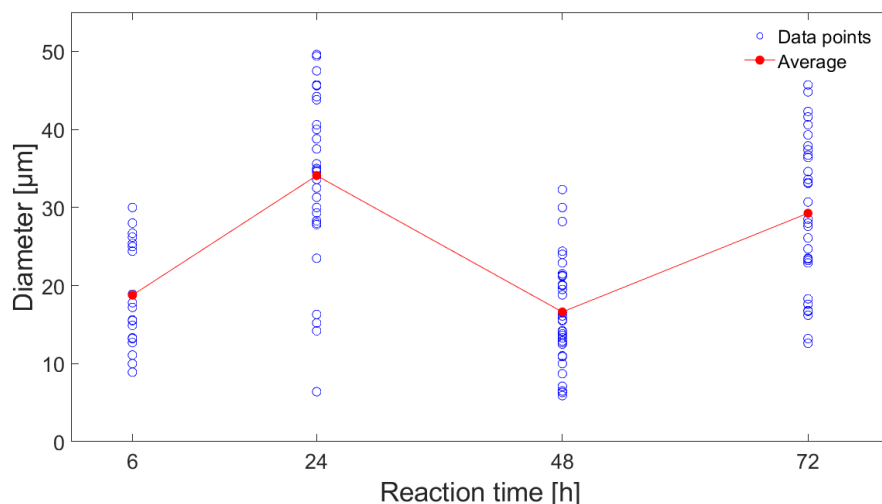
Figure 4.13: Size distribution of *h*-YMnO₃ particles from the Y1-21 - Y4-21 syntheses. Data points are plotted as blue circles, the average diameter for each product is plotted as a filled red circle. The syntheses were performed under identical conditions except reaction time. Sample sizes of 21, 29, 40, and 31 particles were used for the 6 h, 24 h, 48 h, and 72 h reactions, respectively.

The average hole diameter, on the other hand, displays a clearer trend, which can be seen in Figure 4.14. From being zero after 6 hours, the average hole diameter increases when the reaction time is increased to 24 and especially 48 hours, before stabilizing slightly above 3 µm. It should be noted that all particles measured, including the completely dense ones, are included in the computation of the average hole diameter. Thus, the average hole size for the particles that are actually hollow will be larger than the values plotted in Figure 4.14. It should further be noted that that although the average hole diameter does not change much from 48 h to 72 h when particles that are becoming hollow are counted, the number of particles where a hole has been completely formed substantially increases from 48 h to 72 h.
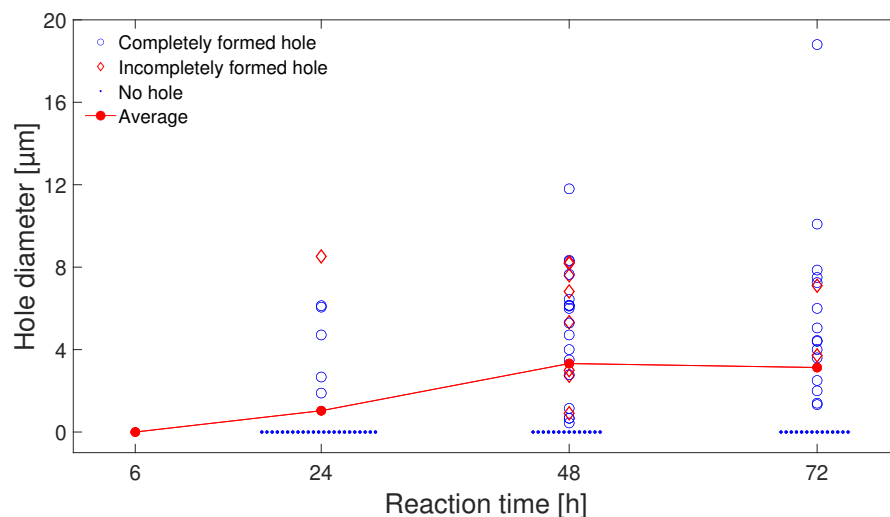
Figure 4.14: Hole diameter as a function of reaction time for the Y1-21 - Y4-21 products. The particles used in the size measurement in Figure 4.13 were also used to obtain data on hole diameter (i.e., the sample sizes are 21, 29, 40, and 31 for the 6 h, 24 h, 48 h, and 72 h reactions, respectively). Particles without hole are spread along the time axis only for visibility. For the 6 h synthesis, only the average is shown as the data points are all zero (i.e., all particles are dense).

To further elucidate the formation mechanism of the donut morphology, EDXS spot analysis was carried out on particles from the Y1-21 product in order to determine if the stochiometric composition changed throughout each particle. A particle from which five different spectra was obtained, each at a different spot, is seen in Figure 4.15. An example of the yttrium to manganese ratio obtained from the spot analysis is plotted in Figure 4.16. It is close to 1 (which is the Y/Mn ratio in h-YMnO$_3$) across the entire particle, a trend that is consistent for all particles on which EDXS was performed. For the particle shown in Figure 4.15, the Y/Mn ratio is highest near the core and lowest near the edges. However, higher yttrium content near the core does not seem to be a consistent trend exhibited by all particles analyzed. The main conclusion drawn from the EDXS analysis thus is that the dense particles after 6 h heating consist of a single phase all the way through, namely h-YMnO$_3$.
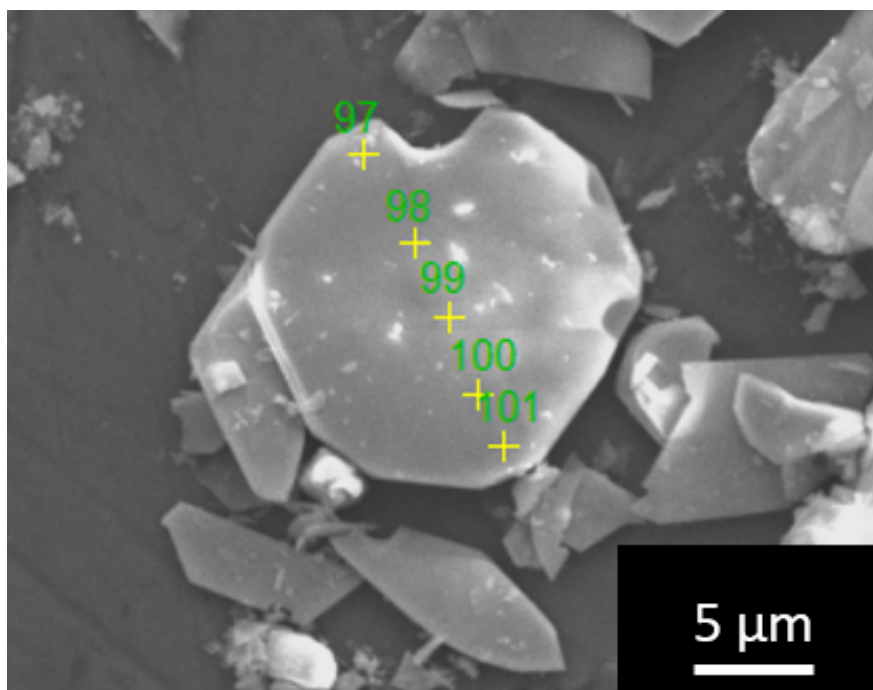
Figure 4.15: One of the *h*-YMnO$_3$ particles on which EDXS was performed. One spectrum was obtained from each of the spots marked with a green number and a yellow cross, and each spectrum was used to calculate the elemental composition (see Section 3.3.3 for details).
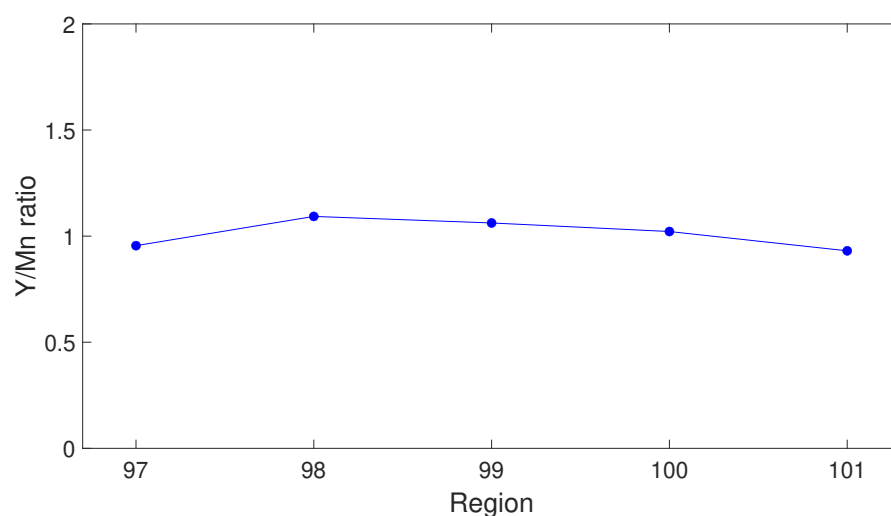
Figure 4.16: Stochiometric yttrium to manganese ratio at different spots on the particle depicted in Figure 4.15 (from the Y1-21 product). The entries on the x-axis correspond to the spots indicated in Figure 4.15.

SEM images of the Y5-21 product are given in Figure 4.17. The product was synthesized from oxide precursors, but otherwise under conditions identical to the Y4-21 synthesis. Both dense (Figure 4.17a) and hollow (Figure 4.17b) particles are present in the product. In many

(a)   *(b)*
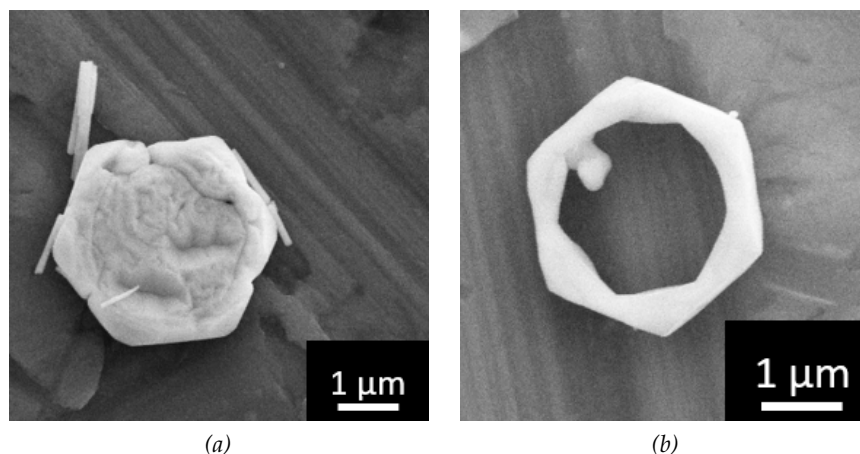
Figure 4.17: SEM images of *h*-YMnO$_3$ from Y5-21, synthesized from oxide precursors, but otherwise under the same conditions as the Y4-21 product seen in subfigures 4.12g and 4.12h; 240 °C, 21.2 M KOH, 72 h.

of the dense particles, however, the interior appears to have started dissolving, as can be seen in Figure 4.17a.

When compared to the Y4-21 product synthesized from salt precursors (see figures 4.12g and 4.12h), the Y5-21 product consists of significantly smaller particles, with a typical diameter of about 3 µm. Interestingly, this is the exact opposite of what was observed with ytterbium as the rare-earth element, where oxide precursors resulted in considerably *larger* particles (see Figure 4.11).

The product from the Y-16 synthesis mostly consists of fragments of *h*-YMnO$_3$ platelets. Since the particles are broken, presumably from the grinding step between synthesis and characterization (see Section 3.2), their size and exact morphology (including whether hollow particles are present) could not be determined. An example of the broken particles is given in Figure A.3 in Appendix A.

4.4   OBSERVATIONS DURING SYNTHESIS

During mixing of the salt precursors, two interesting observations were made by visual inspection. First, adding KOH to a mixture of Ln(NO$_3$)$_3$ and KMnO$_4$ resulted in the formation of a precipitate. Second, brown color was observed upon adding pink MnCl$_2$ solution to a purple reaction mixture containing KMnO$_4$, Ln(NO$_3$)$_3$, and KOH.

When oxide precursors were used, they did not dissolve prior to autoclave heating.

DISCUSSION

In this chapter, interesting observations from Chapter 4 will be discussed, organized by the different reaction parameters' effect. The key observations will then be summarized and tied together in a proposed reaction mechanism.

5.1 REACTION PARAMETERS AND THEIR EFFECT

5.1.1 *The effect of temperature*

The increase in h-YbMnO$_3$ content when the temperature is increased along with the decrease in YbOOH content suggests that the LnOOH phase is an intermediate in the reaction towards h-LnMnO$_3$ formation, as has been suggested earlier [33, 34], including in the author's specialzation project [84]. Higher temperature could favor the reaction between LnOOH and manganese species towards h-LnMnO$_3$ directly, or possibly indirectly by favoring the *formation* of LnOOH, thus giving the LnOOH phase more time to react with manganese. Since a precipitate is formed when KOH is added to Ln(NO$_3$)$_3$ (see Section 4.4), Ln(OH)$_3$ is likely present in the early stages of the reaction, and dehydration of Ln(OH)$_3$ into LnOOH is reported to be favored by increased temperature [33, 34, 82]. However, since products from syntheses with ytterbium at 150 °C or below contain significant amounts of YbOOH, but no Yb(OH)$_3$ (see Table 4.1), the transition from Yb(OH)$_3$ to YbOOH may be fast compared to the reaction between YbOOH and manganese species to form h-YbMnO$_3$. It is thus proposed that higher temperature primarily favors h-YbMnO$_3$ formation by facilitating the reaction between YbOOH and manganese species.

The decline in Mn$_3$O$_4$ content at higher temperature can be seen in context with the increased amount of h-YbMnO$_3$ and decreased amount of YbOOH. If high temperature favors the reaction between manganese and YbOOH, more manganese should be consumed when h-YbMnO$_3$ is formed from YbOOH, providing an explanation of the lower amount of Mn$_3$O$_4$ at higher temperature which is also in line with the explanation of higher h-YbMnO$_3$ amount and lower YbOOH amount.

The Mn^{4+}-containing YbMn$_2$O$_5$ and Yb$_2$Mn$_2$O$_7$ phases are only seen in appreciable amounts at higher temperature, which could be due to disproportion of Mn^{3+} (which is the initial average oxidation state of manganese) into Mn^{2+} and Mn^{4+}. However, since the Mn^{2+}-containing Mn$_3$O$_4$ phase is *less* abundant at higher temperature, an increase in the

average oxidation number of manganese may be more likely. Since the autoclaves are prepared under atmospheric conditions, air is present during the reactions, and dissolved O_2 might oxidize Mn^{3+} into Mn^{4+}. Nevertheless, disproportion of Mn^{3+} into Mn^{2+} and Mn^{4+} cannot be ruled out, as Mn^{2+} could be present in the solution and thus lost in the filtration step instead of reacting to Mn_3O_4, in which case it would not be seen in the XRD diffractograms.

When salt precursors are used, higher temperature also seems to result in smaller particle size (see Figure 4.8). Faster nucleation is a possible explanation because it would lead to more nuclei forming and thus faster consumption of growth species in the growth phase, resulting in many small particles rather than fewer and larger particles. This was proposed as an explanation of similar observations in the author's specialization project [84]. However, this hypothesis has a weakness - since the reaction towards h-LnMnO$_3$ presumably proceeds via solid $Ln(OH)_3$ and LnOOH, and $Ln(OH)_3$ is seen as a precipitate before heating, the nucleation should start already at room temperature and thus not depend strongly on the reaction temperature. Thus, less *time* for growth might be a more feasible explanation for smaller particle size than faster nucleation. Since the $Ln(OH)_3$ phase can grow simply by incorporating Ln^{3+} and OH^- ions from the solution and the LnOOH phase cannot (as that would require $Ln(OH)_3$ to form and then dehydrate), it is assumed that primary growth of the particles that will eventually form h-LnMnO$_3$ mostly occurs while they are in the $Ln(OH)_3$ phase. If so, smaller particle size at higher temperature can be explained by higher temperature favoring the dehydration of $Ln(OH)_3$ into LnOOH, thus decreasing the time the $Ln(OH)_3$ particles have to grow before transitioning into the LnOOH phase that does not grow as easily.

5.1.2   *The effect of hydroxide concentration*

High hydroxide concentration is also seen to favor h-LnMnO$_3$ formation. Based on the observation that the Y-16 product contains more $Y(OH)_3$ than the Y2-21 product, which was synthesized under identical conditions apart from hydroxide concentration (see Table 4.2), high hydroxide concentration could favor h-LnMnO$_3$ formation by facilitating dehydration from $Ln(OH)_3$ to LnOOH. This is in line with Marshall et al. [33], who also reported that the dehydration reaction from $Y(OH)_3$ to YOOH is favored by high hydroxide concentration. If, for a given temperature, the hydroxide concentration is so low that the dehydration is non-spontaneous, it may be impossible to form h-LnMnO$_3$. The syntheses shown in figures 4.3 and 4.4 that did not yield any h-LnMnO$_3$ may be examples of temperature and hydroxide concentration both being too low for the dehydration to LnOOH to be spontaneous.

For the reactions with ytterbium, high hydroxide concentration is also seen to favor h-LnMnO$_3$ formation (see Figure 4.1), even though no Yb(OH)$_3$ is seen in any of the products. Hence, it is possible that hydroxide does not only favor the dehydration from Ln(OH)$_3$ to LnOOH, but also the reaction from LnOOH to h-LnMnO$_3$.

The different hydroxide concentrations used in this study do not appear to result in significantly different microstructure of the products, neither with respect to particle size nor morphology (see Figure 4.8). In the author's specialization project, on the other hand, higher hydroxide concentration was seen to result in significantly smaller particles [84]. However, lower hydroxide concentrations were used than in this study, so it could be that higher hydroxide concentration leads to smaller particles up to a certain point where it is so high that it does not affect the particle size anymore. Interestingly, when the Yb6-11 and Yb9-21 syntheses with 0.31 M Yb^{3+} are compared, the particles synthesized with 10.6 M KOH may be slightly larger than those synthesized with 21.2 M KOH (see Figure 4.10). As the [OH$^-$]/[Yb^{3+}] ratio is lower for these syntheses with higher cation concentration, this observation substantiates the hypothesis that higher hydroxide concentration leads to smaller particles only up to a certain point.

5.1.3 *The effect of reaction time*

At 130 °C and 10.6 M KOH, the increase in h-YbMnO$_3$ content and decrease in YbOOH and Mn$_3$O$_4$ content over time indicate that the reaction between YbOOH and manganese species to form h-YbMnO$_3$ is slow compared to when the temperature and hydroxide concentration are higher, as a similar increase in h-YbMnO$_3$ content over time is not observed at 240 °C and 21.2 M KOH (see Section 4.1.3). This is in line with the discussion in sections 5.1.1 and 5.1.2.

At 240 °C and 21.2 M KOH, on the other hand, the phase purity of h-LnMnO$_3$ is not seen to change much as the reaction time is changed for either rare-earth element. However, the change in the other phases in the products is instructive for understanding how the reaction proceeds. Notably, the content of incompletely reacted rare-earth element (YbOOH in the case of ytterbium and Y(OH)$_3$ in the case of yttrium) is seen to decrease over time. The LnMn$_2$O$_5$ and Ln$_2$Mn$_2$O$_7$ phases, on the other hand, are more abundant after longer reaction time. Since both changes are observed while the h-LnMnO$_3$ content remains largely unchanged, it is possible that h-LnMnO$_3$ is converted to LnMn$_2$O$_5$ (or Ln$_2$Mn$_2$O$_7$), and that more h-LnMnO$_3$ is parallelly formed from the LnOOH phase (or from Y(OH)$_3$ via YOOH when Ln=Y). LnMn$_2$O$_5$ is the thermodynamically most stable phase in the low temperature range used in syntheses in this study [50, 51], but it requires oxidation of Mn^{3+} (the initial average oxidation state) to Mn^{4+}. Thus, while increased reaction time may aid the incompletely

reacted $Ln(OH)_3$ and LnOOH phases in reacting towards h-LnMnO$_3$, it may also increase the extent to which the thermodynamically favored LnMn$_2$O$_5$ is formed at the expense of h-LnMnO$_3$ since more Mn^{3+} can be oxidized to Mn^{4+} when the reaction time is long.

While reaction time is not seen to significantly impact the product microstructure with ytterbium as the rare-earth element (see Figure 4.9), it certainly does when yttrium is used (see Figure 4.12). Hollow particles are the predominant morphology after 48 and 72 h, whereas all particles are dense after 6 h. As was discussed in Section 2.3.3, hollow particles can form in several ways. However, the EDXS analysis performed on the Y1-21 product provides insight that may rule out some of the possibilities. For instance, the EDXS analysis would have revealed it if the core of the particles from the 6 h synthesis consisted of a different phase than the exterior. Since the particles have a constant Y/Mn ratio all the way through, the mechanism with a different and dissolving phase at the core that was proposed by Budhysutanto et al. [70] is considered an unlikely explanation of the hollow particles seen in this study. Similarly, the Kirkendall effect seems unlikely when the particles consist of a single phase (as the diffusibility should then be similar throughout the whole particle so that no net flux of mass from the core is expected). Since the particles are initially dense and then turn hollow, oriented attachment of primary nanoparticles into hierarchical hollow structures as reported by Wannapop et al. [65] is also considered unlikely. The inside-out Ostwald ripening mechanism, which has been seen for several other oxide materials [66–68], on the other hand, does not appear to contradict any of the observations made, and is thus proposed as the mechanism for formation of hollow particles in this study. This hypothesis is also in line with particles with distinct hexagon shape appearing to be hollow less frequently than possibly polycrystalline particles without distinct hexagon shape, as polycrystalline particles may be more prone to dissolving than single-crystals due to higher energy at grain boundaries and thus lower energy cost of dissolution.

While Ostwald ripening normally involves the dissolved material redepositing on a larger particle of the same phase, it cannot be ruled out that the dissolved material from the particle cores is involved in forming the YMn$_2$O$_5$ phase that becomes more abundant when the reaction time is long.

As hollow particles have larger surface area per mass than dense particles of the same size, the hollow particles formed in this study may be well suited for catalysis, which is a possible application of ferroelectric materials (see Section 2.1).

5.1.4 *The effect of precursor type*

Precursor type does not appear to affect the product composition much when yttrium is the rare-earth element, but considerable differences between products synthesized from salt and oxide precursors with ytterbium as the rare-earth element (see Table 4.5). While h-YbMnO$_3$ is the main product from salt precursors, YbOOH is the most abundant phase in the products from oxide precursors, indicating that the reaction between YbOOH and manganese to form h-YbMnO$_3$ is to a large extent incomplete in those syntheses. Indeed, significant amounts of the precursor Mn$_2$O$_3$ is seen in both products from oxide precursors, especially in the product synthesized with lower hydroxide concentration. The presence of Mn$_2$O$_3$ in the products suggests that the lack of h-YbMnO$_3$ is due to incomplete dissolution of Mn$_2$O$_3$, and the greater amount of Mn$_2$O$_3$ when the hydroxide concentration is low is in line with observations made by Stampler et al. [34], who noticed that high pH promotes dissolution of Mn$_2$O$_3$, presumably due to formation of the soluble Mn(OH)$_4^-$ complex. Stampler et al. also proposed that Ln$_2$O$_3$ precursors first react with water to form Ln(OH)$_3$ and then dehydrate to LnOOH. Since YbOOH is seen in large amounts in the products from oxide precursors in this study, but very little Yb$_2$O$_3$ and Yb(OH)$_3$ is seen, the reactions the Yb$_2$O$_3$ precursor undergoes appear to have completed, so that lacking dissolution of the manganese precursor is the primary factor limiting h-YbMnO$_3$ formation.

It should be noted that while the difference in phase composition between products synthesized from salt and oxide precursors are negligible in syntheses with yttrium, the reaction temperature was considerably higher for the syntheses with yttrium (240 °C instead of 150 °C, see Table 4.5). Thus, the impact of precursor type on phase composition in the syntheses with ytterbium, but not in those with yttrium is not necessarily due to differences in the rare-earth metals' properties, but could very well simply be due to Mn$_2$O$_3$ dissolving more easily at higher temperature.

h-LnMnO$_3$ products from salt precursors are seen to be much smaller than products from oxide precursors when ytterbium is used as the rare-earth element, whereas it is the other way around for yttrium (see figures 4.11, 4.12, and 4.17). A possible reason for the precursor type's effect on particle size is the reaction from oxide precursors proceeding only through solid phases towards h-LnMnO$_3$ such as Stampler et al. proposed [34]. If the reaction from Ln$_2$O$_3$ to h-LnMnO$_3$ is a chain of in situ transformations, the size of the Ln$_2$O$_3$ precursors is expected to affect the size of the h-LnMnO$_3$ products (see Section 2.4.2). While such a mechanism may explain why precursor type *affects* the product size, it does not explain why salt precursors result in *smaller* particles than oxide precursors when ytterbium is used and *larger* particles when

yttrium is used. This difference is one of the topics to be discussed in Section 5.1.5.

5.1.5 *The effect of Ln element*

One of the most noticeable differences between the yttrium and ytterbium systems may be that incompletely reacted rare-earth element occurs as different phases for the two elements – almost exclusively as YbOOH for ytterbium and as $Y(OH)_3$ for yttrium. A possible interpretation is that the dehydration from $Ln(OH)_3$ to LnOOH is the rate limiting step when Ln=Y, whereas it is the reaction between LnOOH and manganese species towards h-LnMnO$_3$ when Ln=Yb. This is in line with $Y(OH)_3$ being reported to be more persistent than $Yb(OH)_3$ [82], which is also expected based on the elements' ionic radii (see Section 2.4.3). Interestingly, the different phases incompletely reacted rare-earth element occurs in can be seen in context with SEM imaging, which reveals that the h-YMnO$_3$ particles formed are much larger than the h-YbMnO$_3$ particles when salt precursors are used. Along the lines of the discussion in section 5.1.1, faster dehydration may result in less time for growth of the $Ln(OH)_3$ particles and in turn smaller h-LnMnO$_3$ particles. This hypothesis is substantiated by XRD peak broadening being observed in the YbOOH phase when ytterbium is used, but not in the $Y(OH)_3$ phase when yttrium is used, indicating that the intermediate $Yb(OH)_3$ phase dehydrates to YbOOH when the $Yb(OH)_3$ particles are smaller than the size the $Y(OH)_3$ particles reach. It should further be noted that while both $Y(OH)_3$ and $Yb(OH)_3$ have low solubility in water, $Yb(OH)_3$ is slightly more soluble than $Y(OH)_3$ [93]. Hence, an alternative explanation of the smaller particle size of when ytterbium is used could be that the driving force for growth of $Ln(OH)_3$ ceases earlier when Ln=Yb due to higher solubility and thus lower supersaturation.

As a final major difference between the yttrium and ytterbium systems, the hollow particles resulting when yttrium is used but not when ytterbium is used should be discussed. Once again, it might be instructive to consider the XRD and SEM results in context. Since no product synthesized with yttrium contains any YOOH but unreacted YbOOH is seen in several products from syntheses with ytterbium, the reaction between LnOOH and manganese to form h-LnMnO$_3$ may be faster when Ln=Y than when Ln=Yb (not to be confused with the dehydration from $Ln(OH)_3$ to LnOOH, which is suggested to be faster for Ln=Yb). If the reaction to form h-YMnO$_3$ is faster when yttrium is used, the manganese may have less time to diffuse to the energetically most favorable sites before incorporating, resulting in a slightly less crystalline interior of the h-YMnO$_3$ particles than of the h-YbMnO$_3$ particles. Since less crystalline particle core has been proposed as a driving force for inside-out Ostwald ripening [66] (presumably

because lower degree of crystallinity leads to higher energy, so that the energy cost of the interior dissolving is small), the possibly faster reaction from YOOH to h-YMnO$_3$ indicated by XRD may explain why the h-YMnO$_3$ particles turn hollow, but the h-YbMnO$_3$ particles do not.

5.2 LATTICE PARAMETERS

While the reaction parameters' effect on the lattice parameters of h-LnMnO$_3$ is somewhat inconsistent in this study, the a parameter generally appears to be larger than the values reported from high-temperature synthesis methods both when ytterbium and yttrium is used (see tables 4.6 and 4.7). The reason for this may be ions diffusing in and occupying interstitial positions in the lattice structure when a hydrothermal approach is used. For h-YMnO$_3$ it has been reported that O^{2-} interstitials occupy the AB-plane (which is perpendicular to the c-axis) [94]. In analogy to this, interstitial OH$^-$ in the AB-plane is a possible explanation of enlarged a compared to high-temperature synthesis approaches, as high hydroxide concentration is used in this study.

5.3 PROPOSED REACTION MECHANISM

Since a precipitate is formed when Ln(NO$_3$)$_3$ and KOH are mixed, the first step in the reaction from salt precursors is proposed to be a preciptitation of Ln(OH)$_3$:

$$\text{Ln}^{3+}(aq) + 3\text{OH}^-(aq) \longrightarrow \text{Ln(OH)}_3(s). \tag{5.1}$$
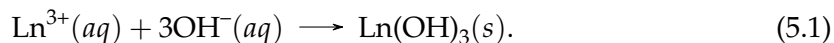
The presence of YbOOH in several products along with the phase composition's dependence on temperature and hydroxide concentration (see sections 5.1.1 and 5.1.2) suggest that dehydration of Ln(OH)$_3$ to LnOOH also is a step in the reaction:

$$\text{Ln(OH)}_3(s) \xrightarrow{\Delta} \text{LnOOH}(s) + \text{H}_2\text{O}. \tag{5.2}$$
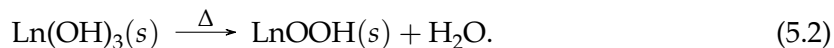
Exactly how the LnOOH phase reacts with manganese species to form h-LnMnO$_3$, and whether the reaction is a single step or consists of several, can not be determined from the experiments conducted in this study. An overall reaction equation between LnOOH and the manganese precursors used and in alkaline environment would be

$$\begin{aligned} 5\text{LnOOH}(s) + 4\text{Mn}^{2+}(aq) + \text{MnO}_4^-(aq) + 7\text{OH}^-(aq) \\ \longrightarrow 5\text{LnMnO}_3(s) + 6\text{H}_2\text{O}, \end{aligned} \tag{5.3}$$
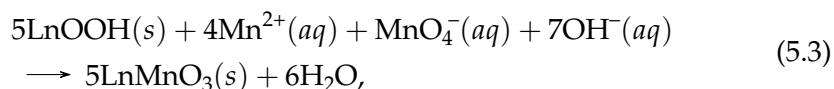
but Equation 5.3 may consist of several steps, and could for instance involve reaction between Mn^{2+} and Mn^{7+} to form Mn^{3+} before the manganese reacts with LnOOH. This would be in line with the brown color observed when mixing purple $KMnO_4$ with pink $MnCl_2$ (see Section 4.4).

The proposed total reaction when salt precursors are used becomes

$$5Ln(NO_3)_3(aq) + KMnO_4(aq) + 4MnCl_2(aq) + 22KOH(aq)$$
$$\longrightarrow 5LnMnO_3(s) + 11H_2O + 8KCl(aq) + 15KNO_3(aq),$$

(5.4)
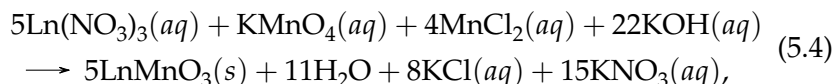
which is analogous to Equation 2.6 proposed by Kumar et al. [37], although the latter was proposed to consist of just a single step from dissolved ions.

The observations leading to these reactions to be proposed are in line with those made in the author's specialization project [84], and similar reaction steps were proposed and discussed in detail there. Since the reaction steps alone cannot explain the interesting differences between the yttrium and ytterbium system, a more comprehensive reaction mechanism is proposed in the following.

The proposed mechanism from salt precursors when yttrium is used is illustrated in Figure 5.1. Starting from dissolved Y^{3+} and OH^- ions, $Y(OH)_3$ particles nucleate and grow. They keep growing until they dehydrate to YOOH in an in situ transformation. After this transformation, growth can no longer occur as easily because growth species would have to first nucleate as $Y(OH)_3$ on the YOOH phase and then dehydrate. Hence, it is assumed that the size of the product h-$YMnO_3$ particles is largely determined by the size of the $Y(OH)_3$ particles when they dehydrate to YOOH. After the dehydration, YOOH can react with manganese species and hydroxide (possibly in the form of $Mn(OH)_4^-$) to form h-$YMnO_3$. Exactly how this reaction proceeds can not be determined with certainty from the experiments conducted in this study. It is possible that manganese and hydroxide diffuse into the YOOH phase and react directly towards h-$YMnO_3$ (see step *(a)* in Figure 5.1). However, nucleation of h-$YMnO_3$ on the surface of YOOH (step *(b)* in Figure 5.1) followed by growth on or into the YOOH phase may be more likely. If so, the possibly polycrystalline h-$YMnO_3$ particles without distinct hexagon shape could form when several h-$YMnO_3$ nuclei form on one YOOH particle and then grow together, whereas particles with hexagon shape are single-crystals arising from one nucleation site. Whether the reaction proceeds through step *(a)* or *(b)*, the size of the YOOH particles limits the size of the h-$YMnO_3$ particles because the reaction towards h-$YMnO_3$ proceeds via solid YOOH. The concentration of Y^{3+} in the solution is assumed to be very low because of the high hydroxide concentrations used in this study and the low solubility of $Y(OH)_3$ [93]. Most of the initial Y^{3+} will thus have precipitated as $Y(OH)_3$ and then dehydrated to YOOH, so that
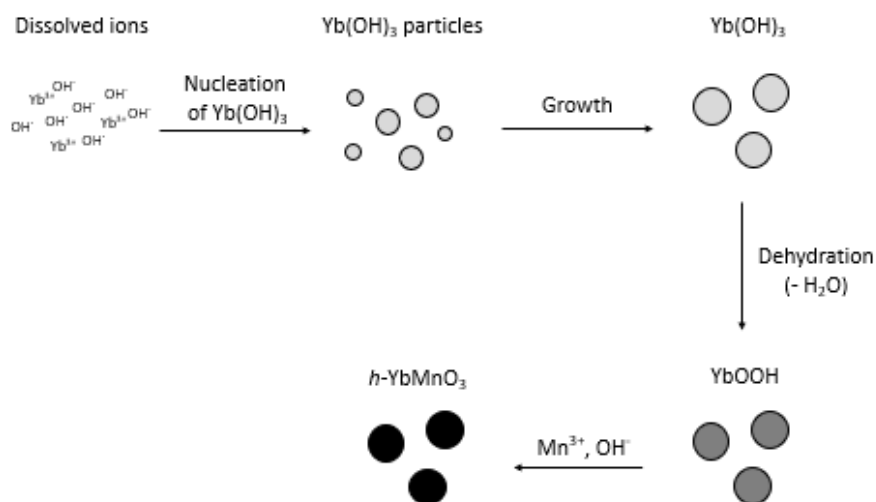
Salt precursors, Y
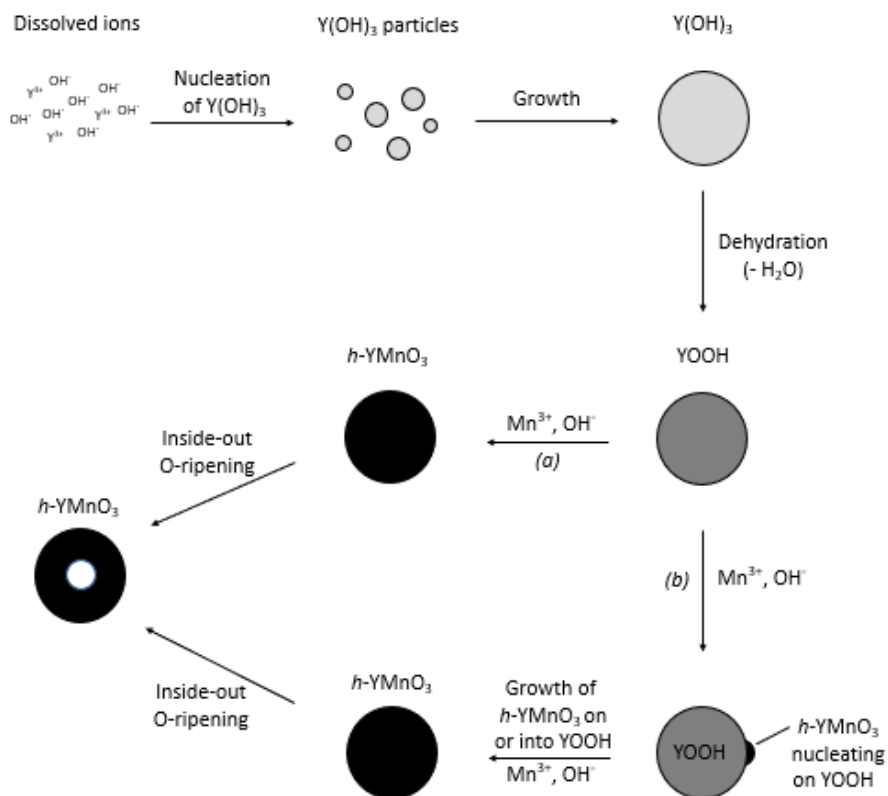
Figure 5.1: Proposed reaction mechanism for salt precursors when yttrium is used as the rare-earth element. The Mn^{3+} and OH^- reacting with YOOH to form h-YMnO$_3$ may be in the form of the $Mn(OH)_4^-$ complex.

h-YMnO$_3$ can only grow on or into the YOOH particles. The hypothesis that the size of the h-YMnO$_3$ particles is limited by the size of the YOOH particles they react from is also consistent with the h-YMnO$_3$ particle size displaying no clear dependence on reaction time (see Section 4.3.2). After having formed, the h-YMnO$_3$ particles eventually turn hollow by mechanism of Ostwald ripening when heated long enough (about 48-72 h).

When ytterbium is used instead of yttrium, several differences are seen in the products, as was discussed in detail in Section 5.1.5. The h-YbMnO$_3$ particles are dense and much smaller than the h-YMnO$_3$ particles, and incompletely reacted rare-earth element occurs in the YbOOH phase when ytterbium is used and in Y(OH)$_3$ when yttrium is used. It is thus proposed that while the dehydration from Ln(OH)$_3$ to LnOOH is the rate limiting step when Ln=Y, it is fast when Ln=Yb, leaving less time for Yb(OH)$_3$ to grow before dehydrating and thus resulting in smaller particles of YbOOH and in turn h-YbMnO$_3$ (see Figure 5.2 for proposed mechanism). XRD peak broadening observed for YbOOH, but not for Y(OH)$_3$ also indicates that the intermediate

Salt precursors, Yb

Figure 5.2: Proposed reaction mechanism for salt precursors when ytterbium is used as the rare-earth element. In the last step, manganese and hydroxide may either diffuse into the YbOOH phase and form h-YbMnO$_3$ directly (analogous to step *(a)* in Figure 5.1), or h-YbMnO$_3$ may nucleate on YbOOH and grow on or into it (analogous to step *(b)* in Figure 5.1). The Mn^{3+} and OH$^-$ reacting with YbOOH to form h-YbMnO$_3$ may be in the form of the Mn(OH)$_4^-$ complex.

Yb(OH)$_3$ particles dehydrate to YbOOH before reaching the size the Y(OH)$_3$ particles reach. While faster dehydration and thus shorter time to grow could be the reason why the Yb(OH)$_3$ are smaller when they dehydrate than the Y(OH)$_3$ particles are, it could also be due to higher solubility of Yb(OH)$_3$ [93], resulting in lower supersaturation and thus slower growth. A combination of the two effects is also possible.

The reaction from LnOOH to h-LnMnO$_3$, on the other hand (see Equation 5.3), may be faster when Ln=Y, which could explain why the inside-out Ostwald ripening is seen for h-YMnO$_3$, but not for h-YbMnO$_3$. The hypothesis that Equation 5.2 is rate limiting when Ln=Y and Equation 5.3 is rate limiting when Ln=Yb is substantiated by incompletely reacted rare-earth element occurring almost exclusively as YbOOH and Y(OH)$_3$ when Ln=Yb and Ln=Y, respectively.

When oxide precursors are used instead of salt precursors, similar difference in particle size from the two elements is not seen. The reaction from oxide precursors is thus assumed to follow the steps proposed by Stampler et al. [34]: First, Ln$_2$O$_3$ reacts with water to form hydroxide,

$$Ln_2O_3(s) + 3H_2O \longrightarrow 2Ln(OH)_3(s), \qquad (5.5)$$
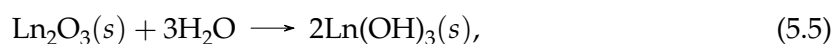
followed by dehydration (see Equation 5.2) and then by reaction between LnOOH and manganese, possibly in the form of dissolved $Mn(OH)_4^-$. The process is illustrated in Figure 5.3. If the reaction from oxide precursors goes via solid intermediates in each step as proposed, the size of the h-LnMnO$_3$ particles will be largely predetermined by the size of the precursors, explaining why the size of h-YMnO$_3$ and h-YbMnO$_3$ is not nearly as different as when salt precursors are used.

Oxide precursors
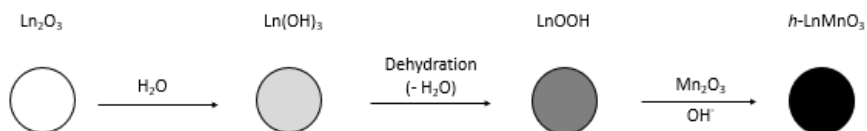
Figure 5.3: Proposed reaction mechanism for oxide precursors. In the last step, manganese species may either diffuse into the LnOOH phase and form h-LnMnO$_3$ directly (analogous to step *(a)* in Figure 5.1), or h-LnMnO$_3$ may nucleate on LnOOH and grow on or into it (analogous to step *(b)* in Figure 5.1). The Mn$_2$O$_3$ reacting with LnOOH to form h-LnMnO$_3$ may be dissolved as the $Mn(OH)_4^-$ complex.

CONCLUSION

An environmentally friendly, scalable, and low-temperature hydrothermal synthesis route of the lead-free ferroelectric material h-LnMnO$_3$ has been investigated in this study. Both h-YMnO$_3$ and h-YbMnO$_3$ have been successfully formed using this approach. For each rare-earth element, syntheses with and without h-LnMnO$_3$ yield have been carried out to determine what combinations of temperature and hydroxide concentration that allow for h-LnMnO$_3$ formation. High temperature and high hydroxide concentration are both seen to favor the formation of h-LnMnO$_3$. It is easier to form h-YbMnO$_3$ than h-YMnO$_3$ when the temperature is low; h-YbMnO$_3$ has been successfully formed at a temperature as low as 110 °C.

The h-LnMnO$_3$ formed has platelet morphology with platelet diameter ranging from below 1 μm to about 50 μm depending on rare-earth element and reaction conditions. When soluble salt precursors are used, significantly larger particles are seen with yttrium as the rare-earth element than with ytterbium. A similar effect is not seen when oxide precursors are used.

When yttrium is used, most platelets turn hollow after 48-72 h at elevated temperature, yielding a donut-like morphology that may be of interest for instance for catalysis purposes. Donut morphology is not seen for h-YbMnO$_3$.

Based on observations of how choice of rare-earth element and other reaction parameters affect the phase composition and microstructure of the products, a reaction mechanism for h-LnMnO$_3$ formation has been suggested. In the proposed mechanism, Ln(OH)$_3$ and LnOOH are intermediate phases, and particle growth primarily occurs in the Ln(OH)$_3$ phase. It is further proposed that dehydration of Y(OH)$_3$ to YOOH is the rate limiting step when yttrium is used as rare-earth element, whereas the reaction from YbOOH towards h-YbMnO$_3$ is rate limiting when ytterbium is used. Finally, it is suggested that the h-YMnO$_3$ platelets turn hollow by a mechanism of inside-out Ostwald ripening.

7

FURTHER WORK

While several aspects of hydrothermal synthesis of hexagonal rare-earth manganites have been investigated in this study, there is more work that must be done before this exciting field can be completely understood. For instance, in situ XRD data on the phases that form during the hydrothermal treatment would be of great interest, as such information would serve to strengthen or falsify the mechanism proposed in this work.

Experimenting with other rare-earth elements than yttrium and ytterbium could also be highly instructive. Several differences between the products from syntheses with yttrium and ytterbium have been observed, and further experiments with other elements could elucidate whether the differences are only due to different ionic radii or if other properties of the rare-earth element are important as well. For instance, a rare-earth element with larger radius than yttrium could be compared to one with smaller radius than ytterbium to see if similar but more extreme differences are observed than when comparing yttrium to ytterbium. This would be expected if manganites of other rare-earth elements are formed by the same mechanism and ionic radius of the rare-earth element is the primary factor governing the differences observed.

Testing the ferroelectric response of the products that were synthesized in this study would also be interesting, not only to confirm that the particles are ferroelectric and thus can be used in applications, but also to see if further differences caused by choice of rare-earth element or other reaction conditions could be detected. Raman spectroscopy was tried as a method for measuring the ferroelectric response, but was unsuccessful because the samples were burned by lower laser power than the power required to obtain a signal. A scanning probe technique may thus be better suited, but could not be carried out in this work because of the COVID-19 pandemic and the restrictions on instrument training that followed.

Catalytic activity could also be tested to assess the products' potential in applications. The small platelets observed when ytterbium is used as the rare-earth element could be very interesting for catalysis purposes due to large surface area, as could the donut morphology that results when yttrium is used.

Finally, the products could be characterized using a technique that allows for better quantitative data on size distribution than SEM does. Nanoparticle tracking analysis is an example of such a technique.

[1] Benjamin Tiller, Andrew Reid, Botong Zhu, José Guerreiro, Roger Domingo-Roca, Joseph Curt Jackson, and J. F.C. Windmill. "Piezoelectric microphone via a digital light processing 3D printing process." In: *Materials and Design* 165 (Mar. 2019). ISSN: 18734197. DOI: `10.1016/j.matdes.2019.107593`.

[2] Jean Yves Chapelon, Dominique Cathignol, Charles Cain, Emad Ebbini, Jan Ulco Kluiwstra, Oleg A. Sapozhnikov, Gérard Fleury, Rémi Berriet, Laurent Chupin, and Jean Luc Guey. "New piezoelectric transducers for therapeutic ultrasound." In: *Ultrasound in Medicine and Biology* 26.1 (Jan. 2000), pp. 153–159. ISSN: 03015629. DOI: `10.1016/S0301-5629(99)00120-9`.

[3] Paul M. Moubarak, Pinhas Ben-Tzvi, and Mona Elwakkad Zaghloul. "A self-calibrating mathematical model for the direct piezoelectric effect of a new MEMS tilt sensor." In: *IEEE Sensors Journal* 12.5 (2012), pp. 1033–1042. ISSN: 1530437X. DOI: `10.1109/JSEN.2011.2173188`.

[4] James F. Tressler. "Piezoelectric transducer designs for sonar applications." In: *Piezoelectric and Acoustic Materials for Transducer Applications*. Springer US, 2008, pp. 217–239. ISBN: 9780387765389. DOI: `10.1007/978-0-387-76540-2{\_}11`.

[5] Mohd Hanif Mohd Ramli and Xinkai Chen. "Modelling and control of piezoelectric actuators by a class of differential equations-based hysteresis models." In: *International Journal of Advanced Mechatronic Systems* 7.3 (2017), p. 165. ISSN: 1756-8412. DOI: `10.1504/IJAMECHS.2017.086201`. URL: `http://www.inderscience.com/link.php?id=86201`.

[6] Christopher A. Howells. "Piezoelectric energy harvesting." In: *Energy Conversion and Management* 50.7 (July 2009), pp. 1847–1850. ISSN: 01968904. DOI: `10.1016/j.enconman.2009.02.020`.

[7] Zhengbao Yang, Shengxi Zhou, Jean Zu, and Daniel Inman. *High-Performance Piezoelectric Energy Harvesters and Their Applications*. Apr. 2018. DOI: `10.1016/j.joule.2018.03.011`.

[8] Hailu Yang, Linbing Wang, Bin Zhou, Ya Wei, and Qian Zhao. "A preliminary study on the highway piezoelectric power supply system." In: *International Journal of Pavement Research and Technology* 11.2 (Mar. 2018), pp. 168–175. ISSN: 19971400. DOI: `10.1016/j.ijprt.2017.08.006`.

[9] Lu You et al. "Origin of giant negative piezoelectricity in a layered van der Waals ferroelectric." In: *Science Advances* 5.4 (2019). ISSN: 23752548. DOI: `10.1126/sciadv.aav3780`.

[10]   J. Fousek. "Joseph Valasek and the discovery of ferroelectricity." In: *Proceedings of 1994 IEEE International Symposium on Applications of Ferroelectrics*. IEEE, pp. 1–5. ISBN: 0-7803-1847-1. DOI: 10.1109/ISAF.1994.522283. URL: http://ieeexplore.ieee.org/document/522283/.

[11]   Glen R. Fox, Richard Bailey, William B. Kraus, Fan Chu, Shan Sun, and Tom Davenport. "The Current Status of FeRAM." In: Mar. 2004, pp. 139–148. DOI: 10.1007/978-3-540-45163-1{_}10.

[12]   T. Mikolajick, C. Dehm, W. Hartner, I. Kasko, M. J. Kastner, N. Nagel, M. Moert, and C. Mazure. "FeRAM technology for high density applications." In: *Microelectronics Reliability* 41.7 (2001), pp. 947–950. ISSN: 00262714. DOI: 10.1016/S0026-2714(01)00049-X.

[13]   All Sheikholeslami and P. Glenn Gulak. "A survey of circuit innovations in random-access memories." In: *Proceedings of the IEEE* 88.5 (2000), pp. 667–689. ISSN: 00189219. DOI: 10.1109/5.849164.

[14]   Zhang Liang, Chang Feng Yan, Sami Rtimi, and Jayasundera Bandara. "Piezoelectric materials for catalytic/photocatalytic removal of pollutants: Recent advances and outlook." In: *Applied Catalysis B: Environmental* 241 (Feb. 2019), pp. 256–269. ISSN: 09263373. DOI: 10.1016/j.apcatb.2018.09.028.

[15]   Jiang Wu, Ni Qin, and Dinghua Bao. "Effective enhancement of piezocatalytic activity of BaTiO3 nanowires under ultrasonic vibration." In: *Nano Energy* (2018). ISSN: 22112855. DOI: 10.1016/j.nanoen.2017.12.034.

[16]   Shufan Jia, Yiping Su, Boping Zhang, Zhicheng Zhao, Shun Li, Yunfei Zhang, Pucai Li, Mingyuan Xu, and Ran Ren. "Few-layer MoS2 nanosheet-coated KNbO3 nanowire heterostructures: Piezo-photocatalytic effect enhanced hydrogen production and organic pollutant degradation." In: *Nanoscale* 11.16 (Apr. 2019), pp. 7690–7700. ISSN: 20403372. DOI: 10.1039/c9nr00246d.

[17]   Shuya Xu, Zhihong Liu, Maolin Zhang, and Limin Guo. "Piezotronics enhanced photocatalytic activities of Ag-BaTiO3 plasmonic photocatalysts." In: *Journal of Alloys and Compounds* 801 (Sept. 2019), pp. 483–488. ISSN: 09258388. DOI: 10.1016/j.jallcom.2019.06.115.

[18]   Arvin Kakekhani, Sohrab Ismail-Beigi, and Eric I. Altman. "Ferroelectrics: A pathway to switchable surface chemistry and catalysis." In: *Surface Science* 650 (Aug. 2016), pp. 302–316. ISSN: 00396028. DOI: 10.1016/j.susc.2015.10.055.

[19] P. K. Panda and B. Sahoo. "PZT to Lead Free Piezo Ceramics: A Review." In: *Ferroelectrics* 474.1 (Jan. 2015), pp. 128–143. ISSN: 0015-0193. DOI: 10.1080/00150193.2015.997146. URL: http://www.tandfonline.com/doi/abs/10.1080/00150193.2015.997146.

[20] *DIRECTIVE 2002/95/EC OF THE EUROPEAN PARLIAMENT AND OF THE COUNCIL of 27 January 2003 on the restriction of the use of certain hazardous substances in electrical and electronic equipment*. Tech. rep.

[21] Wenfeng Liu and Xiaobing Ren. "Large piezoelectric effect in Pb-free ceramics." In: *Physical Review Letters* 103.25 (Dec. 2009). ISSN: 00319007. DOI: 10.1103/PhysRevLett.103.257602.

[22] H. Khassaf, N. Khakpash, F. Sun, N. M. Sbrockey, G. S. Tompa, T. S. Kalkur, and S. P. Alpay. "Strain engineered barium strontium titanate for tunable thin film resonators." In: *Applied Physics Letters* 104.20 (May 2014). ISSN: 00036951. DOI: 10.1063/1.4879281.

[23] Yasuyoshi Saito, Hisaaki Takao, Toshihiko Tani, Tatsuhiko Nonoyama, Kazumasa Takatori, Takahiko Homma, Toshiatsu Nagaya, and Masaya Nakamura. "Lead-free piezoceramics." In: *Nature* 432.7013 (Nov. 2004), pp. 84–87. ISSN: 00280836. DOI: 10.1038/nature03028.

[24] Ahmad Safari and Mehdi Hejazi. "Lead-free KNN-based piezoelectric materials." In: *Lead-Free Piezoelectrics*. Vol. 9781441995988. Springer New York, Nov. 2013, pp. 139–175. ISBN: 9781441995988. DOI: 10.1007/978-1-4419-9598-8{_}5. URL: https://link.springer.com/chapter/10.1007/978-1-4419-9598-8_5.

[25] Didrik René Småbråten. "Defect chemistry and ferroelectric domain walls in hexagonal manganites." PhD thesis. NTNU, 2018.

[26] Sandra H. Skjærvø, Quintin N. Meier, Mikhail Feygenson, Nicola A. Spaldin, Simon J.L. Billinge, Emil S. Bozin, and Sverre M. Selbach. "Unconventional Continuous Structural Disorder at the Order-Disorder Phase Transition in the Hexagonal Manganites." In: *Physical Review X* 9.3 (July 2019), p. 031001. ISSN: 21603308. DOI: 10.1103/PhysRevX.9.031001.

[27] Alexandra S Gibbs, Kevin S Knight, and Philip Lightfoot. "High-temperature phase transitions of hexagonal YMnO 3." In: *PHYSICAL REVIEW B* 83 (2011), p. 94111. DOI: 10.1103/PhysRevB.83.094111.

[28] Xin Huang, Tula R Paudel, Shuai Dong, and Evgeny Y Tsymbal. "Hexagonal rare-earth manganites as promising photovoltaics and light polarizers." In: *PHYSICAL REVIEW B* 92 (2015), p. 125201. DOI: 10.1103/PhysRevB.92.125201.

[29]   S. C. Abrahams. "Ferroelectricity and structure in the YMnO3 family." In: *Acta Crystallographica Section B: Structural Science* 57.4 (Aug. 2001), pp. 485–490. ISSN: 01087681. DOI: 10.1107/S0108768101009399.

[30]   Bas B. Van Aken, Thomas T.M. Palstra, Alessio Filippetti, and Nicola A. Spaldin. "The origin of ferroelectricity in magnetoelectric YMnO3." In: *Nature Materials* 3.3 (2004), pp. 164–170. ISSN: 14761122. DOI: 10.1038/nmat1080.

[31]   M. Fiebig, Th Lottermoser, D. Fröhlich, A. V. Goltsev, and R. V. Pisarev. "Observation of coupled magnetic and electric domains." In: *Nature* 419.6909 (Oct. 2002), pp. 818–820. ISSN: 00280836. DOI: 10.1038/nature01077.

[32]   Tobias Kosub et al. "Purely antiferromagnetic magnetoelectric random access memory." In: *Nature Communications* 8.1 (Jan. 2017), pp. 1–7. ISSN: 20411723. DOI: 10.1038/ncomms13985.

[33]   Kenneth P. Marshall, Anders B. Blichfeld, Susanne L. Skjærvø, Ola G. Grendal, Wouter Beek, Sverre M. Selbach, Tor Grande, and Mari-Ann Einarsrud. "A Fast, Low-Temperature Synthesis Method for Hexagonal YMnO ₃ : Kinetics, Purity, Size and Shape as Studied by In Situ X-ray Diffraction." In: *Chemistry − A European Journal* (May 2020), chem.202000528. ISSN: 0947-6539. DOI: 10.1002/chem.202000528. URL: https://onlinelibrary.wiley.com/doi/abs/10.1002/chem.202000528.

[34]   Evan S. Stampler, William C. Sheets, Wilfrid Prellier, Tobin J. Marks, and Kenneth R. Poeppelmeier. "Hydrothermal synthesis of LnMnO3 (Ln = Ho-Lu and Y): Exploiting amphoterism in late rare-earth oxides." In: *Journal of Materials Chemistry* 19.25 (2009), pp. 4375–4381. ISSN: 09599428. DOI: 10.1039/b900370c.

[35]   M. H. Harunsani, J. Li, Y. B. Qin, H. T. Tian, J. Q. Li, H. X. Yang, and R. I. Walton. "Spontaneous formation of circular and vortex ferroelectric domain structure in hexagonal YMnO3 and YMn0.9Fe0.1O3 prepared by low temperature solution synthesis." In: *Applied Physics Letters* 107.6 (Aug. 2015). DOI: 10.1063/1.4928565.

[36]   H. W. Zheng, Y. F. Liu, W. Y. Zhang, S. J. Liu, H. R. Zhang, and K. F. Wang. "Spin-glassy behavior and exchange bias effect of hexagonal YMnO3 nanoparticles fabricated by hydrothermal process." In: *Journal of Applied Physics* 107.5 (2010). ISSN: 00218979. DOI: 10.1063/1.3296323.

[37]   R. Dhinesh Kumar and R. Jayavel. "Low temperature hydrothermal synthesis and magnetic studies of YMnO 3 nanorods." In: *Materials Letters* 113 (2013), pp. 210–213. ISSN: 0167577X. DOI: 10.1016/j.matlet.2013.09.070.

[38] Richard I. Walton. *Perovskite Oxides Prepared by Hydrothermal and Solvothermal Synthesis: A Review of Crystallisation, Chemistry, and Compositions*. 2020. DOI: 10.1002/chem.202000707.

[39] Per Martin Rørvik, Åsmund Almli, Antonius T.J. Van Helvoort, Randi Holmestad, Thomas Tybell, Tor Grande, and Mari Ann Einarsrud. "PbTiO3 nanorod arrays grown by self-assembly of nanocrystals." In: *Nanotechnology* 19.22 (June 2008). ISSN: 09574484. DOI: 10.1088/0957-4484/19/22/225605.

[40] Per Martin Rørvik, Tor Grande, and Mari Ann Einarsrud. *One-dimensional nanostructures of ferroelectric perovskites*. Sept. 2011. DOI: 10.1002/adma.201004676.

[41] Roger Whatmore. "Ferroelectric materials." In: *Springer Handbooks*. Springer, 2017, p. 1. DOI: 10.1007/978-3-319-48933-9{_}26.

[42] Jian-Jun Wang, Bo Wang, and Long-Qing Chen. "Understanding, Predicting, and Designing Ferroelectric Domain Structures and Switching Guided by the Phase-Field Method." In: *Annual Review of Materials Research* 49.1 (July 2019), pp. 127–152. ISSN: 1531-7331. DOI: 10.1146/annurev-matsci-070218-121843. URL: https://www.annualreviews.org/doi/10.1146/annurev-matsci-070218-121843.

[43] Longyue Liang, Xueliang Kang, Yuanhua Sang, and Hong Liu. *One-dimensional ferroelectric nanostructures: Synthesis, properties, and applications*. 2016. DOI: 10.1002/advs.201500358.

[44] Gordon E. Moore. "Cramming more components onto integrated circuits, Reprinted from Electronics, volume 38, number 8, April 19, 1965, pp.114 ff." In: *IEEE Solid-State Circuits Society Newsletter* 11.3 (Feb. 2009), pp. 33–35. ISSN: 1098-4232. DOI: 10.1109/n-ssc.2006.4785860.

[45] Andrew J. Medford, Aleksandra Vojvodic, Jens S. Hummelshøj, Johannes Voss, Frank Abild-Pedersen, Felix Studt, Thomas Bligaard, Anders Nilsson, and Jens K. Nørskov. "From the Sabatier principle to a predictive theory of transition-metal heterogeneous catalysis." In: *Journal of Catalysis* 328 (July 2015), pp. 36–42. ISSN: 10902694. DOI: 10.1016/j.jcat.2014.12.033.

[46] T. Katsufuji et al. "Crystal structure and magnetic properties of hexagonal (formula presented) Lu, and Sc) and the effect of doping." In: *Physical Review B - Condensed Matter and Materials Physics* 66.13 (2002), pp. 1–8. ISSN: 1550235X. DOI: 10.1103/PhysRevB.66.134434.

[47] J. Liu, C. Toulouse, P. Rovillain, M. Cazayous, Y. Gallais, M. A. Measson, N. Lee, S. W. Cheong, and A. Sacuto. "Lattice and spin excitations in multiferroic h-YbMnO 3." In: *Physical Review B -*

Condensed Matter and Materials Physics 86.18 (Nov. 2012). ISSN: 10980121. DOI: `10.1103/PhysRevB.86.184410`.

[48]   X. Fabrèges, I. Mirebeau, P. Bonville, S. Petit, G. Lebras-Jasmin, A. Forget, G. André, and S. Pailhès. "Magnetic order in YbMnO3 studied by neutron diffraction and Mössbauer spectroscopy." In: *Physical Review B - Condensed Matter and Materials Physics* 78.21 (Dec. 2008), p. 214422. ISSN: 10980121. DOI: `10.1103/PhysRevB.78.214422`.

[49]   Bernd Lorenz. " Hexagonal Manganites—(RMnO 3): Class (I) Multiferroics with Strong Coupling of Magnetism and Ferroelectricity." In: *ISRN Condensed Matter Physics* 2013 (2013), pp. 1–43. DOI: `10.1155/2013/497073`.

[50]   Ming Chen, Bengt Hallstedt, and Ludwig J. Gauckler. "Thermodynamic assessment of the Mn-Y-O system." In: *Journal of Alloys and Compounds* 393.1-2 (May 2005), pp. 114–121. ISSN: 09258388. DOI: `10.1016/j.jallcom.2004.09.057`.

[51]   V. F. Balakirev, L. B. Vedmid', A. M. Yankin, and Yu V. Golikov. "P-T-X phase diagram of the Yb-Mn-O system." In: *Doklady Physical Chemistry* 400.1-4 (2005), pp. 1–3. ISSN: 00125016. DOI: `10.1007/s10634-005-0011-x`.

[52]   James J De Yoreo and Peter G Vekilov. *Principles of Crystal Nucleation and Growth*. Tech. rep.

[53]   Guozhong Cao and Ying Wang. *Nanostructures and Nanomaterials*. Vol. 2. World Scientific Series in Nanoscience and Nanotechnology. WORLD SCIENTIFIC, Jan. 2011, pp. 61–74. ISBN: 978-981-4322-50-8. DOI: `10.1142/7885`. URL: `https://www.worldscientific.com/worldscibooks/10.1142/7885`.

[54]   Steven S. Zumdahl. *Chemical principles*. Houghton Mifflin, 2009, p. 102. ISBN: 9780618946907.

[55]   "Heterogeneous nucleation." In: *Pergamon Materials Series* 15.C (2010), pp. 165–226. ISSN: 14701804. DOI: `10.1016/S1470-1804(09)01506-5`.

[56]   S. Karthika, T. K. Radhakrishnan, and P. Kalaichelvi. "A Review of Classical and Nonclassical Nucleation Theories." In: *Crystal Growth and Design* 16.11 (Nov. 2016), pp. 6663–6681. ISSN: 15287505. DOI: `10.1021/acs.cgd.6b00794`.

[57]   Jens-Petter Andreassen and Alison Emslie Lewis. "Classical and Nonclassical Theories of Crystal Growth." In: *New Perspectives on Mineral Nucleation and Growth*. Springer International Publishing, 2017, pp. 137–154. DOI: `10.1007/978-3-319-45669-0{\_}7`.

[58]   E. D. Bøjesen and B. B. Iversen. *The chemistry of nucleation*. Oct. 2016. DOI: `10.1039/c6ce01489e`. URL: `https://pubs.rsc.org/en/content/articlehtml/2016/ce/c6ce01489ehttps://pubs.rsc.org/en/content/articlelanding/2016/ce/c6ce01489e`.

[59] Jörg Polte. "Fundamental growth principles of colloidal metal nanoparticles - a new perspective." In: *CrystEngComm* 17.36 (June 2015), pp. 6809–6830. ISSN: 14668033. DOI: 10.1039/c5ce01014d. URL: www.rsc.org/crystengcomm.

[60] Wangsuo Weng, Jun Lin, Yichen Du, Xufang Ge, Xiaosi Zhou, and Jianchun Bao. *Template-free synthesis of metal oxide hollow micro-/nanospheres: Via Ostwald ripening for lithium-ion batteries.* June 2018. DOI: 10.1039/c8ta03161d.

[61] See Wee Chee, Shu Fen Tan, Zhaslan Baraissov, Michel Bosman, and Utkur Mirsaidov. "Direct observation of the nanoscale Kirkendall effect during galvanic replacement reactions." In: *Nature Communications* 8.1 (Dec. 2017), pp. 1–8. ISSN: 20411723. DOI: 10.1038/s41467-017-01175-2.

[62] Yadong Yin, Robert M. Rioux, Can K. Erdonmez, Steven Hughes, Gabor A. Somorjal, and A. Paul Alivisatos. "Formation of Hollow Nanocrystals Through the Nanoscale Kirkendall Effect." In: *Science* 304.5671 (Apr. 2004), pp. 711–714. ISSN: 00368075. DOI: 10.1126/science.1096566.

[63] Wenshou Wang, Michael Dahl, and Yadong Yin. *Hollow nanocrystals through the nanoscale Kirkendall effect.* Apr. 2013. DOI: 10.1021/cm3030928.

[64] F. Merkoçi, J. Patarroyo, L. Russo, J. Piella, A. Genç, J. Arbiol, N. G. Bastús, and V. Puntes. "Understanding galvanic replacement reactions: the case of Pt and Ag." In: *Materials Today Advances* 5 (Mar. 2020), p. 100037. ISSN: 25900498. DOI: 10.1016/j.mtadv.2019.100037.

[65] Surangkana Wannapop, Titipun Thongtem, and Somchai Thongtem. "Characterization of Donut-Like SrMoO 4 Produced by Microwave-Hydrothermal Process." In: *Journal of Nanomaterials* 2013 (2013). DOI: 10.1155/2013/474576. URL: http://dx..

[66] Xiong Wen Lou, Yong Wang, Chongli Yuan, Jim Yang Lee, and Lynden A. Archer. "Template-free synthesis of SnO2 hollow nanostructures with high lithium storage capacity." In: *Advanced Materials* 18.17 (Sept. 2006), pp. 2325–2329. ISSN: 09359648. DOI: 10.1002/adma.200600733. URL: http://doi.wiley.com/10.1002/adma.200600733.

[67] Hua Gui Yang and Hua Chun Zeng. "Preparation of hollow anatase TiO2 nanospheres via Ostwald ripening." In: *Journal of Physical Chemistry B* 108.11 (Mar. 2004), pp. 3492–3495. ISSN: 15206106. DOI: 10.1021/jp0377782.

[68] Li Zhang and Hui Wang. "Interior structural tailoring of Cu2O shell-in-shell nanostructures through multistep Ostwald ripening." In: *Journal of Physical Chemistry C* 115.38 (Sept. 2011), pp. 18479–18485. ISSN: 19327447. DOI: 10.1021/jp2059613.

[69]   Hua Chun Zeng. "Ostwald Ripening: A Synthetic Approach for Hollow Nanomaterials." In: *Current Nanoscience* 3.2 (May 2007), pp. 177–181. ISSN: 15734137. DOI: 10.2174/157341307780619279. URL: http://www.eurekaselect.com/openurl/content.php?genre=article&issn=1573-4137&volume=3&issue=2&spage=177.

[70]   W. N. Budhysutanto, F. J. Van Den Bruele, B. D. Rossenaar, D. Van Agterveld, W. J.P. Van Enckevort, and H. J.M. Kramer. "A unique growth mechanism of donut-shaped MgAl layered double hydroxides crystals revealed by AFM and STEMEDX." In: *Journal of Crystal Growth*. Vol. 318. 1. North-Holland, Mar. 2011, pp. 110–116. DOI: 10.1016/j.jcrysgro.2010.10.083.

[71]   Mari Ann Einarsrud and Tor Grande. *1D oxide nanostructures from chemical solutions*. Apr. 2014. DOI: 10.1039/c3cs60219b.

[72]   Richard I Walton. "Subcritical solvothermal synthesis of condensed inorganic materials." In: (2002). DOI: 10.1039/b105762f.

[73]   Bonnie L. Gersten. "Growth of Multicomponent Perovskite Oxide Crystals." In: *Crystal Growth Technology*. Elsevier, 2003, pp. 299–333. DOI: 10.1016/b978-081551453-4.50011-7.

[74]   Yoko Ohba, Tatsuo Rikitoku, Takaaki Tsurumi, and Masaki Daimon. "Precipitation of Lead Zirconate Titanate Powders under Hydrothermal Conditions." In: *Journal of the Ceramic Society of Japan* 104 (1996), pp. 6–10.

[75]   Chang Tai Xia, Er Wei Shi, Wei Zhuo Zhong, and Jing Kun Guo. "Preparation of BaTiO3 by the hydrothermal method." In: *Journal of the European Ceramic Society* 15.12 (1995), pp. 1171–1176. ISSN: 09552219. DOI: 10.1016/0955-2219(95)00101-8.

[76]   Jooho Moon, Melanie L. Carasso, Henrik G. Krarup, Jeffrey A. Kerchner, and James H. Adair. "Particle-shape control and formation mechanisms of hydrothermally derived lead titanate." In: *Journal of Materials Research* 14.3 (1999), pp. 866–875. ISSN: 08842914. DOI: 10.1557/JMR.1999.0116.

[77]   Reza Asiaie, Weidong Zhu, Sheikh A. Akbar, and Prabir K. Dutta. "Characterization of submicron particles of tetragonal BaTiO3." In: *Chemistry of Materials* 8.1 (1996), pp. 226–234. ISSN: 08974756. DOI: 10.1021/cm950327c.

[78]   Takashi Ichihara, Takaaki Tsurumi, Kiyoshi Asaga, Kyung Hee Lee, and Masaki Daimon. "Hydrothermal synthesis of PZT crystalline powder and piezoelectric property of ceramics." In: *Nippon Seramikkusu Kyokai Gakujutsu Ronbunshi/Journal of the Ceramic Society of Japan* 98.2 (1990), pp. 150–155. ISSN: 09145400. DOI: 10.2109/jcersj.98.150.

[79] Jae Young Choi, Chong Hee Kim, and Do Kyung Kim. "Hydrothermal Synthesis of Spherical Perovskite Oxide Powders Using Spherical Gel Powders." In: *Journal of the American Ceramic Society* 81.5 (Jan. 2005), pp. 1353–1356. ISSN: 00027820. DOI: 10.1111/j.1151-2916.1998.tb02490.x. URL: http://doi.wiley.com/10.1111/j.1151-2916.1998.tb02490.x.

[80] Michael Z.C. Hu, Vino Kurian, E. Andrew Payzant, Claudia J. Rawn, and Rodney D. Hunt. "Wet-chemical synthesis of monodispersed barium titanate particles - Hydrothermal conversion of TiO2 microspheres to nanocrystalline BaTiO3." In: *Powder Technology*. Vol. 110. 1-2. Elsevier Sequoia SA, May 2000, pp. 2–14. DOI: 10.1016/S0032-5910(99)00262-4.

[81] Bonnie Gersten and Jennifer Synowczynski. "Hydrothermal synthesis of pure barium strontium titanate." In: *IEEE International Symposium on Applications of Ferroelectrics*. Vol. 1. 2000, pp. 75–78. DOI: 10.1109/isaf.2000.941515.

[82] P. V. Klevtsov and L. P. Sheina. "Hydrothermal Synthesis and Crystal Structure of Rare-earth Hydroxides." In: *Neorganicheskie Materialy* 1.6 (1965), pp. 912–917.

[83] S Mroczkowski, J Eckert, H Meissner, and J C Doran. *Hydrothermal growth of single crystals of rare earth hydroxides*. Tech. rep. 1970, p. 33.

[84] Sigurd Opdal Eidem. *Synthesis of Nanostructured Hexagonal Manganites*. Tech. rep. NTNU, 2019.

[85] *Model 4749 General Purpose Acid Digestion Vessels, 5 mL – 23mL Documents - Parr Instrument Company*. URL: https://www.parrinst.com/products/sample-preparation/acid-digestion/general-purpose-acid-digestion-vessel-model-4749-23-ml/documents/.

[86] *Series 4760 General Purpose Pressure Vessels, 100-600 mL Documents - Parr Instrument Company*. URL: https://www.parrinst.com/products/non-stirred-pressure-vessels/series-4760/documents/.

[87] *4838 Reactor Controller Documents - Parr Instrument Company*. URL: https://www.parrinst.com/products/controllers/4838-reactor-controller/documents/.

[88] A. Sanjid, Parama Chakraborty Banerjee, and R. K.Singh Raman. "Multi-layer graphene coating for corrosion resistance of Monel 400 alloy in chloride environment." In: *Surface and Coatings Technology* 370 (July 2019), pp. 227–234. ISSN: 02578972. DOI: 10.1016/j.surfcoat.2019.04.077.

[89] Alan A. Coelho. "TOPAS and TOPAS-Academic: An optimization program integrating computer algebra and crystallographic objects written in C++: An." In: *Journal of Applied Crystallography* 51.1 (Feb. 2018), pp. 210–218. ISSN: 16005767. DOI: 10.1107/S1600576718000183.

[90] Peter W. Stephens. "Phenomenological model of anisotropic peak broadening in powder diffraction." In: *Journal of Applied Crystallography* 32.2 (1999), pp. 281–289. ISSN: 00218898. DOI: 10.1107/S0021889898006001.

[91] T. Choi, Y. Horibe, H. T. Yi, Y. J. Choi, Weida Wu, and S. W. Cheong. "Insulating interlocked ferroelectric and structural antiphase domain walls in multiferroic YMnO 3." In: *Nature Materials* 9.3 (Feb. 2010), pp. 253–258. ISSN: 14764660. DOI: 10.1038/nmat2632.

[92] T. Katsufuji, S. Mori, M. Masaki, Y. Moritomo, N. Yamamoto, and H. Takagi. "Dielectric and magnetic anomalies and spin frustration in hexagonal RMnO3 (R = Y, Yb, and Lu)." In: *Physical Review B* 64.10 (Aug. 2001), p. 104419. DOI: 10.1103/PhysRevB.64.104419. URL: https://link.aps.org/doi/10.1103/PhysRevB.64.104419.

[93] Z Orhanovic, B Pokric, H Furedi, and M Branica. "Precipitation and Hydrolysis of Metallic Ions. III. Studies on the Solubility of Yttrium and Some Rare Earth Hydroxides." In: *Croatica Chemica Acta* 38 (1966), pp. 269–276.

[94] Sandra H. Skjærvø, Espen T. Wefring, Silje K. Nesdal, Nikolai H. Gaukås, Gerhard H. Olsen, Julia Glaum, Thomas Tybell, and Sverre M. Selbach. "Interstitial oxygen as a source of p-type conductivity in hexagonal manganites." In: *Nature Communications* 7 (Dec. 2016). ISSN: 20411723. DOI: 10.1038/ncomms13745.

APPENDICES

A

ADDITIONAL SEM IMAGES

Figures A.1 and A.2 illustrate how the quantitative measurement of particle and hole diameter was carried out for the Y1-21 - Y4-21 products. In addition, an example of the broken particles the Y-16 product consists of is shown in Figure A.3, as SEM images of that product were not included in the main text. As mentioned in Section 4.3.2, the size and exact morphology of the particles could not be determined due to all particles being broken.
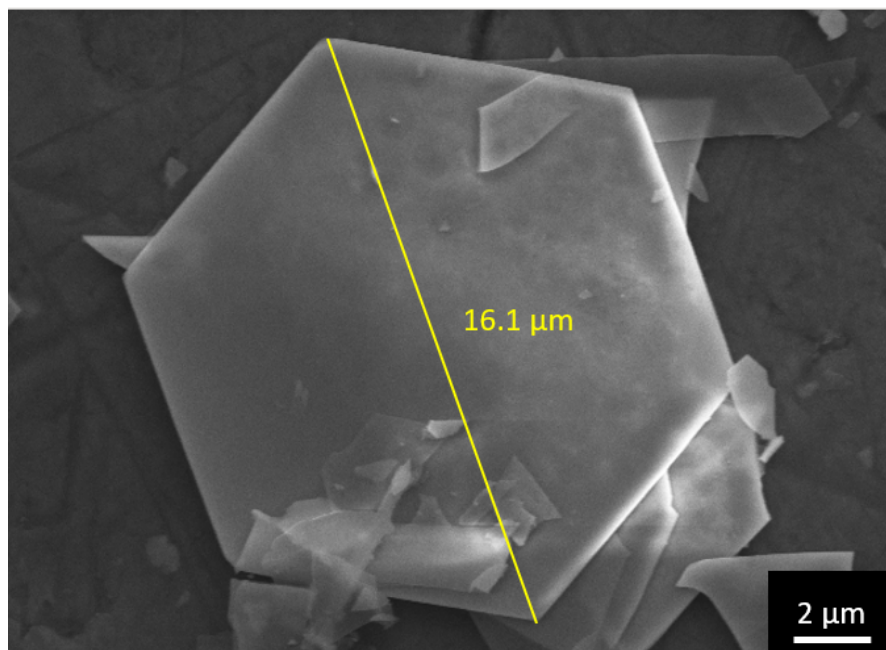
Figure A.1: Example of measurement of particle diameter. This h-YMnO$_3$ particle is from the Y2-21 product.
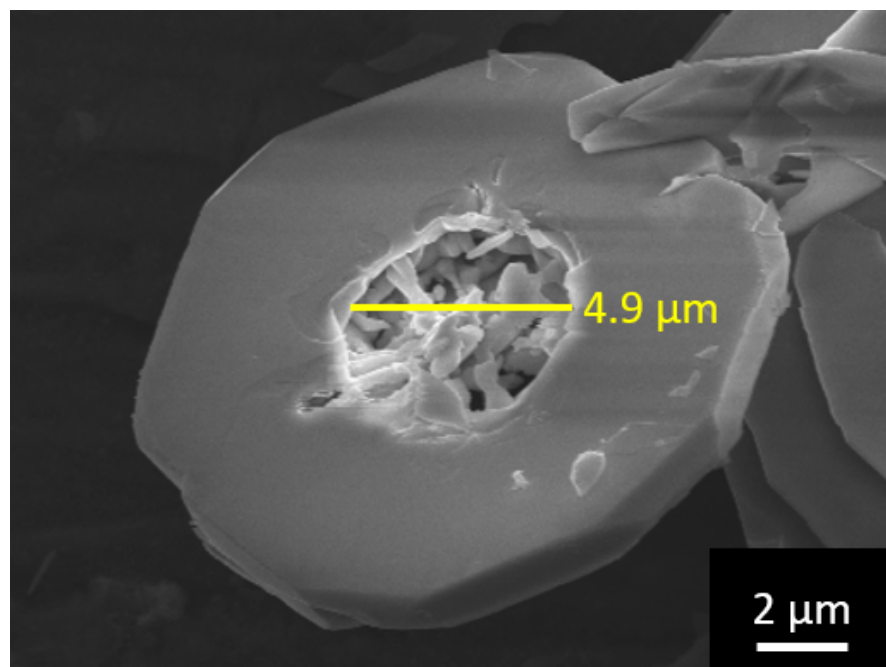
Figure A.2: Example of measurement of hole diameter, here of a hole that has not yet completely formed. This h-YMnO$_3$ particle is from the Y3-21 product.
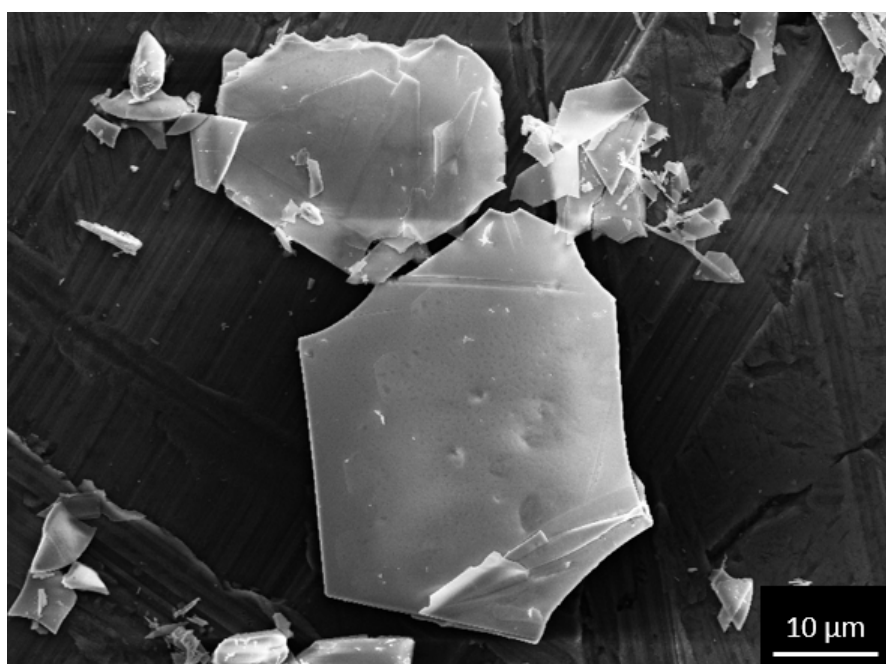
Figure A.3: Example of broken *h*-YMnO$_3$ particles from the Y-16 product.

FULL PRODUCT COMPOSITIONS

In this appendix, the full phase composition (in wt%) is given for all products on which Rietveld refinements were successfully performed. For the sake of completeness, even minor phases are included. "-" is written when a phase is not present (or has a lower purity than 0.5 wt%).The products are structured in tables where each table puts emphasis on one reaction parameter.

Table B.1: Composition as a function of temperature. Full product composition and Rwp values obtained from Rietveld refinements of the synthesis products included in Figure 4.1, apart from the three syntheses at 150 °C and with 21.2 M KOH, whose product compositions can be found in Table B.7, and the Yb1-11 syntheses, for which a Rietveld refinement has not been performed. Hydroxide concentration can be read out of the synthesis ID, and reaction temperature is given in the table. Apart from those two parameters, all syntheses were performed under identical conditions.

ID	T [°C]	h-YbMnO$_3$ [wt%]	YbOOH [wt%]	YbMn$_2$O$_5$ [wt%]	Mn$_3$O$_4$ [wt%]	Yb$_2$Mn$_2$O$_7$ [wt%]	KMn$_2$O$_{5.44}$ [wt%]	Rwp
Yb2-11	130	67	20	2	11	1	-	9.4
Yb4-11	150	75	18	-	5	1	1	8.0
Yb1-21	110	48	36	3	10	1	2	8.9
Yb2-21	130	75	18	1	5	-	-	7.5
Yb7-21	240	86	-	4	3	7	-	11.7

Table B.2: Composition as a function of hydroxide concentration. Full product composition and Rwp values obtained from Rietveld refinements of the products from the Y-16 and Y2-21 syntheses. Apart from hydroxide concentrations, all syntheses were performed under identical conditions.

ID	h-YMnO$_3$ [wt%]	Y(OH)$_3$ [wt%]	YMn$_2$O$_5$ [wt%]	Mn$_3$O$_4$ [wt%]	Y$_2$Mn$_2$O$_7$ [wt%]	KMn$_2$O$_{5.44}$ [wt%]	o-YMnO$_3$ [wt%]	Rwp
Y-16	81	3	13	1	1	1	1	11.5
Y2-21	90	-	3	1	1	1	4	11.3

Table B.3: Composition as a function of reaction time, ytterbium. Full product composition and Rwp values obtained from Rietveld refinements of the Yb2-11, Yb3-11, Yb7-21, and Yb8-21 synthesis products. Hydroxide concentration can be read out of the synthesis ID, and reaction temperature and time are given in the table. Apart from those three parameters, all syntheses were performed under identical conditions.

ID	Yb2-11	Yb3-11	Yb7-21	Yb8-21
T [°C]	130	130	240	240
Time [h]	24	72	24	72
h-YbMnO$_3$ [wt%]	67	76	86	84
YbOOH [wt%]	20	13	-	-
YbMn$_2$O$_5$ [wt%]	2	2	4	2
Mn$_3$O$_4$ [wt%]	11	5	3	2
Yb$_2$Mn$_2$O$_7$ [wt%]	1	-	7	12
KMn$_2$O$_{5.44}$ [wt%]	-	2	-	-
o-YbMnO$_3$ [wt%]	-	-	-	-
Rwp	9.4	9.0	11.7	11.4

Table B.4: Composition as a function of reaction time, yttrium. Full product composition and Rwp values obtained from Rietveld refinements of the Y1-21 - Y4-21 synthesis products. The syntheses were conducted at 240 °C. Apart from reaction time, all syntheses were performed under identical conditions.

ID	Y1-21	Y2-21	Y3-21	Y4-21
Time [h]	6	24	48	72
h-YMnO$_3$ [wt%]	84	90	89	84
Y(OH)$_3$ [wt%]	7	-	2	3
YMn$_2$O$_5$ [wt%]	3	3	4	8
Mn$_3$O$_4$ [wt%]	3	1	1	1
Y$_2$Mn$_2$O$_7$ [wt%]	-	1	-	-
KMn$_2$O$_{5.44}$ [wt%]	-	1	-	-
o-YMnO$_3$ [wt%]	4	4	4	4
Rwp	17.6	11.3	9.0	9.4

Table B.5: Composition as a function of cation concentration. Full product composition and Rwp values obtained from Rietveld refinements of the products of the Yb6-11, Yb7-21, and Yb9-21 syntheses. Hydroxide concentration can be read out of the synthesis ID, and Yb^{3+} concentration is given in the table. Apart from those two parameters, all syntheses were performed under identical conditions.

ID	[Yb^{3+}] [M]	h-YbMnO$_3$ [wt%]	YbOOH [wt%]	YbMn$_2$O$_5$ [wt%]	Mn$_3$O$_4$ [wt%]	Yb$_2$Mn$_2$O$_7$ [wt%]	o-YbMnO$_3$ [wt%]	Rwp
Yb7-21	0.17	86	-	4	3	7	-	11.7
Yb9-21	0.31	86	6	3	2	4	-	12.0
Yb6-11	0.31	87	9	2	1	-	1	10.3

Table B.6: The phase composition of products synthesized from different precursor types, but under otherwise similar conditions. The phase purities were obtained from Rietveld refinements. Salt precursors denote $Ln(NO_3)_3$, $MnCl_2$, and $KMnO_4$ solutions in 5:4:1 stochiometry, oxide precursors mean Ln_2O_3 and Mn_2O_3 powders in 1:1 stochiometry. Precursor type, reaction temperature, and reaction time are listed in the table, whereas Ln element and KOH concentration can be read out of the synthesis ID. All other parameters are identical for all syntheses listed.

ID	Yb4-11	Yb5-11	Avg*	Yb6-21	Y4-21	Y5-21
Precursor type	Salt	Oxide	Salt	Oxide	Salt	Oxide
T [°C]	150	150	150	150	240	240
Time [h]	24	24	24	24	72	72
h-LnMnO$_3$ [wt%]	75	1	76	32	84	85
LnOOH [wt%]	18	72	18	49	-	-
Ln(OH)$_3$ [wt%]	-	-	-	-	3	1
LnMn$_2$O$_5$ [wt%]	-	1	1	1	8	12
Mn$_3$O$_4$ [wt%]	5	-	3	-	1	1
Ln$_2$Mn$_2$O$_7$ [wt%]	1	-	1	-	-	-
KMn$_2$O$_{5.44}$ [wt%]	1	-	1	-	-	-
o-LnMnO$_3$ [wt%]	-	-	-	-	4	1
Mn$_2$O$_3$ [wt%]	-	25	-	18	-	1
Ln$_2$O$_3$ [wt%]	-	1	-	-	-	-
Rwp	8.0	13.3	10.7	11.1	9.4	8.2

*Average percentages of the Yb3-21, Yb4-21, and Yb5-21 syntheses.

Table B.7: Full product composition and Rwp values of the Yb3-21, Yb4-21, and Yb5-21 syntheses, all performed under similar conditions.

ID	h-YbMnO$_3$ [wt%]	YbOOH [wt%]	YbMn$_2$O$_5$ [wt%]	Mn$_3$O$_4$ [wt%]	Yb$_2$Mn$_2$O$_7$ [wt%]	KMn$_2$O$_{5.44}$ [wt%]	Rwp
Yb3-21	72	20	1	5	1	1	7.5
Yb4-21	75	20	1	2	2	-	8.1
Yb5-21	80	15	1	3	-	2	10.7

XRD DIFFRACTOGRAMS

This appendix contains X-ray diffractograms of all synthesis products. For the products where Rietveld refinements were carried out, the calculated intensities are plotted in addition to the measured intensities, as is the difference between measured and calculated intensity. In the diffractogram from the Y-11 product, where several peaks could not be identified, only the measured intensities and the calculated intensities of the YMn_2O_5 phase are shown.
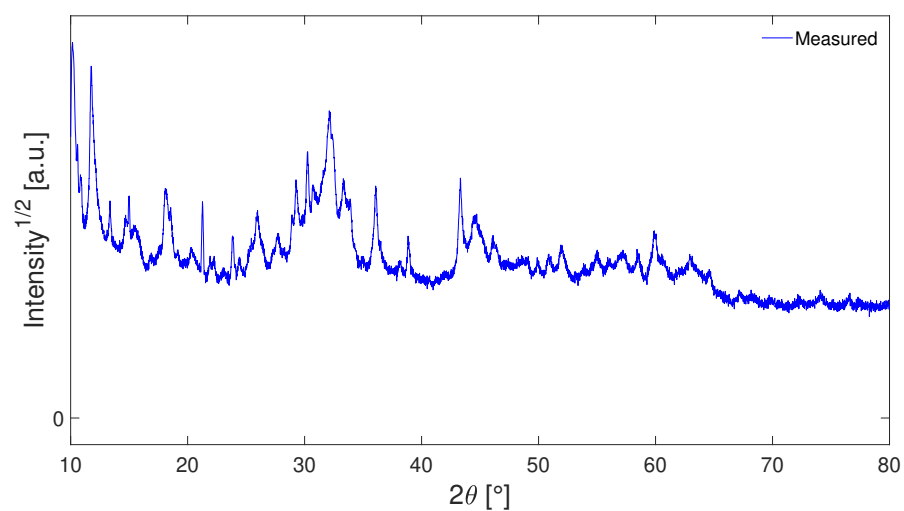
Figure C.1: X-ray diffractogram from the Yb-0.9 product.
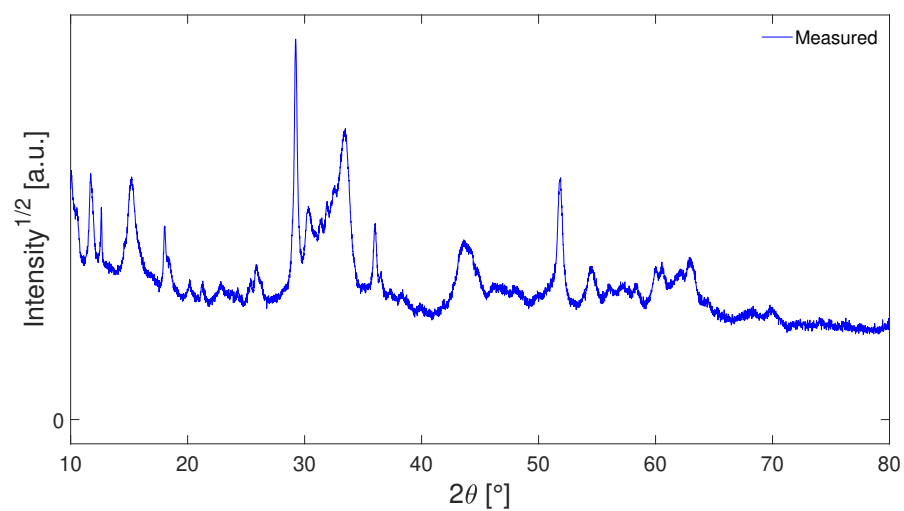
Figure C.2: X-ray diffractogram from the Yb1-11 product.
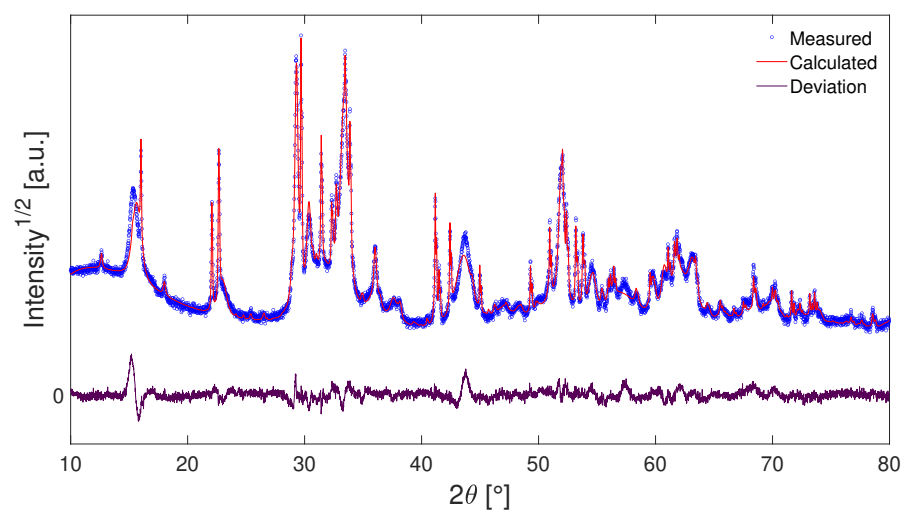
Figure C.3: Rietveld refinement of the Yb2-11 product.
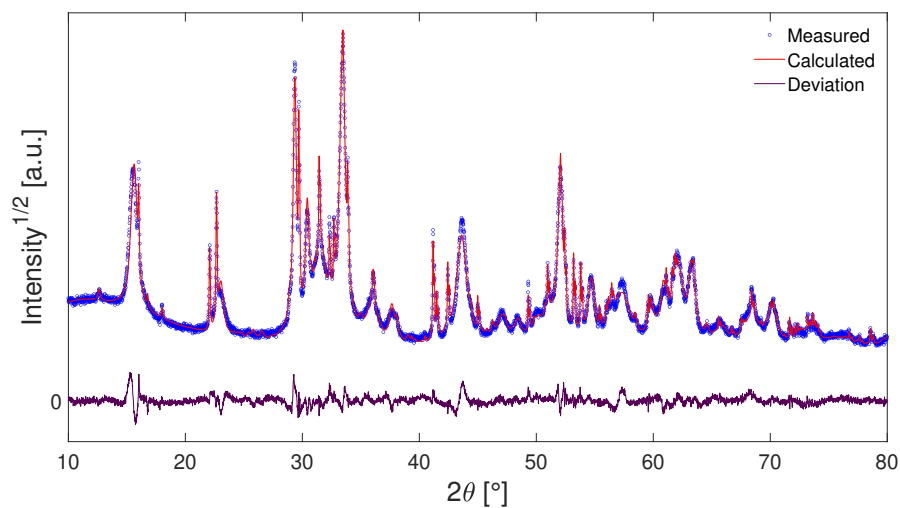
Figure C.4: Rietveld refinement of the Yb3-11 product.
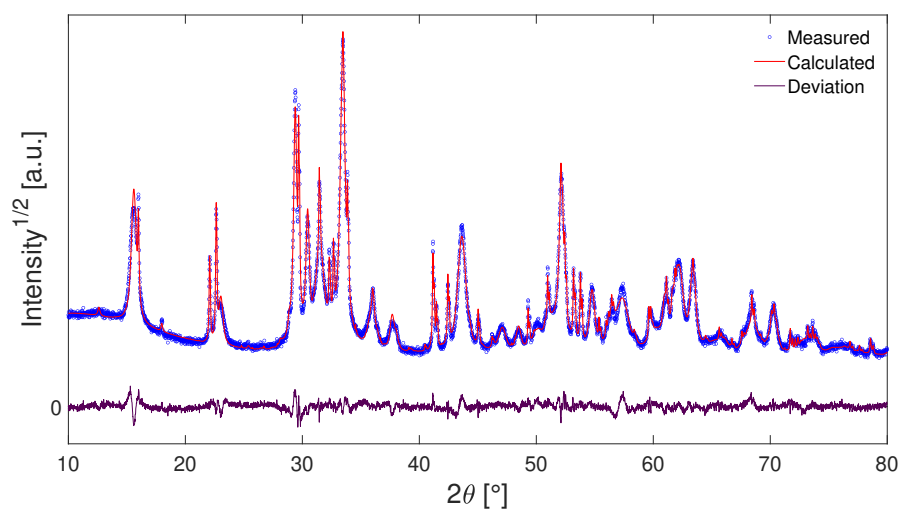
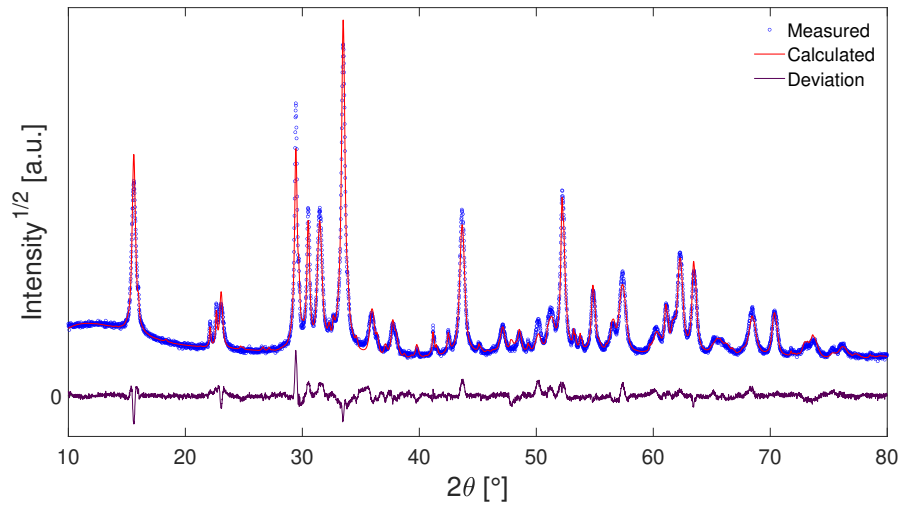*Figure C.5:* Rietveld refinement of the Yb4-11 product.
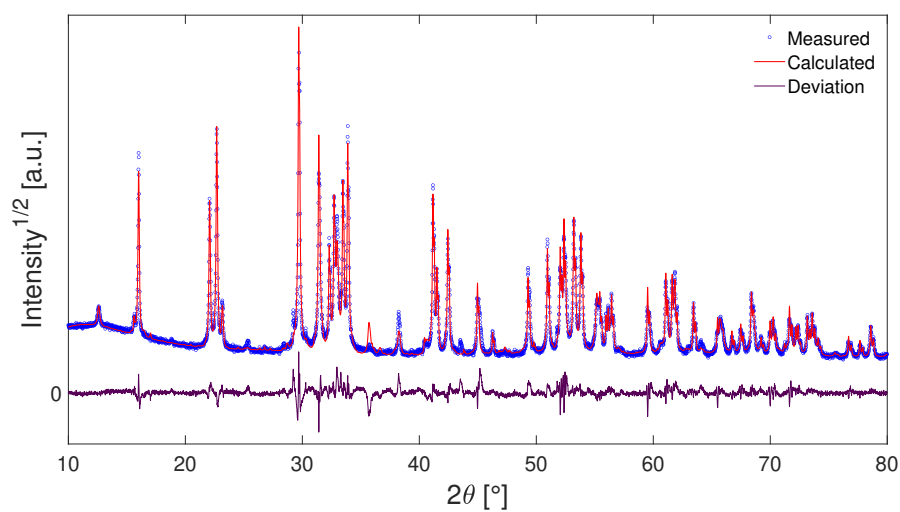
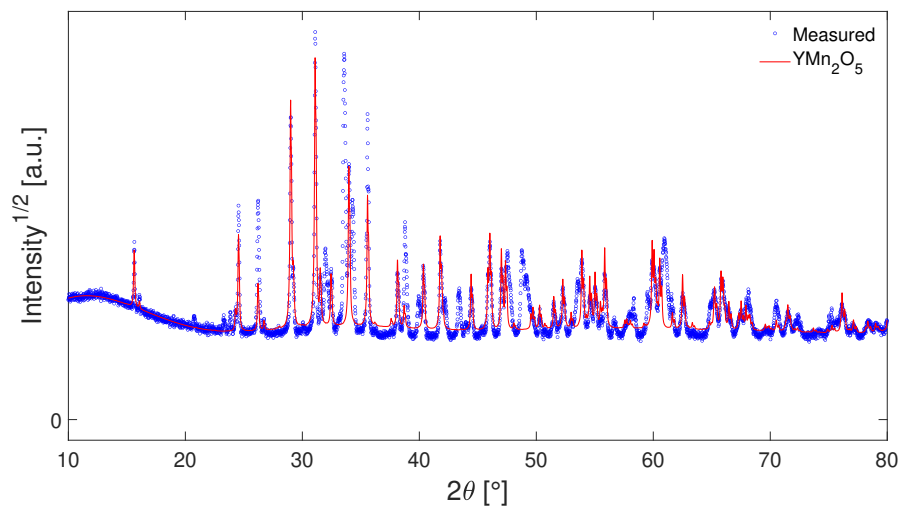*Figure C.6:* Rietveld refinement of the Yb5-11 product.
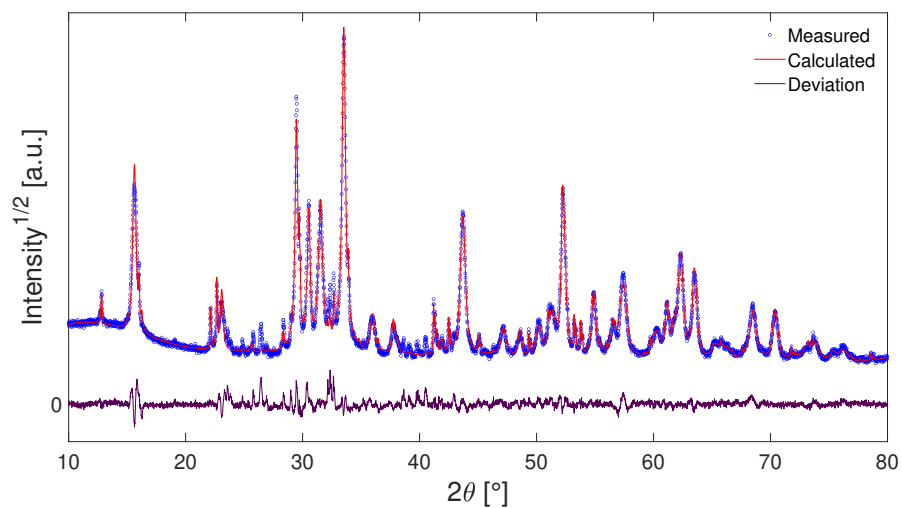
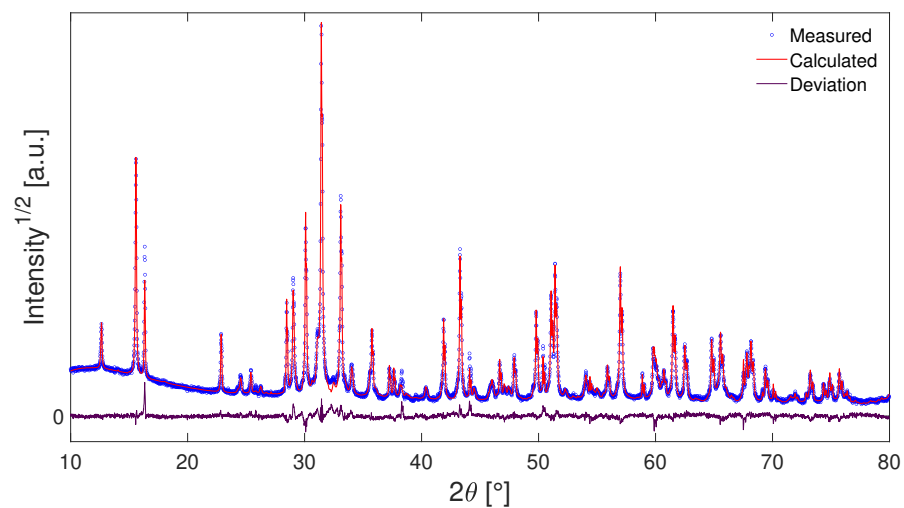*Figure C.7:* Rietveld refinement of the Yb6-11 product.
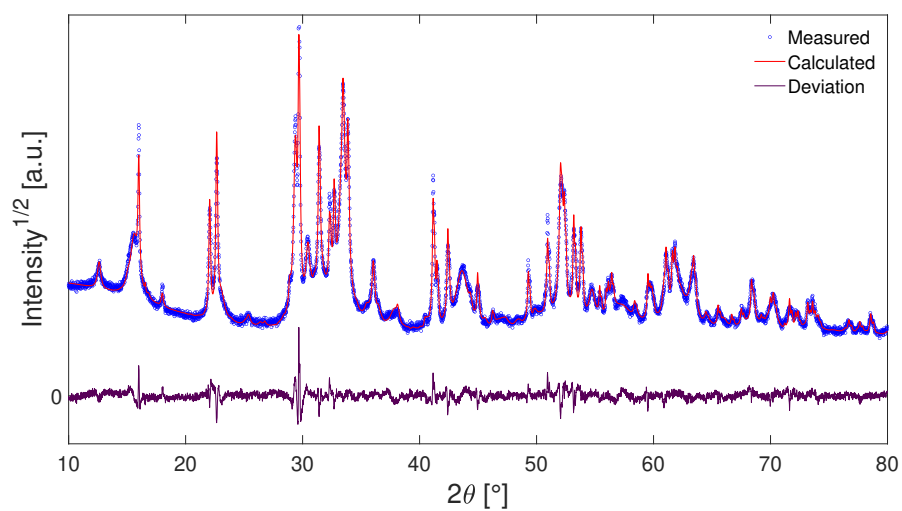
Figure C.8: Rietveld refinement of the Yb1-21 product.
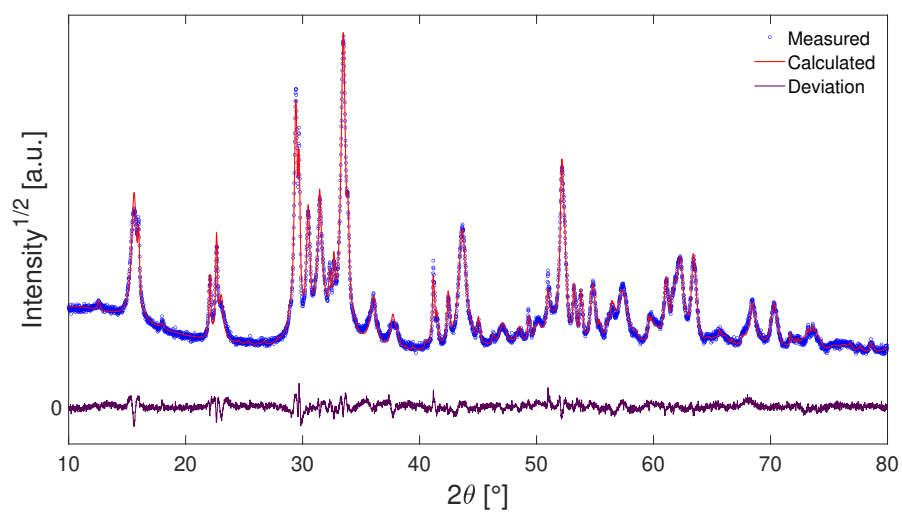
Figure C.9: Rietveld refinement of the Yb2-21 product.
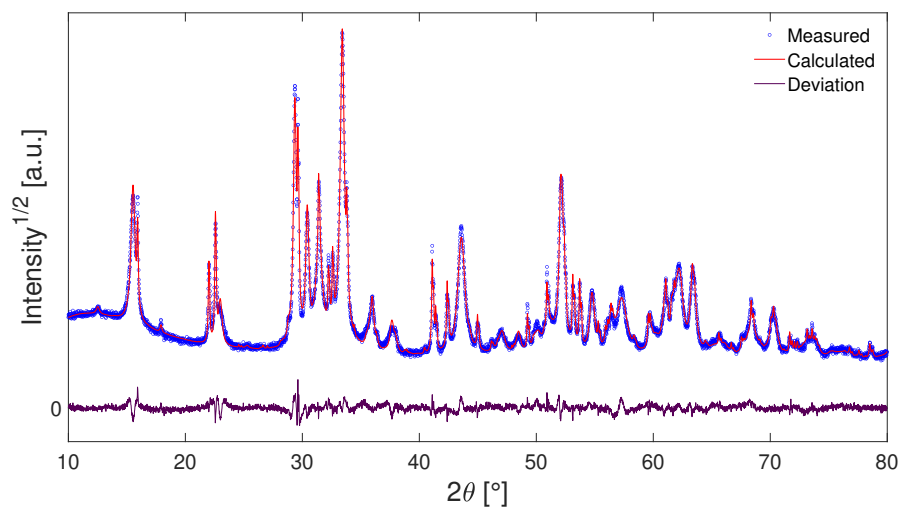
Figure C.10: Rietveld refinement of the Yb3-21 product.
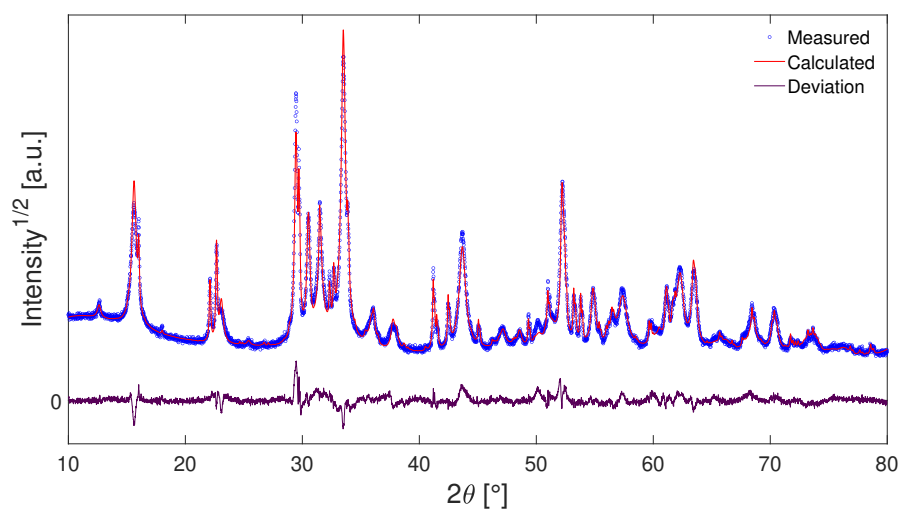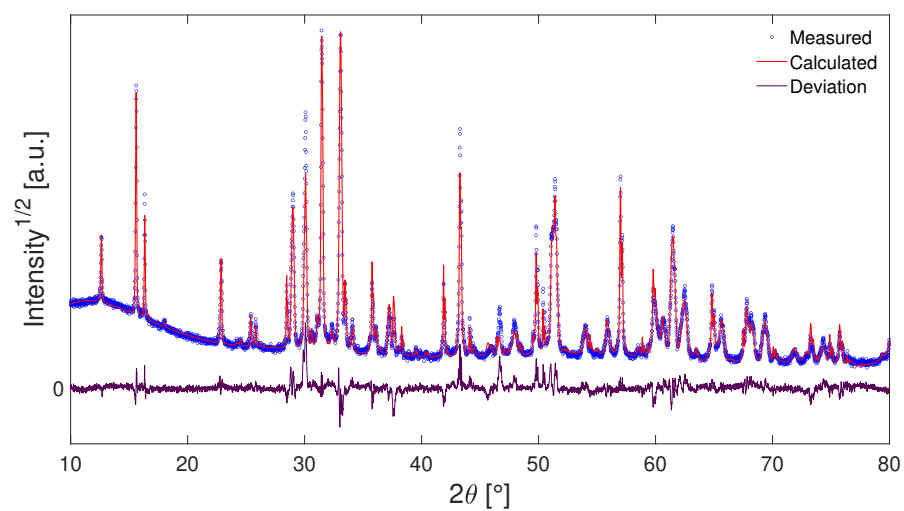

Figure C.11: Rietveld refinement of the Yb4-21 product.
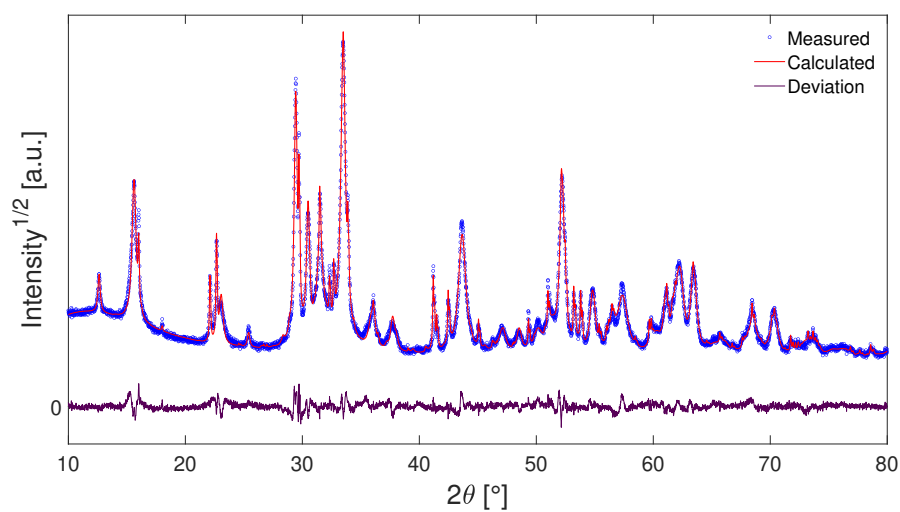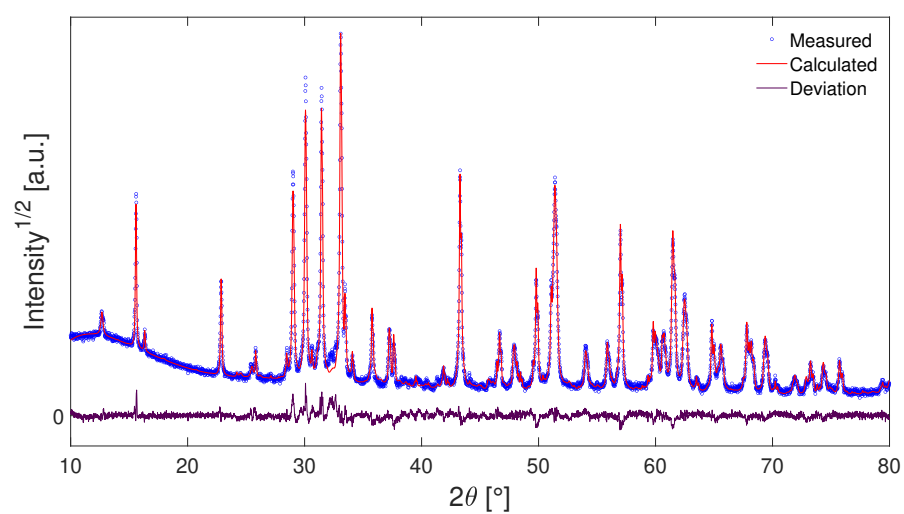

Figure C.12: Rietveld refinement of the Yb5-21 product.
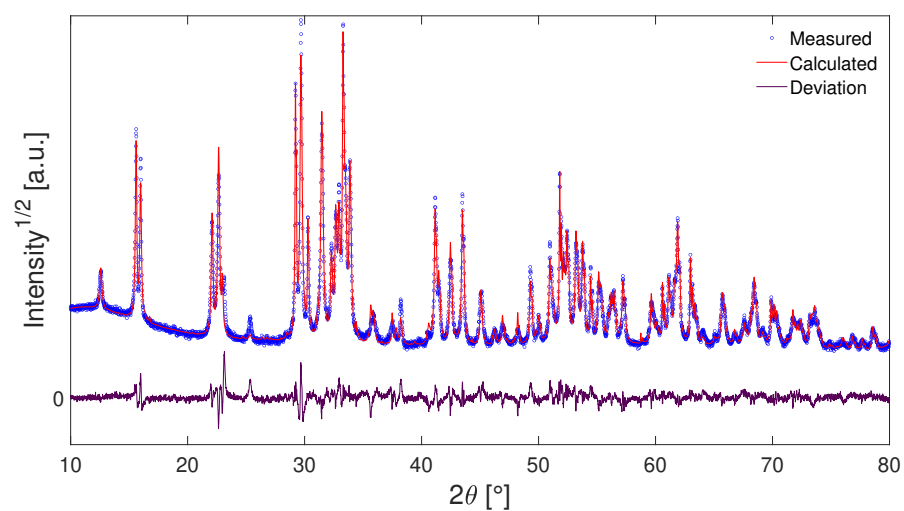
Figure C.13: Rietveld refinement of the Yb6-21 product.
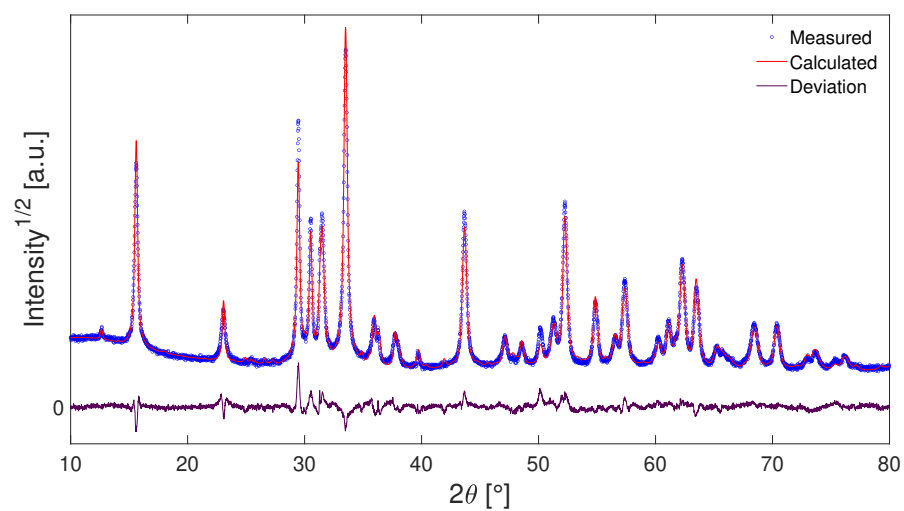
Figure C.14: Rietveld refinement of the Yb7-21 product.
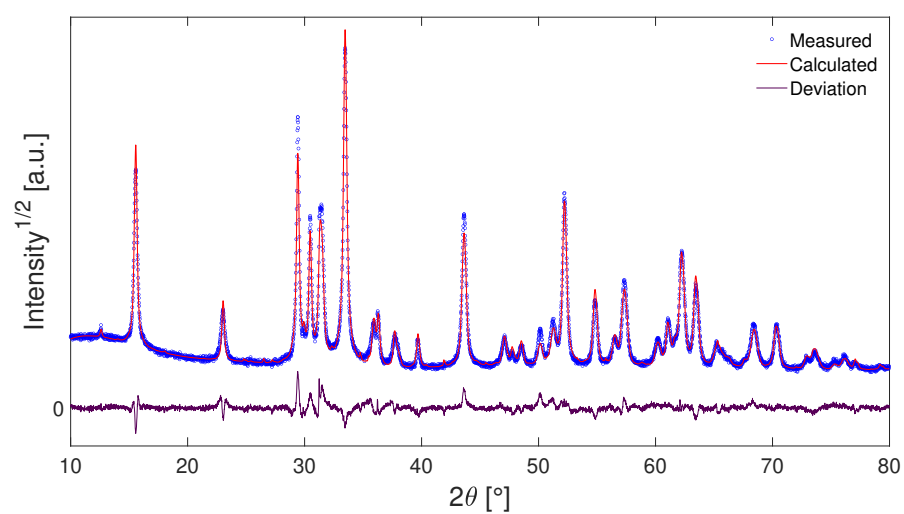
Figure C.15: Rietveld refinement of the Yb8-21 product.

Figure C.16: Rietveld refinement of the Yb9-21 product.

Figure C.17: X-ray diffractogram of the Y-11 product. The calculated intensities of the YMn_2O_5 phase, which appears to constitute a major part of the product, is also plotted. In addition, tiny amounts of $Y(OH)_3$ and $Y_2Mn_2O_7$ were identified in the product. Several unidentified peaks remain, see the discussion in Section 4.1.2. The product does not contain h-$YMnO_3$.

Figure C.18: Rietveld refinement of the Y-16 product.

Figure C.19: Rietveld refinement of the Y1-21 product.
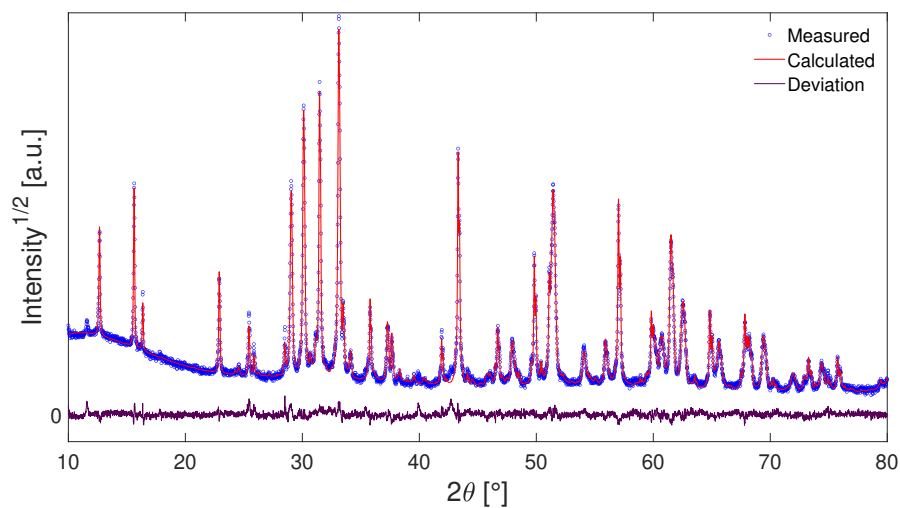

Figure C.20: Rietveld refinement of the Y2-21 product.
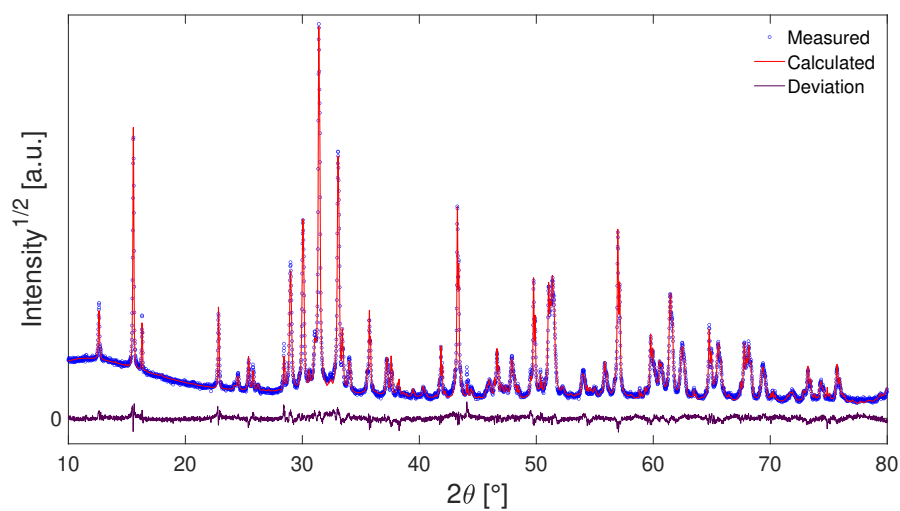
Figure C.21: Rietveld refinement of the Y3-21 product.
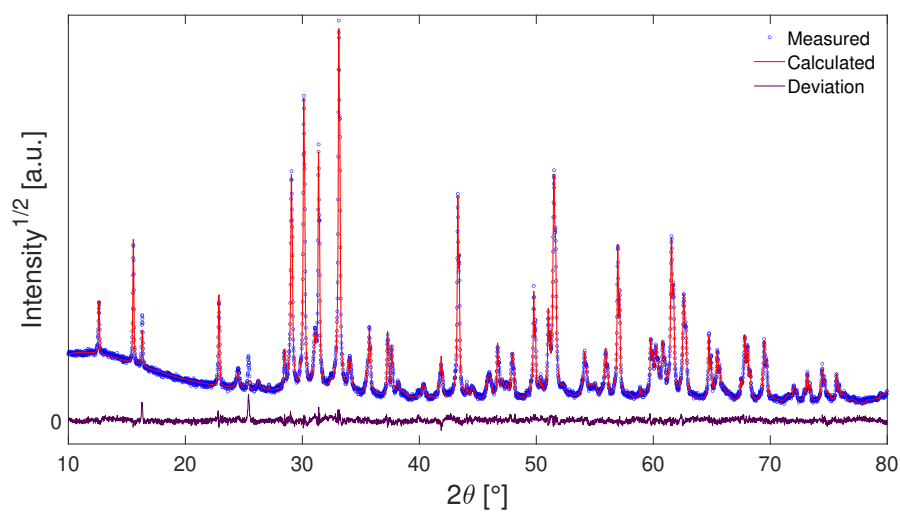

Figure C.22: Rietveld refinement of the Y4-21 product.

Figure C.23: Rietveld refinement of the Y5-21 product.